J-Coupling Effects on Quantification of the 1.3 ppm Lipid Methylene Resonance with *In-Vivo* Magnetic Resonance Spectroscopy at 3 T

by

Dylan Yamabe Breitkreutz

A thesis submitted in partial fulfillment of the requirements for the degree of

Master of Science

in

Medical Physics

Department of Oncology
University of Alberta

Abstract

Quantification of $1.3\,ppm$ lipid methylene protons by proton magnetic resonance spectroscopy has been shown to be relevant to a number of diseases. Additionally, T_2 estimation of $1.3\,ppm$ methylene protons has been used to grade the metastatic potential of colon tumours. J-coupling interactions of lipid protons result in time dependent signal modulations. J-coupling effects can hinder quantification and T_2 determination by modulating the signal acquired as a function of echo time rendering it difficult to accurately fit the decay curve. The objective of the work presented in this thesis is to investigate the effects J-coupling on quantification and T_2 estimation of $1.3\,ppm$ lipid methylene protons by using a modified PRESS (Point RESolved Spectroscopy) sequence to rewind the J-coupling evolution (also known as scalar coupling evolution). The effects of J-coupling on quantification and T_2 determination are studied by comparing the response of fatty acid phantoms and the tibial bone marrow of six volunteers to a standard PRESS sequence and to a modified PRESS sequence, which is designed to rewind J-coupling evolution. In corn oil, hexanoic, heptanoic, octanoic, oleic and linoleic acid phantoms, rewinding J-coupling evolution resulted in $13-198\,\%$ higher T_2 values compared to those obtained with standard PRESS. The amount of increase was higher for fatty acids with a higher percentage of J-coupled $1.3\,ppm$ protons. The narrow bandwidth PRESS sequence also resulted in significant changes in M_0 (-$77-29\,\%$). The response of the 1.3 ppm protons of hexanoic, heptanoic, octanoic, linoleic and oleic acid in response to a STEAM (Stimulated Echo Acquisition Mode) sequence was also examined. T_2values obtained with STEAM were closer to the values measured with narrow bandwidth PRESS. On average, in tibial bone marrow rewinding J-coupling evolution resulted in $\sim 21\,\%$ and $\sim 9\,\%$ higher M_0 and T_2 values,

respectively. The work demonstrates that the consequence of neglecting to consider J-coupling effects on the quantification of $1.3\ ppm$ lipid methylene protons and on their T_2 values is not negligible.

Preface

This research is an original work by Dylan Yamabe Breitkreutz.

All volunteer research subjects provided informed consent to a protocol which has Health Research Ethics Board of Alberta (HREBA) ethics approval, namely, HREBA 22307 “Pulse Sequence Development on 3 T Magnetic Resonance Imaging/Spectroscopy”.

A version of chapter 3 of the thesis has been accepted for publication by the journal *NMR in Biomedicine* as Dylan Y. Breitkreutz, B. Gino Fallone, Atiyah Yahya, “Effect of J-Coupling on 1.3-ppm lipid methylene signal acquired with localised proton MRS at 3 T”. I, Dylan Y. Breitkreutz, was responsible for the experimental work, data acquisition, data analysis and manuscript composition. B. Gino Fallone contributed to manuscript edits and experimental suggestions. Atiyah Yahya is the supervisory author who was involved with concept formation, experimental approach and manuscript composition.

Acknowledgments

First and foremost I would like to thank my supervisor Dr. Atiyah Yahya for her mentorship, knowledge, patience and time.

Thanks are also given to the additional members of my supervisory committee, namely, Dr. B. Gino Fallone and Dr. Nicola DeZanche, for their guidance and time.

I am grateful for the time and consideration of my thesis given to me by my arms' length examiner Dr. Richard Thompson.

Furthermore, I would like to thank Dr. Ron Sloboda, the chair of my defense committee for his valuable time.

I am grateful to the scholarships provided to me by the Natural Sciences and Engineering Research Council of Canada and the University of Alberta Faculty of Medicine and Dentistry 75th Anniversary Award. I am also grateful to the Canadian Breast Cancer Foundation: Prairies-NWT for providing research and stipend funding.

It has been a great privilege to study in a department with so many skilled, helpful and kind staff and physicists.

Lastly, I would like to thank my fellow students for their camaraderie and support.

Table of Contents

List of Figures

List of Tables

List of Abbreviations

BW	Bandwidth
CPMG	Carr-Purcell-Meiboom-Gill
TE	Echo Time
FSE	Fast Spin Echo
FFW	Fat Fraction
FW	Fat-Water Ratio
FID	Free Induction Decay
FWHM	Full Width Half Maximum
MR	Magnetic Resonance
MRI	Magnetic Resonance Imaging
MRS	Magnetic Resonance Spectroscopy
TM	Mixing Time
NMR	Nuclear Magnetic Resonance
PRESS	Point RESolved Spectroscopy
STEAM	STimulated Echo Acquisition Mode
RF	Radiofrequency
TR	Repetition Time

Chapter 1: Introduction

1.1 - Introduction

The first nuclear magnetic resonance (NMR) experiments were conducted to determine the magnetic moments of nuclei(1). As the field of NMR developed, it was discovered that the chemical environment of different nuclei on the same molecule resulted in distinct resonant frequencies and allowed these nuclei to be differentiated; this phenomenon was coined "the chemical shift effect"(2). As a result of the chemical shift effect, NMR became a tool capable of profiling the composition of a substance by producing a spectrum containing peaks associated with different nuclear groups in a substance. As an example, figure 1.1a shows a proton spectrum of linoleic acid, a primary fatty acid component of human lipids, and illustrates the distinct peaks in NMR spectra each of which corresponds to a different proton group in linoleic acid. Figure 1.1b is the molecular structure of linoleic acid. Eventually, spatial localization within an imaged volume became possible and due to NMR's non-destructive and non-invasive nature(3), it became an ideal method for diagnostic biochemical analysis of living systems. Proton magnetic resonance spectroscopy (MRS) measurements of lipids, specifically the quantification of signal from $1.3\ ppm$ -$(CH_2)_n$- methylene chain protons, have been used to investigate a range of diseases including cancer(4-7), diabetes(8-10), liver disease(11,12) and osteoporosis(13,14). The signal from the $1.3\ ppm$ methylene protons is typically chosen for lipid quantification due to its dominance in *in-vivo* lipid MRS spectra. Additionally, the transverse relaxation time (T_2) of methylene protons has been used to differentiate between colon cancers with a high and low risk of metastasis(15).

Lipid quantification and T_2 determination *in vivo* is performed most commonly by single voxel localization sequences such as PRESS(16) or STEAM(17). Some studies quantify the $1.3\,ppm$ methylene peak by integrating the peak area acquired with a single short TE(6-9,13,14,18), a timing parameter of MRS sequences. While this method requires less scan time, the measured fat level includes transverse relaxation effects and will be smaller than the actual value. Other studies correct for T_2 effects by acquiring peak areas at a series of TE values and fitting the data to a monoexponentially decaying function of the form $M_0 e^{-(\frac{TE}{T_2})}$(11,12). The fitting allows for both quantification of methylene signal in the absence of T_2 relaxation, i.e. M_0, as well as a determination of T_2. In general, correction for T_2relaxation will yield a more accurate representation of the signal of a particular proton group assuming longitudinal relaxation (T_1) effects are negligible. However, the protons of some molecules are subject to J-coupling interactions. A discussion of J-coupling and its consequences is necessary because all lipid proton groups display these interactions(19,20). Specifically, the $1.3\,ppm$ methylene protons of lipids interact with the $0.90\,ppm$methyl protons, the $1.6\,ppm$methylene protons and the $2.1\,ppm$allylic proton groups(21). J-coupling interactions result in sinusoidal signal modulation of the affected protons as well as splitting of the spectral peaks(3) – more detail will be provided about this phenomenon in later sections. The effects of signal modulation will be a shorter apparent T_2time and loss of signal which consequently alters the estimatedM_0 resulting in inaccurate quantification and T_2values.

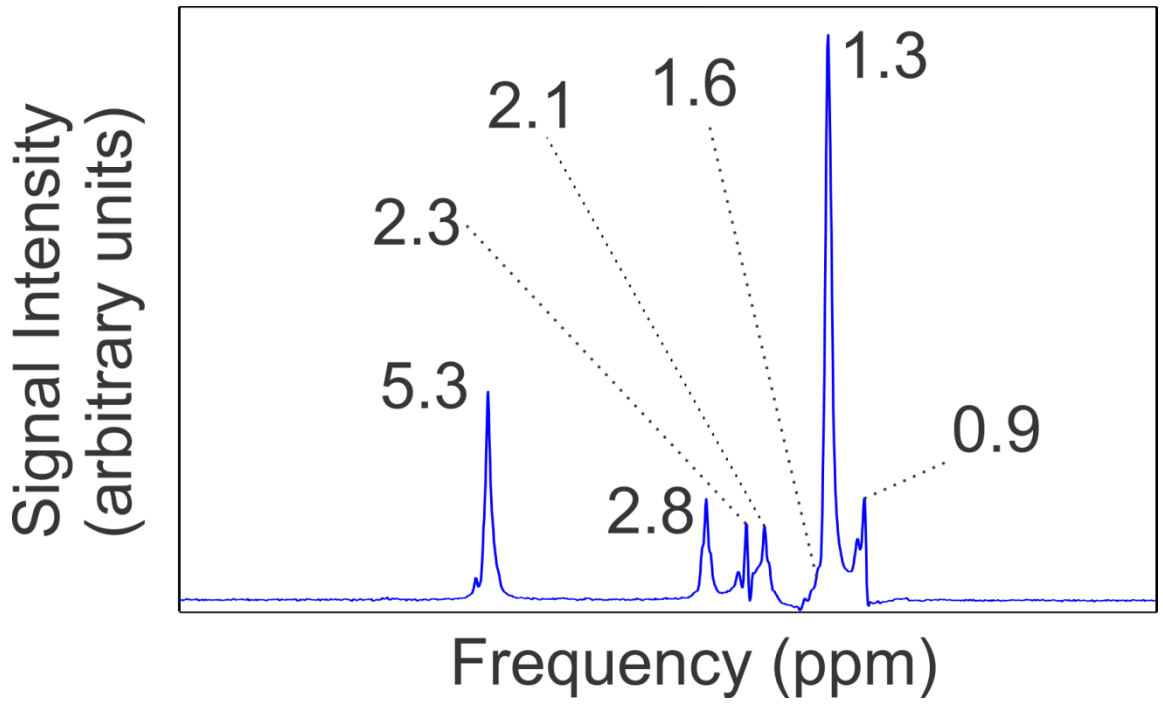

Figure 1.1

a. – Proton MRS spectrum of linoleic acid acquired at $3\,T$ using PRESS. The x-axis, in units of ppm, is a measure of resonant frequency.

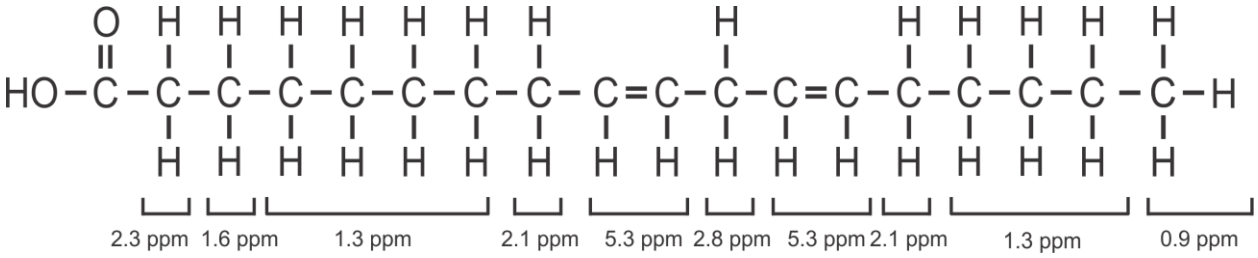

b. – Molecular structure of linoleic acid. The proton groups corresponding to the peaks in (a) are labelled.

Despite the fact that J-coupling interactions of $1.3\,ppm$ methylene protons exist, J-coupling modulations of the$1.3\,ppm$ lipid signal *in vivo*, and in phantoms representative of *in*

vivo lipids, appear minimal (19). In mathematical terms, the decay curve of the $1.3\ ppm$methylene protons is monoexponential in nature. As a result, the effects of J-coupling on the quantification and T_2 determination of $1.3\ ppm$ methylene protons may appear inconsequential. However, previous works have noted the effects of the J-coupling interactions of $1.3\ ppm$ lipid methylene protons. A number of authors have observed an increase in fat signal in fast spin echo (FSE) and Carr-Purcell-Meiboom-Gill (CPMG) imaging relative to conventional spin echo imaging and attribute the increase in signal to a minimization of J-coupling effects resulting from the reduced interpulse timing of FSE and CPMG imaging(22-24). The effects of the phenomenon on oils, fats and bone marrow has been demonstrated experimentally (24-29). Furthermore, work done by Hamilton et al. shows a difference in the quantification and T_2 estimates of the $1.3\ ppm$ methylene protons determined with PRESS and with STEAM. The differences were attributed to a difference in J-coupling evolution during the two sequences(19). Despite these numerous observations, little work has been done in attempt to account for the effects of J-coupling on the quantification and T_2 determination of the $1.3\ ppm$ lipid methylene protons. The only work encountered, by Gajdošík et al, which has made an attempt to account for these effects was recently published in 2014. The acquired peak areas of different lipid proton groups including those of the $1.3\ ppm$ protons were fit to a product of a monoexponential function and a sinusoidal function to explicitly account for the oscillatory modulation due to J-coupling(30). However, due to the largely monoexponential nature of the decay curve of $1.3\ ppm$ methylene signal, only small changes in quantification and T_2 estimates were found when compared to a strictly monoexponential fit for phantoms and no difference was observed for *in-vivo* liver fat.

The objective of the work described in this thesis is to investigate the J-coupling behaviour of the $1.3\,ppm$ lipid methylene protons. Given the presence of J-coupling interactions, the lack of signal modulation is investigated following which a method used previously by Yahya et al.(31) is applied to rewind the J-coupling evolution of $1.3\,ppm$ methylene protons to investigate the extent to which J-coupling evolution affects quantification and T_2 estimates of the $1.3\,ppm$ lipid protons.

The following sections of chapter 1 will include background information on the discipline of MRS necessary to understand the work that will follow. In chapter 2, more directly relevant background information as well as experimental details are provided. Chapter 3 summarizes the outcomes of the research. Lastly, chapter 4 consists of concluding remarks.

1.2 – Basic Theory

1.2.1 – Nuclear Magnetic Moments

Fundamental to our discussion of the theory behind proton MRS is the concept of nuclear magnetic moments. In section 1.1, it was stated that the signal used to create a spectrum in MRS originates from the nuclei of molecules in a living system or in a phantom. However, not every nucleus is capable of creating an NMR signal; the nucleus must have a nuclear magnetic moment, μ. Whether or not a nucleus possesses a nuclear magnetic moment depends on its composition of protons (fundamental subatomic particles with a positive net charge) and neutrons (fundamental subatomic particles with no net charge). If either or both of

the number of protons and neutrons composing a nucleus is odd, that nucleus will have a nuclear magnetic moment.

1.2.2 – Nuclear Magnetic Moments and Angular Momentum

A nuclear magnetic moment is required for MRS viability because it results in an interaction between the nuclei and an external magnetic field. Classical theory tells us that(32)

$$\mu = \frac{qv}{2\pi r}\pi r^2, \tag{1.1}$$

where q is the charge of the particle, v is the velocity of the particle, and r is the radius of the particle's circular orbit. So, a nuclear magnetic moment is created by a spinning charge.

We can relate μ to angular momentum, L. If we invoke the equation for classical angular momentum(33),

$$L = mvr, \tag{1.2}$$

where m is the mass of the particle, and relate equations (1.1) and (1.2) we see that

$$\mu = \frac{q}{2m}L = \gamma_{rad}\,L, \tag{1.3}$$

where $\frac{q}{2m}$ is defined as γ_{rad}, the gyromagnetic ratio with units of $\frac{rad}{T \bullet s}$ with a value specific to each species of nuclei[1].

[1] For ^{1}H nuclei or protons, $\gamma_{rad} = 2.674x10^8 \frac{rad}{T \bullet s}$

Quantum mechanical theory tells us that the angular momentum of elementary particles and nuclei is given by(32)

$$L = (\frac{h}{2\pi})\sqrt{I(I+1)}, \quad (1.4)$$

where h is Planck's constant (6.626x10^{-34} m^2 kg/s) and I is the spin of the elementary particle or nucleus. I can only take on integer or half integer values (i.e. ½, 1, 1 ½, etc.), thus, the angular momentum of elementary particles is quantized. Rules exist which allow us to determine the spin of a nucleus(3):

1. Nuclei with odd mass numbers[2] have positive half-integral values of spin.

2. Nuclei with and even mass number and an even charge number have a spin of zero.

3. Nuclei with an even mass number and an odd charge have positive integral values of spin.

As a vector, angular momentum has both direction and magnitude. For our discussion of the basic theory of MRS the z-direction is of primary interest as this is the conventional direction of the external applied magnetic field. The component of angular momentum in the z-direction, L_Z, is given by(32)

$$L_Z = \left(\frac{h}{2\pi}\right)m. \quad (1.5)$$

[2] Mass number is the sum of the number of protons and neutrons in a nucleus.

Here m, is another quantum number similar to I, which can take on values of $I, I - 1, I - 2, \ldots -I$. Thus, combining equations (1.3) and (1.5) along with the fact that protons are spin $\frac{1}{2}$ particles, the magnetic moment in the z-direction of a proton is

$$\mu_Z = \pm\frac{1}{2}\gamma_{rad}\left(\frac{h}{2\pi}\right). \quad (1.6)$$

1.2.3 – Nuclear Magnetic Moments and Applied External Magnetic Fields

In the absence of an external magnetic field, B_0, the nuclear magnetic moments[3] of a population of nuclei will have no preferred direction. The random orientations of this spin population will result in no coherence amongst the directions of spins and hence no net macroscopic magnetization. However, in the presence of an applied external magnetic field the spins will align preferentially in a direction parallel or anti-parallel to the direction of B_0, referred to as the z-direction by convention. The interaction between spins and B_0 results in an interaction energy given by(3,32)

$$E = -\mu_z B_0. \quad (1.7)$$

The energy difference between the parallel and anti-parallel orientation can be obtained by combining equations (1.6) and (1.7) to get

$$\Delta E = \gamma_{rad}\frac{h}{2\pi}B_0. \quad (1.8)$$

[3]Henceforth, the term "spin" will be used interchangeably with "nuclear magnetic moment" due to convention.

1.2.4 – The Resonance Condition and Larmor Frequency

The basis of NMR rests on the two populations of spins created by the applied external magnetic field and the energy difference between the parallel and anti-parallel spin states. From quantum mechanics we know that a change in spin state will either emit a photon or absorb of a photon with a specific energy, depending on whether energy is released by the transition or needed for transition, given by equation (1.8) – the relationship between spin state transitions and photons is termed resonance. To determine the energy of the photons needed to resonate with a spin system we start with the energy of a photon given by(32)

$$E = h\nu_0, \tag{1.9}$$

where ν_0 is the frequency of the photon in *Hz*.

The energy of the photon must match the energy difference between the two spin states in order to resonate, therefore, equating equations (1.8) and (1.9) we see that

$$\nu_0 = \frac{\gamma_{rad}}{2\pi} B_0 = \gamma B_0, \tag{1.10}$$

where $\gamma = 42.6 \frac{MHz}{T}$ for ^{1}H nuclei.

The frequency given by equation (1.10) is known as the Larmor frequency. It will be shown in later sections that the Larmor frequency plays a crucial role in the NMR experiment.

1.2.5 – Spin Population Statistics

In the presence of an applied external magnetic field the two spin states will not be equally populated. The small energy difference of $E = hv_0$ leads to a preferential spin state since one state will have a slightly lower energy. The spin states will be populated according to Boltzmann statistics and the ratio of the parallel (α state) to the anti-parallel (β state) is given by (34)

$$\frac{n_\alpha}{n_\beta} = e^{\Delta E/kT} = 1 + \frac{\Delta E}{kT} = 1 + \frac{hv_0}{kT}, \qquad (1.11)$$

using a Taylor expansion. In equation (1.11) k is the Boltzmann constant with a value of $1.38x10^{23}\frac{J}{K}$ and T is absolute temperature in degrees Kelvin. Even for high field magnets (>3 T) the ratio of alpha to beta spins is excessively small. For example, at room temperature in a 3 T field, for every one million spins in the beta state there will be approximately one million and twenty spins in the alpha state.

1.2.6 – The Net Magnetization Vector

The disparity between the number of spins in an alpha or beta state leads to a larger number of spins in the alpha energy state. The result of the inequality is a net magnetization vector, M_0. At equilibrium, M_0 points in the direction parallel to B_0 along the z-axis and is referred to as longitudinal magnetization, denoted as M_Z. $M_0$is the macroscopic representation of the spin population and is used when discussing the further details of MR (magnetic

resonance) experiments. Furthermore, the magnitude of the vector determines the maximum amount of signal that can be detected in an MR experiment which is given by(3)

$$M_0 = \left(\frac{\gamma h}{2\pi}\right)^2 \left(\frac{nB_0}{4kT}\right), \tag{1.12}$$

where n is the total number of spins in the population.

The small magnitude excess of spins in the alpha state, however, results in a relatively small M_0. Consequentially, MR is a relatively insensitive technique which is one of its major drawbacks, since longer scan times are necessary to compensate for the low signal to noise ratio (SNR).

1.3 – The NMR Experiment

The simplest form of MR experimentation consists of a90°excitation pulse followed by signal acquisition and Fourier analysis to create an MRS spectrum from an entire sample placed in an external static magnetic field. Spatially localized MRS experiments, which produce spectra from a designated voxel of interest within a sample, and MRI experiments, which render 2D images, both require a series of RF pulses along with the application of magnetic field gradients. The details of specific techniques (pulse sequences) will be discussed later on.

1.3.1 – The Rotating Reference Frame

Two reference frames are commonly used in NMR, MRS and MRI theory – the static and the rotating reference frame. The static reference frame (x, $y$and z) is a standard Cartesian reference frame in which the z-axis points along the direction of B_0. In the rotating reference frame (x_ρ, y_ρ and z_ρ) the analog of the z-axis is the z_ρ-axis, which also points in the direction of B_0. The significant difference between the two frames of reference is that the rotating frame rotates at a frequency of v_0 with respect to the static reference frame about the z_ρ-axis. Due to the precessional frequency of M_0, the motion of magnetization during MR experiments appears complicated in the static reference frame. The rotating reference frame is used to simplify the illustration of M_0's motion during pulse sequences. When aligned along the direction of B_0, M_0 appears identical in both reference frames since M_0 precesses around the direction of B_0. However, when M_0 has a component perpendicular to B_0 it will visibly precess at the Larmor frequency in the static reference frame. In the rotating reference frame M_0 will appear static since both M_0 and the reference frame rotate at the same frequency of v_0 as illustrated in figure 1.2.

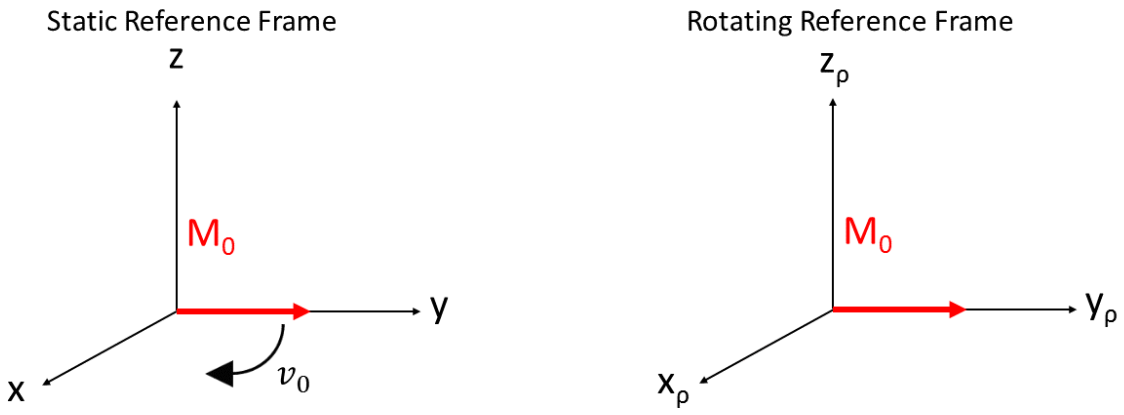

Figure 1.2 - The static and rotating reference frame. The rotating reference frame rotates at a frequency v_0 about the $z_{\boldsymbol{\rho}}$ axis with respect to the static reference frame.

1.3.2 – Preparation, Excitation and Detection

The NMR experiment is generally divided into three phases: preparation, excitation and detection. The preparation phase, with mathematical details outlined in sections 1.2.3 – 1.2.6, consists of the sample under investigation being placed in an external static magnetic field. The result is magnetization of the sample and production of the net magnetization vector M_0, which at this point in the experiment points along the z-axis, parallel to B_0. This is the equilibrium state of an NMR experiment during which no signal is detected. During excitation, a time varying magnetic field, denoted as B_1 , is produced by radiofrequency (RF) energy oscillating at the Larmor frequency which is transmitted by the RF transmission coil surrounding the sample.

The direction of $B_1$is perpendicular to the z-axis and results in a torque on M_0 causing it to precess towards the xy plane. The duration of the RF pulse and the final position of M_0 depend on the type of pulse used and the desired effect of the pulse. A$90°$excitation pulse, for example, manipulates M_0 by 90 degrees into the xy plane. A $180°$ degree pulse, on the other hand, results in inversion of M_0. The component of M_0in the xy plane is denoted M_{XY} and is referred to as transverse magnetization. The vector M_{XY} precesses at the Larmor frequency and induces an electromotive force via Faraday's law of electromagnetic induction in the RF receiver coil. During detection, the signal produced in the reception coil by M_{XY} is read out by the computational components of the MR scanner hardware. This signal, known as the free induction decay (FID), is Fourier transformed to create the NMR spectrum of the sample. The steps of the basic NMR experiment are illustrated in figure 1.3.

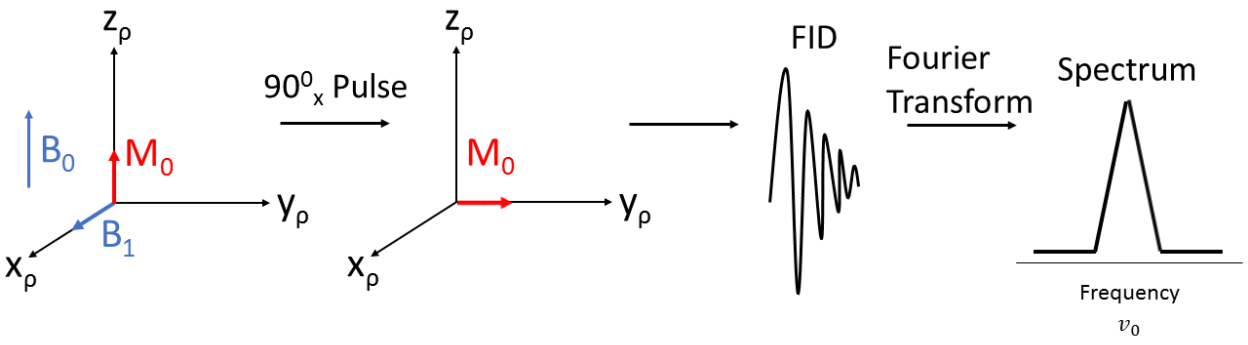

Figure 1.3– Vector diagram in the rotating frame of reference illustrating the effect of a $90°_X$ excitation pulse, the creation of the FID and the spectrum created from the FID's Fourier transform.

1.4 – Chemical Shift and The ppm Scale

1.4.1 Chemical Shift

All protons on a molecule do not experience the same static magnetic field. The variations in local magnetic environment arise due to the chemical structure of a molecule. The presence of more or less electronegative atoms, as well as the atom's distance from the proton in question, will alter the distribution of electrons around a given proton. In the presence of B_0, the electrons populate two different energy levels in a similar fashion to protons as discussed in sections 1.2.1 – 1.2.3. However, due to the negative charge of electrons the resulting net magnetic moment points anti-parallel to B_0. This opposing nuclear magnetic moment "shields" or "screens" the protons from B_0, effectively reducing the magnetic field seen by the proton in question by an amount dependent on the electron distribution around the proton and thus dependent on the chemical structure of the molecule(3). This effective magnetic field, B, is expressed mathematically as(35)

$$B = B_0(1 - \sigma), \tag{1.13}$$

where is a dimensionless value defined as the shielding or screening constant. Combining equations (1.10) and (1.13) we see that

$$v = \gamma B = \gamma B_0(1 - \sigma). \tag{1.14}$$

Thus, the resonant frequency of a proton will depend on the magnetic environment determined by its location in a molecule. The chemical shift phenomenon leads to the protons in a molecule having a wide variety of resonant frequencies which results in distinct peaks in an

MRS spectrum allowing for the discernment of metabolic information. Figure 1.1 exhibits seven distinct peaks each of which corresponds to distinct proton groups of linoleic acid distinguished by different chemical and magnetic environments.

1.4.2 – The ppm Scale

The ppm scale is often used instead of resonant frequency due to v's dependence on the strength of B_0. This is achieved by defining the chemical shift of a reference compound and using the equation(3)

$$\delta = \frac{v - v_{ref}}{v_{ref}} * 10^6, \quad (1.15)$$

where v is the resonant frequency of the proton group in question, v_{ref} is the resonant frequency of the reference resonances – the protons of the CH_3 group of tetramethylsilane(3) (TMS) which are assigned a chemical shift of $0\ ppm$ – and δ is the chemical shift between the proton group in question and the reference resonance in units of ppm(3).

1.5 - Relaxation Effects

After excitation, the transverse magnetization vector will not exist and create signal indefinitely. Random interactions within the spin system, as well as with the system and its surroundings, return the system to its equilibrium state in which M_Z is equal to M_0. These

interactions have been defined as spin-spin, or transverse (T_2) relaxation and spin-lattice or longitudinal (T_1) relaxation.

1.5.1 – T_1 Relaxation

In an NMR experiment, the spin system under investigation is not isolated but rather is surrounded by a molecular environment – i.e. the lattice. The random molecular motion of nuclei, electrons and molecules within the lattice produces fluctuating magnetic fields which oscillate at a range of frequencies. If these oscillations match the Larmor frequency of the spin system, there will be an exchange of energy from the spin system to the lattice(3,35). This interaction results in a return of the system's spin states to their equilibrium values given by equation (1.11) and a restoration of M_Z. Phenomenologically, the equation describing the change in M_Z as a function of time is given as(35,36)

$$\frac{dM_Z(t)}{dt} = -\frac{M_0 - M_Z(t)}{T_1}, \tag{1.16}$$

where T_1 is the time constant governing longitudinal relaxation.

Solving the equation for a $90°$ excitation pulse and a $180°$ inversion pulse yields(35,36)

$$M_Z(t) = M_0\left(1 - e^{-t/T_1}\right) \tag{1.17}$$

and

$$M_Z(t) = M_0\left(1 - 2e^{-t/T_1}\right), \tag{1.18}$$

respectively. Figure 4 illustrates the recovery of M_Z after both a$90°$ excitation pulse and a $180°$ inversion pulse.

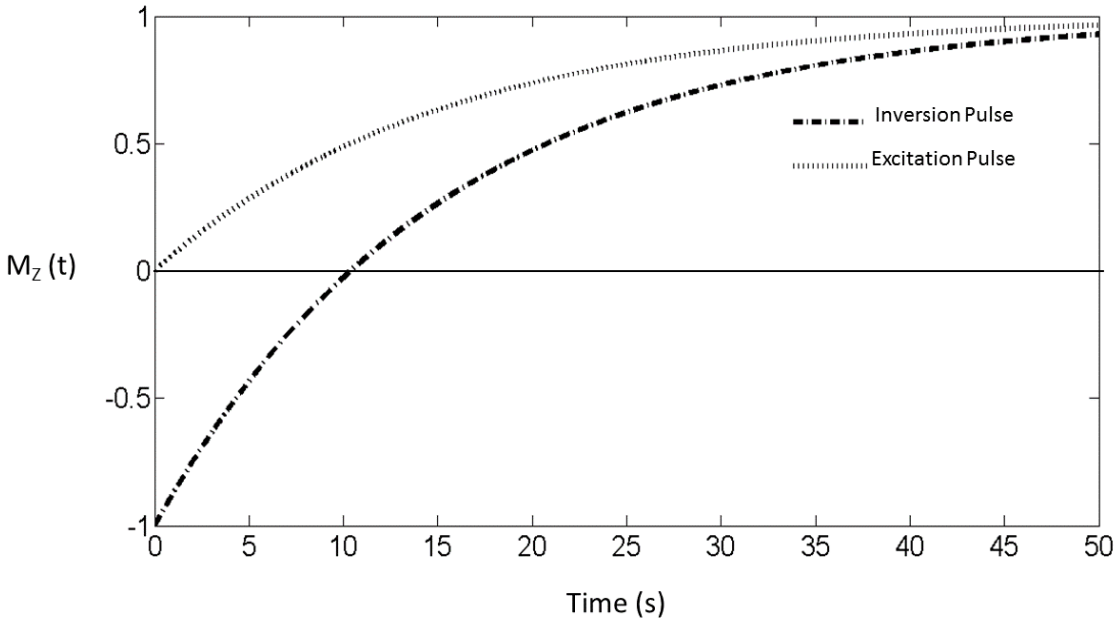

Figure 1.4– The process of T_1 relaxation. After a $90°$ excitation pulse all longitudinal magnetization is converted into transverse magnetization and $\frac{M_Z}{M_0} = 0$. After a $180°$ inversion pulse M_Z points along the $-z$-axis and $\frac{M_Z}{M_0} = -1$. Longitudinal magnetization then begins to recover monoexponentially with time. A T_1 time of 1.5 seconds is used as an example.

1.5.2 – T_2 Relaxation

In addition to oscillating magnetic fields, the environment in which the spin system exists will also be permeated by random static magnetic fields(35). Generally, the source of these static fields are neighbouring spins, hence the term “spin-spin relaxation” (35). The static fields alter the precessional frequency of spins within the population in a fixed manner and result in a range of precessional frequencies. As a result, transverse magnetization will dephase and lose coherence over time, resulting in a loss of signal. The phenomenological equation describing the change in M_{XY} as a function of time is given as(36)

$$\frac{dM_{XY}(t)}{dt} = -\frac{M_{XY}}{T_2}, \tag{1.19}$$

where T_2 is the time constant governing transverse relaxation. Solving the equation for a 90° excitation pulse yields(36)

$$M_{XY}(t) = M_0 e^{-t/T_2}. \tag{1.20}$$

Figure 1.5 illustrates the decay of transverse magnetization following a90° excitation pulse.

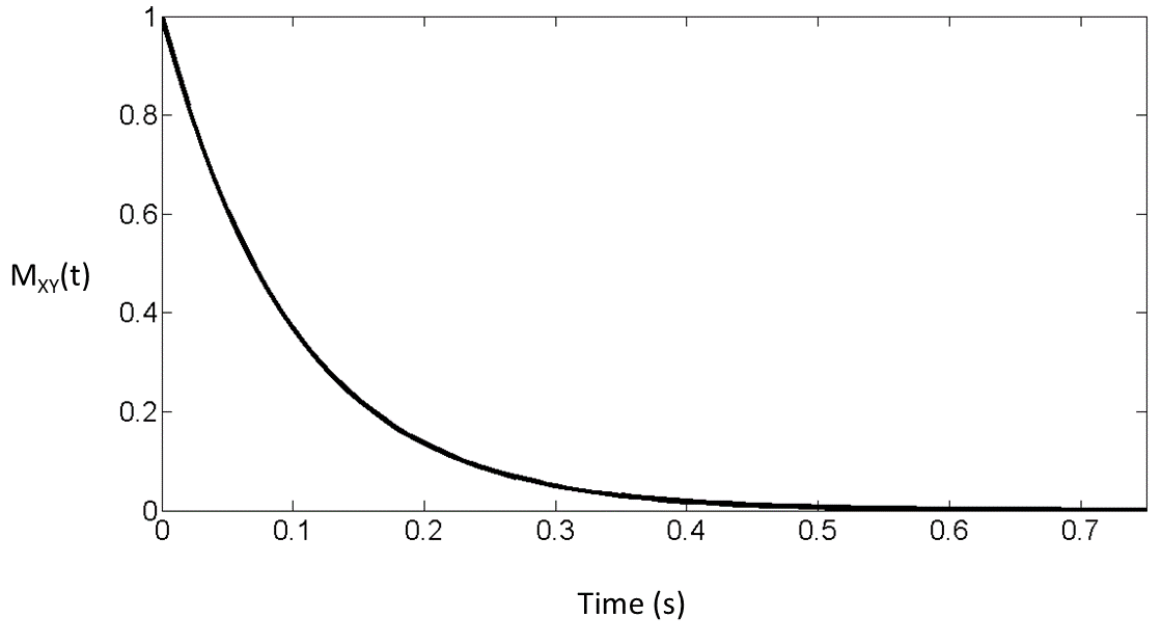

Figure 1.5– The process of T_2 relaxation. After a $90°$ excitation pulse all longitudinal magnetization is converted into transverse magnetization and $\frac{M_{XY}}{M_0} = 1$. Transverse magnetization then begins to dephase and decays monoexponentially with time. A T_2 time of 100 ms is used as an example.

1.5.3 – Factors Affecting T_1 and T_2 Times

The relaxation times of spins in different molecules vary due to the chemical structure of the molecule as well as its physical characteristics affecting molecular motion, such as viscosity and temperature. Additionally, the local environment and biology will affect relaxation.

The process of transverse relaxation is expedited due to time independent static field inhomogeneities in the magnetic environment. The inhomogeneities are caused by

susceptibility effects of the surrounding environment, imperfections in the static magnetic field, chemical shift effects and the use of gradients (37). Much like the random magnetic inhomogeneities discussed in section 1.5.2, the static inhomogeneities will cause transverse magnetization to dephase. The result is an apparent transverse relaxation time, denoted as T_2^*, which is smaller than the relaxation time in the absence of static field inhomogeneities, T_2. The relation between the relaxation constants is given by(37)

$$\frac{1}{T_2^*} = \frac{1}{T_2'} + \frac{1}{T_2}, \tag{1.21}$$

where T_2' is the contribution from static field inhomogeneities. It should be noted that transverse relaxation due to static inhomogeneities is reversible through use of 180° refocussing pulses, to be discussed later, whereas transverse relaxation from spin-spin interactions is not, due to their random nature(37).

1.6 – Spin Echoes and Stimulated Echoes

To obtain an MRS spectrum, signal from the spins of interest must be excited and acquired. In previous sections the creation of transverse magnetization via a90° excitation pulse was discussed. Signal can be acquired immediately after excitation using a receiver coil. This technique constitutes the most basic method of pulsed spectroscopy. However, other pulse methods which consist of a series of RF pulses have been designed to address concerns such as time constraints or relaxation effects. Of particular relevance to this thesis are the spin echo and the stimulated echo.

1.6.1 – The Spin Echo

After the manipulation of magnetization into the $x_\rho y_\rho$ plane by an RF pulse, transverse magnetization will begin to precess at the Larmor frequency. Due to magnetic inhomogeneities, the Larmor frequency of spins will cover a range of values centred about v_0. As a result, transverse magnetization will dephase and lose coherence over time as depicted in figure 1.6. If signal were to be acquired at any time point after the excitation pulse the signal would be weighted by T_2^* relaxation. To eliminate relaxation effects due to static inhomogeneities, i.e. T_2', a 180° refocussing pulse is applied at a time τ after excitation. The refocussing pulse will flip the dephasing spins about the x_ρ-axis (for a $180^\circ{}_Y$ pulse following a $90^\circ{}_X$ pulse). The spins will continue precessing at their previous frequencies and rephase at a time 2τ(3,38). Signal acquired from a spin echo will have decayed exclusively by T_2 relaxation. See figure 1.6 for an illustrated example of a spin echo.

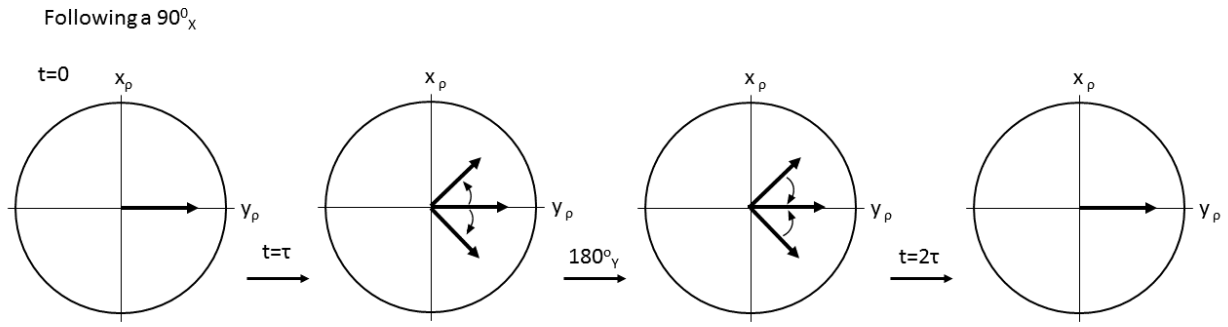

Figure 1.6– The creation of a spin echo. Following a$90^{\circ}{}_{X}$ excitation pulse M_0 is rotated into the transverse plane. As time elapses M_{XY} dephases due to differences in resonant frequencies. At time τ, a$180^{\circ}{}_{Y}$ refocusing pulse flips magnetization about the y_{ρ}-axis. After the refocusing pulse the spins continue to rotate at the same frequency and rephase at time 2τ, forming a spin echo.

1.6.2 – The Stimulated Echo

A stimulated echo is created by three successive 90° pulses(36). In fact, any pulse sequence with at least three RF pulses has the possibility of creating a stimulated echo(39). The first $90^{\circ}{}_{X}$ pulse tips M_0 into the $x_{\rho}y_{\rho}$ plane. During a time τ the transverse magnetization will dephase. A second $90^{\circ}{}_{X}$ pulse is applied to rotate spin isochromats[4] about the x_{ρ}-axis into the $x_{\rho}z_{\rho}$ plane. Any x_{ρ}- components of the isochromats will remain unchanged by a rotation about

[4] Any group of spins with equal phase.

x_ρ, due to this a stimulated echo has a maximum amplitude of $\frac{1}{2}M_0$(40). After the second $90°_X$ pulse a spoiler gradient is used to dephase the magnetization in the transverse plane. The third $90°_X$ pulse rotates the magnetization along the z_ρ back into the transverse plane. After time τ a stimulated echo will be formed(36,39). It should be noted that in addition to the stimulated echo, the sequence of $90°$ pulses also creates up to four spin echoes(39). Judicious choice of acquisition timing and spoiler gradients alleviates the risk of signal contamination by spin echoes(39).

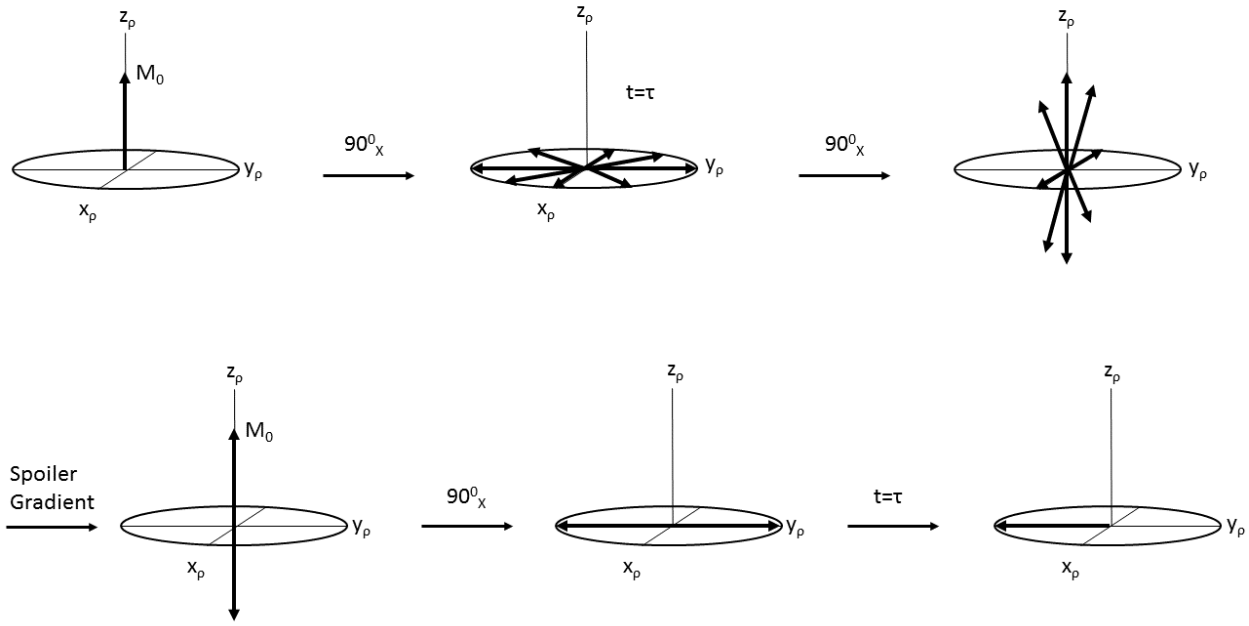

Figure 1.7– Creation of a stimulated echo. Following a$90°_X$ excitation pulse M_0 is rotated into the transverse plane. As time elapses M_{XY} dephases due to differences in resonant frequencies during a time τ**.** Another $90°_X$ pulse rotates all transverse magnetization into the $z_\rho x_\rho$ plane. A spoiler gradient is used to dephase all transverse components. Another $90°_X$ rotates the magnetization into the transverse plane. After a time τspins rephase and a stimulated echo is formed. Adapted from references(36,39).

1.7 – Spatial Localization

Spatial localization of MRS signal is required to extract useful diagnostic information *in vivo*. Without localization, spectroscopic techniques would be unable to probe and differentiate separate *in-vivo* tissues. Localization is achieved by the simultaneous application of frequency selective RF pulses and magnetic field gradients – denoted as G_X, G_Y and G_Z – resulting in slice selective RF pulses(36). In the absence of magnetic field gradients and other magnetic perturbations all spins of a given species resonate at the same Larmor frequency according to equation (1.10). Gradient coils produce a varying magnetic field that depend on position within the magnet bore. For the sake of simplicity we will only address linear gradient fields in the x, y, or z directions. When a gradient coil is active a magnetic field is produced such that(36)

$$B(r) = B_0 + G \bullet r, \tag{1.22}$$

where r, is the distance from isocentre[5] (defined as $r = 0$) and G_X is the gradient strength in units of $\frac{mT}{m}$. As a consequence of equation (1.22) the resonant frequency of spins will now be dependent on position such that

$$v(r) = \gamma(B_0 + Gr)$$

$$= v_0 + \gamma G r. \tag{1.23}$$

Thus, in the presence of a gradient field in one direction, all spins with the same position r will precess at the same frequency. When a magnetic field gradient is used in conjunction with a

[5] Isocentre is defined as the centre of the static magnetic field.

frequency selective RF pulse the pulse will only affect spins in a certain layer or "slice" of the phantom or patient(36). The width of the affected slice depends on both the range of frequencies contained in the pulse, given by its bandwidth (BW), and the strength of the gradient field, G. The bandwidth of the pulse can be related to the frequencies of the spins due to the gradient (3) so that

$$BW = \gamma G \Delta r, \tag{1.24}$$

where Δr is the width of the slice. Figure 1.8 illustrates the concept. For example, the width of slice in the z-direction given a gradient strength of $10\,\frac{mT}{m}$ and a bandwidth of $1000\ Hz$ is

$$\Delta z = \frac{BW}{\gamma G_Z} = \frac{1000\ Hz}{42.6\,\frac{MHz}{T} \bullet 100\frac{mT}{m}} = 2.34\ cm.$$

The position of a slice is determined by the offset frequency of the RF pulse and can be determined from equation (1.23) such that

$$r_{offset} = \frac{v_{offset} - v_0}{\gamma G}.$$

So, to centre the slice at the isocentre an offset frequency of v_0 is used.

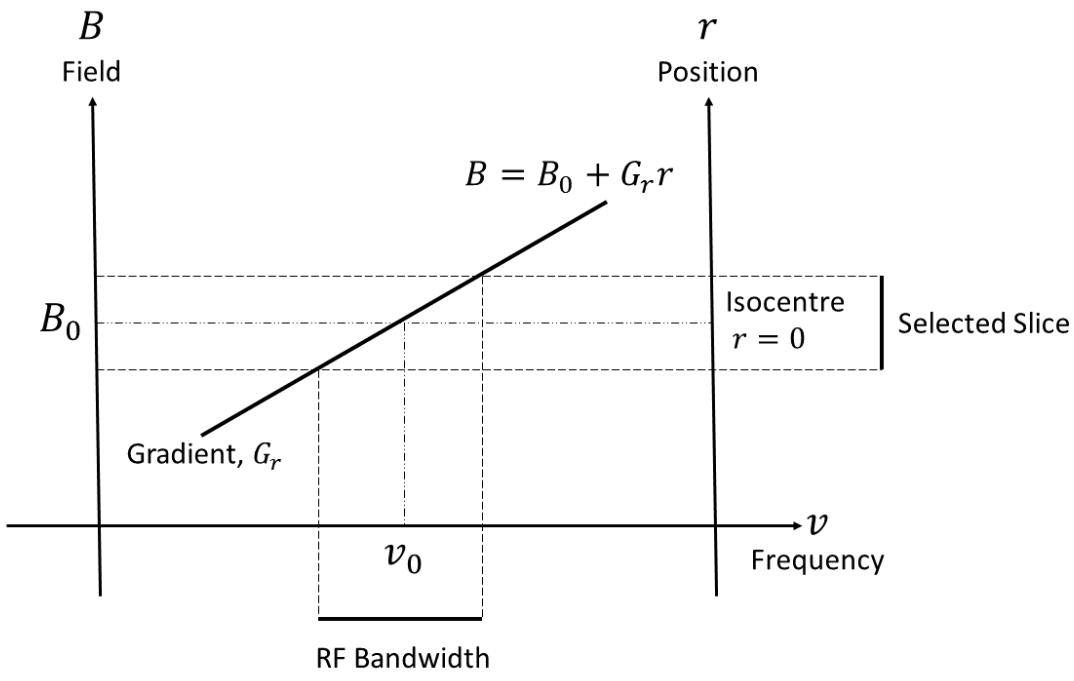

Figure 1.8– Relationship between the magnetic field seen by spins in the presence of a gradient, their resonant frequency and position. In the presence of a gradient, a frequency selective RF pulse will affect a slice with a width that is determined by the pulses bandwidth and the gradient's strength as illustrated.

1.8 Chemical Shift Displacement

Slice selection is possible because of the relationship between position and resonant frequency created by gradient fields. However, not all protons resonate at the same Larmor frequency due to chemical shift. The differences in resonant frequency result in a spatial offset of signal originating from protons with different chemical shifts when using spatially localized spectroscopy techniques. This effect is known as chemical shift displacement(3).To illustrate the concept we consider two protons on different molecules – water protons and $1.3\ ppm$ lipid

methylene protons which have a chemical shift difference of $434.5\ Hz$at $3\ T$. Now consider the frequency selective RF pulse from the previous section with a bandwidth of $1000\ Hz$ and the use of a z-gradient of strength $10\ \frac{mT}{m}$. If the offset of the RF pulse is centred on water protons at isocentre, then the frequencies over which the RF pulse is effective corresponds to a slice of water protons $2.34\ cm$ thick centred at isocentre. The RF pulse also affects the lipid methylene protons that fall within the same frequency range in a slice that is $2.34\ cm$ thick. However, due to the chemical shift difference between the methylene protons and the water protons, the result is a slice that is displaced from the slice selected for the water protons – the chemical shift displacement. The magnitude of the chemical shift displacement in the z-direction of a cubic voxel (created by the use of three orthogonal gradients) can by calculated by(3)

$$Chem\ Shift_Z = \frac{v}{BW} V_Z, \tag{1.25}$$

where V_Z is the size of the voxel in the z-direction. The same effect will occur in any direction depending on the direction of the gradient being used.

1.9 – Pulse Sequences

The research contained in this thesis employs two commonly used localized spectroscopy pulse sequence: Point RESolved Spectroscopy and STimulated Echo Acquisition Mode. PRESS acquires signal by use of a double spin echo created by a $90° - 180° - 180°$ pulse sequence whereas STEAM acquires signal from a stimulated echo created by a $90° - 90° - 90°$ pulse sequence. The design differences result in both distinct and subtle

consequences on the acquired signal. The selection of one of these scans over the other depends on experimental criteria. For example, the 90° pulses of STEAM allow a smaller minimum echo time (TE), ($\sim 20\,ms$) than that achievable using PRESS ($\sim 30\,ms$). However, STEAM is only capable of producing a maximum of half the maximum signal produced by PRESS due to the nature of the stimulated echo(39). Additionally, J-coupling evolution differs under each of these pulse sequences which will be discussed later in this thesis.

1.9.1 – Point RESolved Spectroscopy (PRESS)

PRESS(16) is a double spin echo spectroscopy technique which acquires signal from a localized cubic voxel. PRESS employs one 90° slice selective excitation pulse followed by two 180° slice selective refocussing pulses. During each of these pulses gradients in the $x, y,$ and$z$ direction are applied resulting in each pulse affecting spins in mutually orthogonal rectangular slabs. The intersection of these rectangular slabs forms a cubic voxel which is affected by all three pulses and is the origin of the acquired signal. The double spin echo is formed at a time $TE = TE_1 + TE_2$. Crusher gradients are employed to dephase any undesired signal generated by imperfections of the 180°refocussing pulses. Additionally, signal suppression pulses may be used outside of the voxel to spoil any signal originating exterior of the voxel. Figure 1.9 is a detailed illustration of the PRESS pulse sequence.

The equation describing the signal produced by PRESS and its dependence on echo time and repetition time (TR)[6] is given by(40)

$$S(TE) = S_0 \left(1 - 2e^{\left(-\frac{\left(TR - \frac{TE}{2} \right)}{T_1} \right)} + e^{\left(-\frac{TR}{T_1} \right)} \right) e^{\left(-\frac{TE}{T_2} \right)}, \quad (1.25)$$

where $S(TE)$ is the signal at time TE, S_0 is the signal at time $TE = 0$, and TR is the repetition time. For the case when $TE \ll TR$, equation (1.25) simplifies to

$$S(TE) = S_0 \left(1 - e^{\left(-\frac{TR}{T_1} \right)} \right) e^{\left(-\frac{TE}{T_2} \right)}. \quad (1.26)$$

[6] Repetition time is the amount of time between the initial pulses of consecutive sequences. Potential signal is maximized by making TR long enough for complete T_1 relaxation.

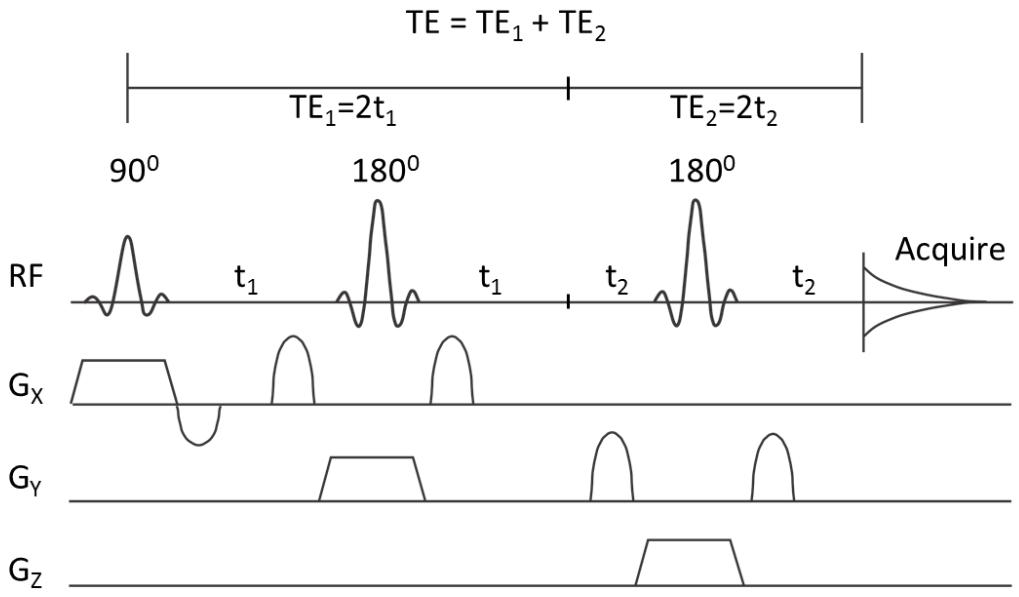

Figure 1.9- Point RESolved Spectroscopy (PRESS) pulse sequence diagram. A frequency selective 90°excitation pulse and two frequency selective 180° refocusing pulses are used in the presence of orthogonal gradients to create a double spin echo in a voxel of interest at time TE. Crusher gradients are used on either side of the refocusing pulses to dephase unwanted signal. Adapted from reference (3).

1.9.2 – STimulated Echo Acquisition Mode (STEAM)

STEAM(17) is a stimulated echo spectroscopy technique which acquires signal from a localized cubic voxel. STEAM employs three 90° slice selective excitation pulses. Gradients in the x, y, and$z$ direction are applied in conjunction with each of the pulses causing each pulse to affect spins in mutually orthogonal rectangular slabs. The intersection of the rectangular slabs forms a cubic voxel which is affected by all three pulses and is the origin of the acquired signal.

The stimulated echo is formed at a time TE. In addition to a stimulated echo, spin echoes are produced by this pulse sequence. Careful timing and crusher gradients are required to acquire only signal from the stimulated echo. The mixing time (TM) is the period of time when magnetization is stored as longitudinal magnetization. Crusher gradients are employed to dephase any undesired signal before the second $90°$ pulse and after the final $90°$ pulse and during TM. Additionally, signal suppression pulses may be used outside of the voxel to spoil any signal originating exterior of the voxel. Figure 1.10 is a detailed illustration of the STEAM pulse sequence.

The equation describing the signal produced by STEAM and its dependence on TE, TM and TR is given by(41)

$$S(TE) = \frac{S_0}{2}\left(1 - e^{\left(-\frac{\left(TR - TM - \frac{TE}{2}\right)}{T_1}\right)}\right)e^{\left(-\frac{TM}{T_1}\right)}e^{\left(-\frac{TE}{T_2}\right)}. \quad (1.27)$$

For the case when $TE + TM \ll TR$, equation (1.27) simplifies to

$$S(TE) = \frac{S_0}{2}\left(1 - e^{\left(-\frac{TR}{T_1}\right)}\right)e^{\left(-\frac{TM}{T_1}\right)}e^{\left(-\frac{TE}{T_2}\right)}. \quad (1.28)$$

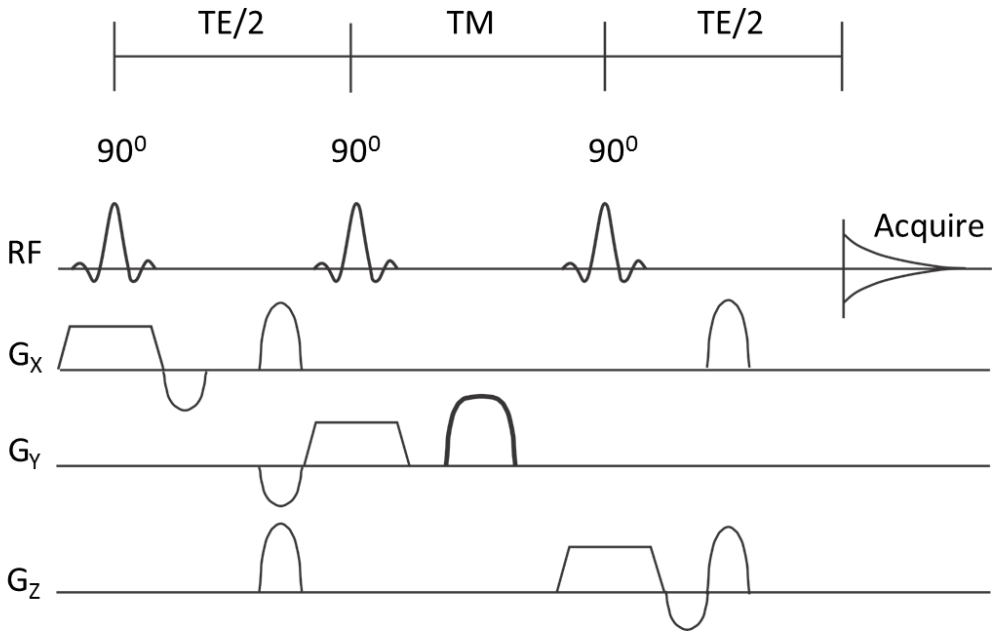

Figure 1.10– Stimulated Echo Acquisition Mode (STEAM) pulse sequence diagram. Three frequency selective 90°excitation pulses are used in the presence of orthogonal gradients to create a stimulated echo in a voxel of interest. Crusher gradients are used before the second RF pulse, after the third RF pulse and during the mixing time to dephase unwanted signal. Adapted from reference(3).

1.10 – J-Coupling

J-coupling, also known as scalar coupling, is another aspect of a spin's magnetic environment which needs to be addressed in spectroscopy. J-coupling is the phenomenon by which two spins interact magnetically through the electrons in chemical bonds(3,42). The interaction causes a splitting of the two energy levels seen in section 1.2.3 which consequently produces more than one resonant frequency for coupled spins (42). In an MR spectrum, this manifests as peak splitting in the peaks of coupled spins. The strength of a J-coupling interaction is measured by the constant J in units of Hz and is appropriately termed the J-coupling constant. For proton-proton interactions, J-coupling constants are on the order of $1 - 15\ Hz$ and only interactions as far as three bonds away are considered significant(3) J-coupling interactions are defined as either *weakly* or *strongly* coupled based on the ratio of $\frac{J}{\delta}$, where δ is the chemical shift difference between the coupled spins(42). An interaction is considered weakly coupled if $\frac{J}{\delta} \sim < 0.10$(42). The simplest weakly coupled spin system is denoted as anAX spin system. With the mentioned notation, A and X each represent a singular spin with distinct resonant frequency. An AX_2 system would involve one spin of a given chemical shift weakly interacting with *two* equivalent spins with a distinct chemical shift from that of A. The splitting phenomenon of weakly coupled interactions is more structured than that of strong coupling. The peak areas of the split resonances follow a binomial pattern(3) as stated in Table 1.1. Figure 1.11 illustrates the splitting pattern of AX and A_2X_2 spin systems.

Spin System	Number of $\boldsymbol{A}$ Peaks	Number of $\boldsymbol{X}$ Peaks	Area Ratios of $\boldsymbol{A}$ Peaks	Area Ratios of $\boldsymbol{X}$ Peaks
$\boldsymbol{A}$	1	0	1	0
$\boldsymbol{AX}$	2	2	1:1	1:1
$\boldsymbol{AX_2}$	3	2	1:2:1	1:1
$\boldsymbol{AX_3}$	4	2	1:3:3:1	1:2:1
$\boldsymbol{A_2X_2}$	3	3	1:2:1	1:2:1

Table 1.1 – Splitting patterns of weakly coupled spins.

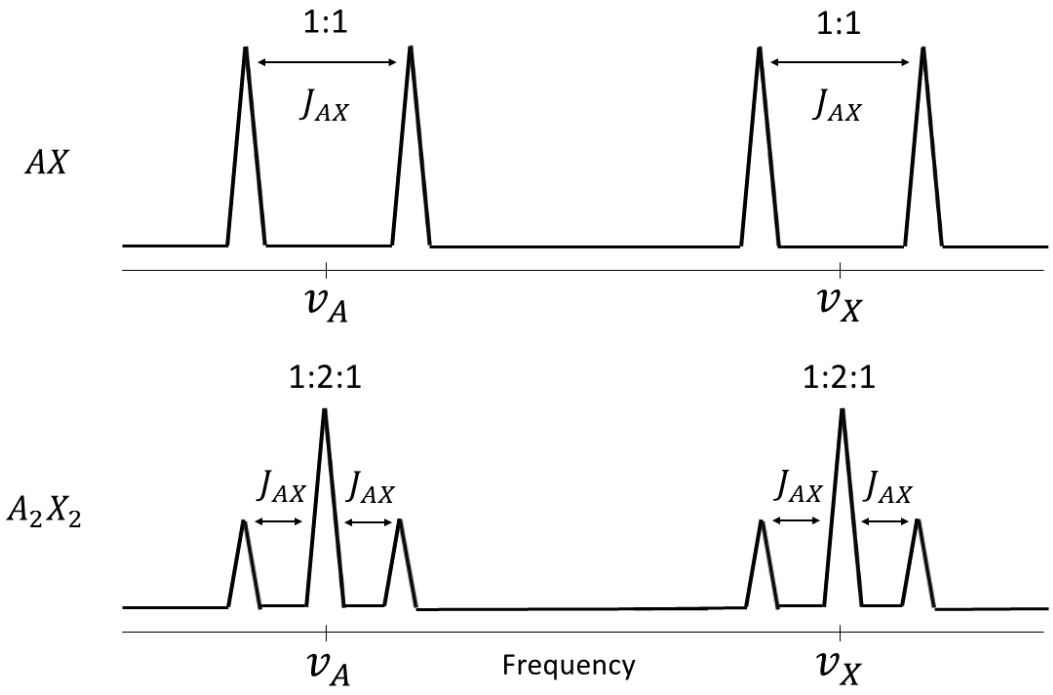

Figure 1.11– The spectral appearance of A and X spins of weakly coupled AX and A_2X_2 spin systems. The peaks are separated by a frequency equal to the coupling strength of the spins. The ratio of peak heights follows a binomial distribution.

1.11 – J-Coupling Evolution During PRESS and STEAM

Another consequence of J-coupling is the modulation of acquired signal from coupled spins as a function of TE(42). The details of this modulation will depend on the strength of the coupling interaction, the number of spins involved as well as the pulses used in the spectroscopy technique. Due to the different pulses and physical mechanisms used in PRESS and STEAM, coupled spins evolve differently in response to each sequence. For PRESS, the acquired signal for either spin A or X of a weakly coupled AX spin system is given by(42)

$$S(TE) = S_0[\cos(\pi J_{AX} TE)]e^{-TE/T_2}, \quad (1.29)$$

where J_{AX} is the coupling constant of the AX spin system and T_2 is the transverse relaxation time constant for the spin of interest. The analogous equation for STEAM is given by(42)

$$S(TE, TM) = \frac{S_0}{2}\left[cos^2\left(\frac{\pi J_{AX}\, TE}{2}\right) - \frac{1}{2}sin^2\left(\frac{\pi J_{AX}\, TE}{2}\right) * \right.$$

$$\left.\left[1 - cos\left(\frac{\delta_{AX}\, TE}{2}\right)\right]\cos(\delta_{AX} TM)\right] e^{-TE/T2}, \quad (1.30)$$

where TM is the mixing time parameter and δ_{AX} is the chemical shift difference between A and X. Figure 1.12 illustrates the evolution of anAX spin system in the absence of relaxation effects for an AX spin system under PRESS and STEAM.

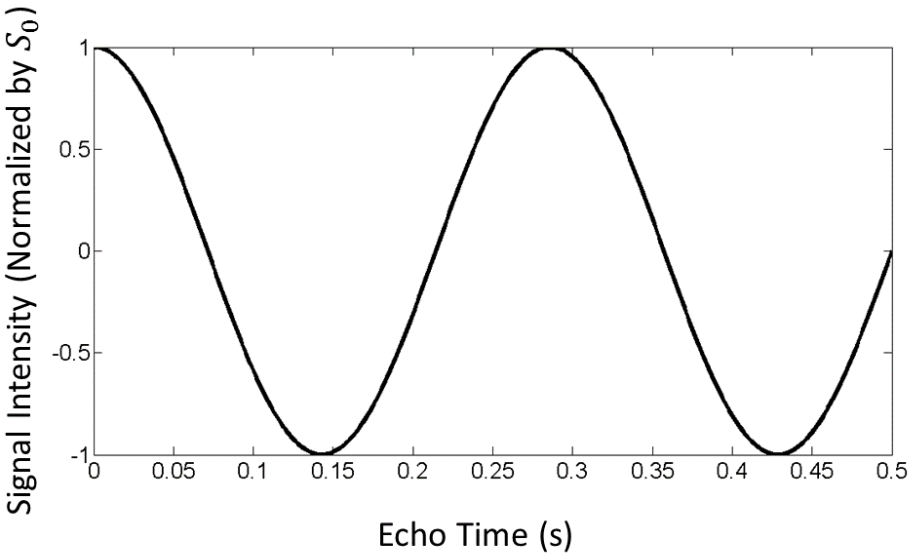

Figure 1.12

a. Signal evolution of spin A of a weakly coupled AX spin system using a PRESS sequence in the absence of relaxation. The relevant parameters are $J_{AX} = 7\ Hz$, and $\delta_{AX} = 50\ Hz$.

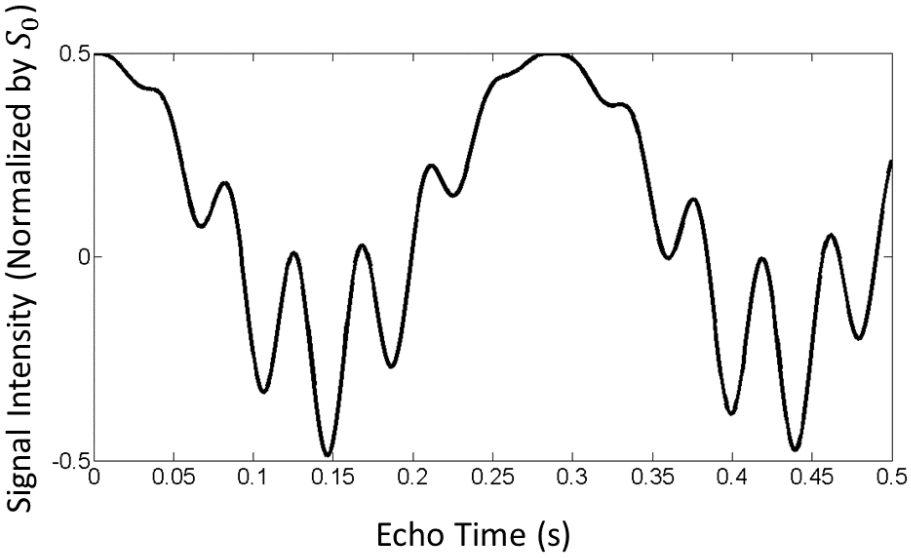

b. Signal evolution of spin A of a weakly coupled AX spin system using a STEAM sequence in the absence of relaxation. The relevant parameters are $TM = 50\ ms$, $J_{AX} = 7\ Hz$, and $\delta_{AX} = 50\ Hz$.

1.12 – References

1. Rabi I, Millman S, Kusch P. The Molecular Beam Resonance Method for Measuring Nuclear Magnetic Moments. *Physical Review* 1939; **55**.
2. Proctor W, Yu F. The Dependence of a Nuclear Magnetic Resonance Frequency Upon Chemical Compound. *Physical Review* 1950; **77**.
3. de Graaf R. *In Vivo* NMR Spectroscopy: John Wiley & Sons Ltd.; 2007.
4. Chernov MF, Hayashi M, Izawa M, Ono Y, Hori T. Proton magnetic resonance spectroscopy (MRS) of metastatic brain tumors: variations of metabolic profile. *Int J Clin Oncol* 2006; **11**: 375-384.
5. Kumar M, Jagannathan NR, Seenu V, Dwivedi SN, Julka PK, Rath GK. Monitoring the therapeutic response of locally advanced breast cancer patients: sequential in vivo proton MR spectroscopy study. *J Magn Reson Imaging* 2006; **24**: 325-332.
6. Oriol A, Valverde D, Capellades J, Cabañas ME, Ribera JM, Arús C. In vivo quantification of response to treatment in patients with multiple myeloma by ^{1}H magnetic resonance spectroscopy of bone marrow. *Magn Reson Mater Phy* 2007; **20**: 93-101.
7. Qi J, Fong Y, Saltz L, D'Angelica MI, Kemeny NE, Gonen M, Shia J, Shukla-Dave A, Jarnagin WM, Do RKG, Schwartz LH, Koutcher JA, Zakian KL. Serial measurement of hepatic lipids during chemotherapy in patients with colorectal cancer: a ^{1}H MRS study. *NMR Biomed* 2013; **26**: 204-212.
8. Borra R, Lautamäki R, Parkkola R, Komu M, Sijens PE, Hällsten K, Bergman J, Iozzo P, Nuutila P. Inverse association between liver fat content and hepatic glucose uptake in patients with type 2 diabetes mellitus. *Metabolism* 2008; **57**: 1445-1451.
9. Kotronen A, Juurinen L, Tiikkainen M, Vehkavaara S, Yki-Järvinen H. Increased liver fat, imparied insulin clearance, and hepatic adipose tissue insulin resistance in type 2 diabetes. *Gastroenterology* 2008; **135**: 122-130.
10. Perseghin G, Scifo P, De Cobelli F, Pagliato E, Battezzati A, Arcelloni C, Vanzulli A, Testolin G, Pozza G, Del Maschio A, Luzi L. Intramyocellular triglyceride content is a determinant of in vivo insulin resistance in humans. *Diabetes* 1999; **48**: 1600-1606.

11. Chabanova E, Bille DS, Thisted E, Holm JC, Thomsen HS. ^{1}H MRS assessment of hepatic steatosis in overweight children and adolescents: comparison between 3T and open 1T MR-systems. *Abdom Imaging* 2013; **38**: 315-319.

12. Hayashi N, Miyati T, Minami T, Takeshita Y, Ryu Y, Matsuda T, Ohno N, Hamaguchi T, Kato K, Takamura T, Matsui O. Quantitative analysis of hepatic fat fraction by single-breath-holding MR spectrscopy with T_2 correction: phantom and clinical study with histologic assessment. *Radiol Phys and Technol* 2013; **6**: 219-225.

13. Griffith JF, Yeung DKW, Antonio GE, Lee FKH, Hong AWL, Wong SYS, Lau EMC, Leung PC. Vertebral bone mineral density, marrow perfusion, and fat content in healthy men and men with osteoporosis: dynamic contrast-enhanced MR imaging and MR spectroscopy. *Radiology* 2005; **236**: 945-951.

14. Li X, Kuo D, Schafer AL, Porzig A, Link TM, Black D, Schwartz AV. Quantification of vertebral bone marrow fat content using 3 Tesla MR spectroscopy: reproducibility, vertebral variation, and applications in osteoporosis. *J Magn Reson Imaging* 2011; **33**: 974-979.

15. Smith IC, Princz EJ, Saunders JK. Magnetic resonance spectroscopy in cancer research. *Can Assoc Radiol J* 1990; **41**: 32-38.

16. Bottomley P. Selective volume method for performing localized NMR spectrscopy. *US patent 4,480,228* 1984.

17. Frahm J, Merboldt K, Hanioke W. Localized proton spectroscopy using stimulated echoes. *J Magn Reson* 1987; **72**: 502-508.

18. Venkatesh BA, Lima JAC, Bluemke DA, Lai S, Steenbergen C, Liu CY. MR proton spectroscopy for myocardial lipid deposition quantification: a quantitative comparison between 1.5T and 3T. *J Magn Reson Imaging* 2012; **36**: 1222-1230.

19. Hamilton G, Middleton MS, Bydder M, Yokoo T, Schwimmer JB, Kono Y, Patton HM, Lavine JE, Sirlin CB. Effect of PRESS and STEAM sequences on magnetic resonance spectroscopic liver fat quantification. *J Magn Reson Imaging* 2009; **30**: 145-152.

20. Oostendorp M, Engelke UFH, Willemsen MAAP, Wevers RA. Diagnosing inborn errors of lipid metabolism with proton nuclear magnetic resonance spectroscopy. *Clin Chem* 2006; **52**: 1395-1405.
21. Stokes AM, Feng Y, Mitropoulos T, Warren WS. Enhanced refocusing of fat signals using optimized multipulse echo sequences. *Magn Reson Med* 2013; **69**: 1044-1055.
22. Henkelman RM, Hardy PA, Bishop JE, Poon CS, Plewes DB. Why fat is bright in RARE and fast spin-echo imaging. *J Magn Reson Imaging* 1992; **2**: 533-540.
23. Melki P, Mulkern R, Lawrence P, Jolesz F. Comparing the FAISE Method with Conventional Dual-Echo Sequences. *Journal of Magnetic Resonance Imaging* 1991; **1**: 319-326.
24. Constable R, Anderson A, Zhong J, Gore J. Factors Influencing Contrast In Fast Spin-Echo MR Imaging. *Magnetic Resonance Imaging* 1992; **10**: 497-511.
25. Peled S, Williamson D, Mulkern R. Signal Intensity Studies of Strongly-Coupled Spin Systems during CPMG/RARE Imaging Sequences. *Proceedings of the Society of Magnetic Resonance Third Scientific Meeting* 1995: 655.
26. Williamson D, Mulkern R, Jakab P, Jolesz F. Coherence Transfer by Isotropic Mixing in Carr-Purcell-Meiboom-Gill Imaging: Implications for the Bright Fat Phenomenon in Fast Spin-Echo Imaging. *Magnetic Resonance in Medicine* 1996; **35**: 506-513.
27. Hinks R, Martin D. Bright Fat, Fast Spin Echo, and CPMG. *Proceedings of the Society of Magnetic Resonance in Medicine 11th Annual Meeting* 1992: 4503.
28. Rutt B, Wright G. Lipid Signal Enhancement in CPMG MRI: Effect of Field Strength. *Proceedings of the Society of Magnetic Resonance in Medicine 11th Annual Meeting* 1992: 4504.
29. Wright G, Macovski A. Lipid Signal Enhancement in Spin-Echo Trains. *Proceedings of the Society of Magnetic Resonance in Medicine 11th Annual Meeting* 1992: 437.
30. Gajdošík M, Chmelík M, Just-Kukurová I, Bogner W, Valkovič L, Trattnig S, Krššák M. In vivo relaxation behavior of liver compounds at 7 Tesla, measured by single-voxel proton MR spectroscopy. *J Magn Reson Imaging* 2014; **40**: 1365-1374.

31. Yahya A, Fallone BG. T_2 determination of the J-coupled methyl protons of lipids: in vivo ilustration with tibial bone marrow at 3 T *J Magn Reson Imaging* 2010; **31**: 1514-1521.
32. Tipler P, Llewellyn R. Modern Physics. New York: W. H. Freeman and Company; 2002.
33. Giancoli D. Physics for Scientists and Engineers. New Jersey: Prentice Hall; 2000.
34. Schroeder D. An Introduction to Thermal Physics: Addison Wesley Longman; 1999.
35. James T. Nuclear Magnetic Resonance In Biochemistry: Academic Press; 1975.
36. Callaghan P. Principles of Nuclear Magnetic Resonance Microscopy. Oxford: Oxford University Press; 1993.
37. Chavhan G, Babyn P, Thomas B, Shroff M, Haacke E. Principles, Techniques and Applications of T2* - based MR Imaging and Its Special Applications. *Radiographics* 2009; **29**: 1433 - 1449.
38. Hahn E. Spin Echoes. *Physical Review* 1950; **80**: 580-594.
39. Burstein D. Stimulated Echoes: Description, Applications, Practical Hints. *Concepts in Magnetic Resonance* 1996; **8**: 269-278.
40. Traber F, Block R, Lamerichs J. ^{1}H Metabolite Relaxation Times at 3.0 Tesla: Measurements of T_1 and T_2 Values in Normal Brain and Determinaton of Regional Differences in Transverse Relaxation. *Journal of Magnetic Resonance Imaging* 2004; **19**: 537-545.
41. Helms G. Analysis of 1.5 Tesla Proton MR Spectra of Human Brain Using LCmodel and an Imported Basis Set. *Magnetic Resonance Imaging* 1999; **17**: 1211-1218.
42. de Graaf R, Rothman D. *In Vivo* Detection and Quantification of Scalar Coupled ^{1}H NMR Resonances. *Concepts in Magnetic Resonance* 2001; **13**: 32-76.
43. Allerhand A. Analysis of Carr-Purcell Spin-Echo NMR Experiments on Multiple-Spin Systems. *The Journal of Chemical Physics* 1966; **44**: 1-9.

Chapter 2 –Background Information and Experimental Methods

2.1 – Introduction

The primary objective of the work presented in this thesis is to investigate the effects of J-coupling evolution on the quantification of the$1.3\ ppm$ lipid methylene resonance and the estimation of its T_2 value by proton MRS. The goal is approached via the modification of a standard PRESS sequence. By employing refocussing pulses with bandwidths less than or equal to the chemical shift difference between the $1.3\ ppm$ lipid methylene protons and the lipid proton groups to which they are coupled, the signal evolution due to J-coupling can be rewound. The method was previously used to rewind the J-coupling evolution of the$0.9\ ppm$ methyl protons(1)there by improving their quantification. The present chapter focuses on a discussion of the information relevant to the understanding of the project, its motivation, and the experimental and analysis methods.

2.2 – Lipids

2.2.1 – Definition and Chemical Structure of Lipids

Lipids are naturally occurring substances that include fats, waxes, greases and other chemically similar substances(2). One of the main lipids found in humans are fats contained in adipose tissue and bone marrow. One example of fats is triglycerides, which are formed from a glycerol backbone and three fatty acids. Fatty acids consist of a carboxylic acid (COOH) molecule connected to a chain of carbon-hydrogen (CH_n) groups. Linoleic, oleic, and palmitic

acid, the molecular structures of which are illustrated in figure 2.1, are examples of common fatty acids found *in vivo*(3). There are two kinds of fatty acids, namely, saturated and unsaturated. Saturation refers to the number of hydrogen atoms which are bound to each carbon atom relative to the maximum number of hydrogen atoms that are able to be bound. A saturated fatty acid, such as palmitic acid has the maximum number of hydrogen atoms as possible on each carbon atom and thus contains no carbon-carbon double bonds. Unsaturated fatty acids, such as oleic or linoleic acid, do contain carbon-carbon double bonds.

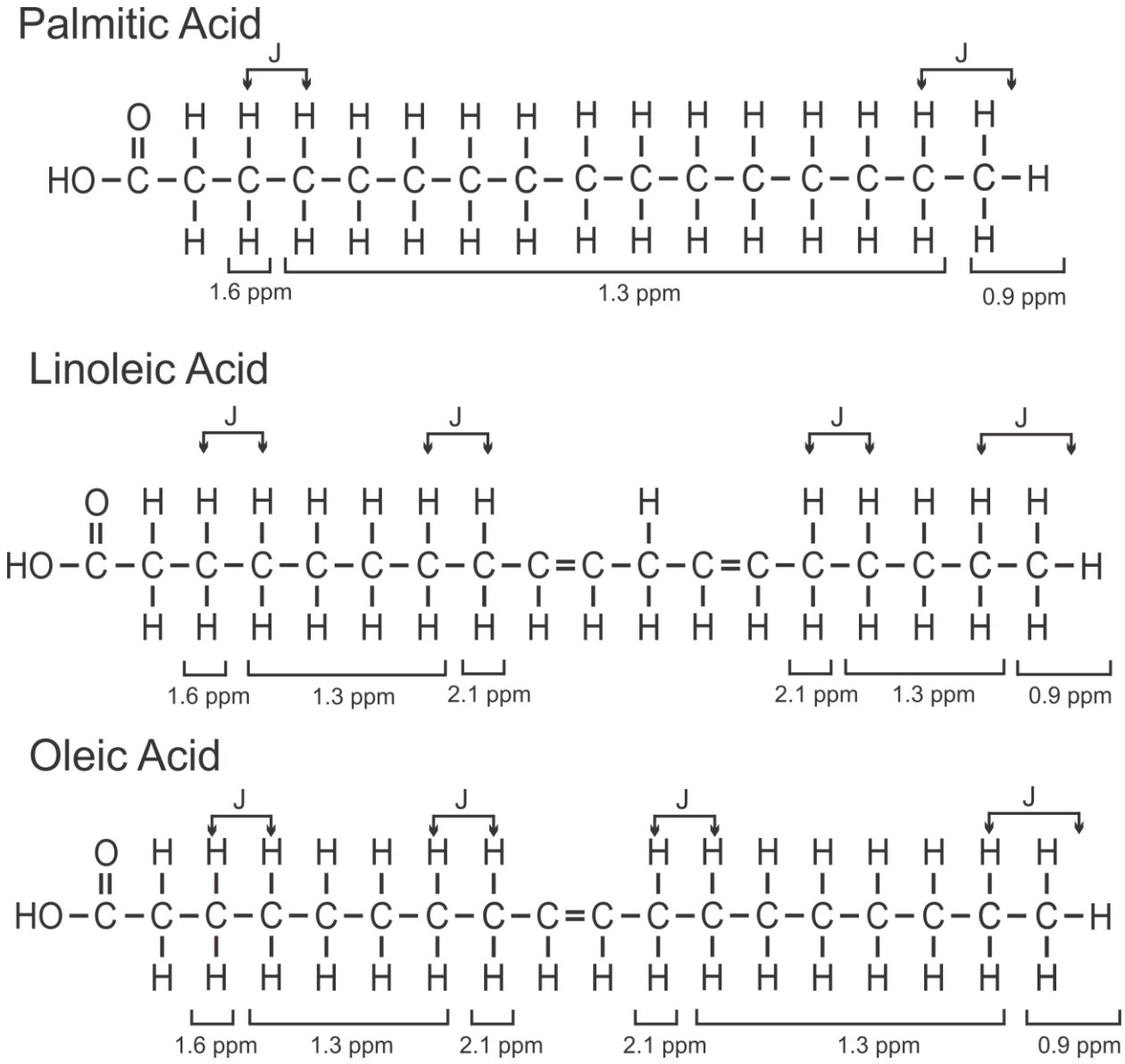

Figure 2.1 – Molecular structures of palmitic, linoleic and oleic acid. The J-coupling interactions of the $1.3\ ppm$ methylene protons are indicated by J.

2.2.2 - Relevance of the$1.3\ ppm$ Methylene Protons

Quantification of the$1.3\ ppm$ lipid methylene signal is an active field of research in medicine due to the observation of changes in lipid levels in disease. Proton MRS can detect changes in $1.3\ ppm$ lipid methylene levels and has been used to study cancer(4-7), liver disease(8,9), osteoporosis(10,11) and diabetes(12-14). For example, Oriol et al.(6) found in a study of 16 patients being treated for multiple myeloma with chemotherapy that eight out of eight patients classified as completely responsive, and three out of four patients classified as partially responsive to the treatment, presented an increase in the $1.3\ ppm$ lipid methylene signal as quantified using a lipid-water ratio. Four out of four patients who were non-responsive showed no increase in $1.3\ ppm$ lipid methylene signal. Chernov et al.(4) noted that metastatic brain tumours can be identified based on the presence of distinct $1.3\ ppm$ lipid methylene peaks relative to healthy brain tissue and primary brain tumours. Furthermore, Kumar et al.(5) observed a statistically significant increase in the fat to water ratio of breast tumours which decreased in volume in response to neo-adjuvant chemotherapy.

2.3 – J-Coupling of the $1.3\ ppm$ Methylene Protons

2.3.1 – J-Coupling Interactions

All protons in lipid molecules exhibit J-coupling interactions(15,16). The most relevant interactions to this thesis are those of the $1.3\ ppm$ methylene protons. Figure 2.1 illustrates all possible J-coupling interactions for $1.3\ ppm$ methylene protons found in fatty acids. The $1.3\ ppm$ methylene protons are weakly coupled to the $0.9\ ppm$ methyl protons and the

$2.1\ ppm$ allylic protons withJ/δ values of $\sim 0.13(1)$ and $\sim 0.07(17)$, respectively. The $1.3\ ppm$ methylene protons are also strongly coupled to the $1.6\ ppm$ methylene protons with a J/δ value of $\sim 0.18(17)$. For those fatty acids which do not contain a carbon-carbon double bond, such as palmitic acid as seen in figure 2.1, there are no $2.1\ ppm$ allylic protons.

2.3.2 – Signal Evolution of the$1.3\ ppm$ Methylene Protons

Despite the J-coupling interactions of the$1.3\ ppm$ methylene protons, signal acquired from the protons *in vivo*or from biologically representative phantoms decays nearly monoexponentially as a function of increasing echo time. In contrast, signal from $0.9\ ppm$ methyl protons displays marked signal modulation from J-coupling interactions. Figure 2.2a shows the decay of the $1.3\ ppm$ methylene proton signal acquired from a linoleic acid phantom, a fatty acid commonly found *in vivo*. Figure 2.2b demonstrated the decay of the $0.9\ ppm$ methyl proton signal acquired from a linoleic acid phantom as a function of echo time.

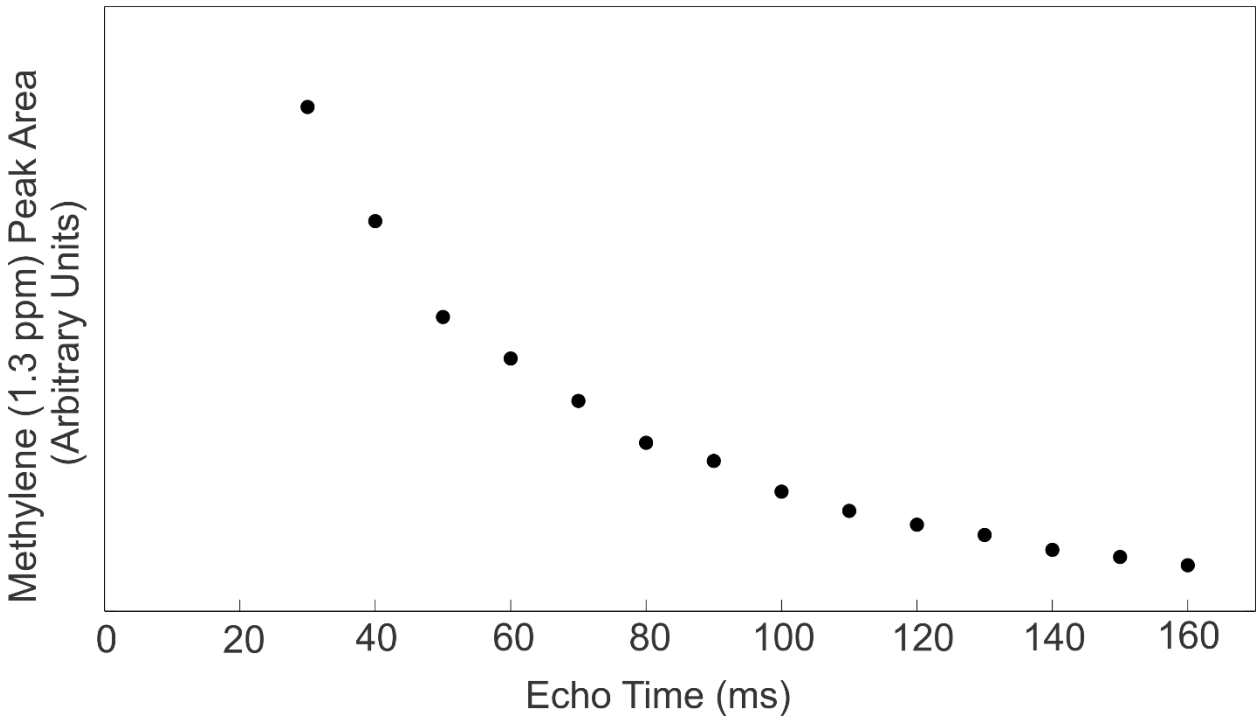

Figure 2.2

a. $1.3\ ppm$ methylene signal from linoleic acid acquired with a standard PRESS sequence as a function of TE at $3\ T$. Signal from the $1.3\ ppm$ methylene protons in linoleic acid decays nearly monoexponentially.

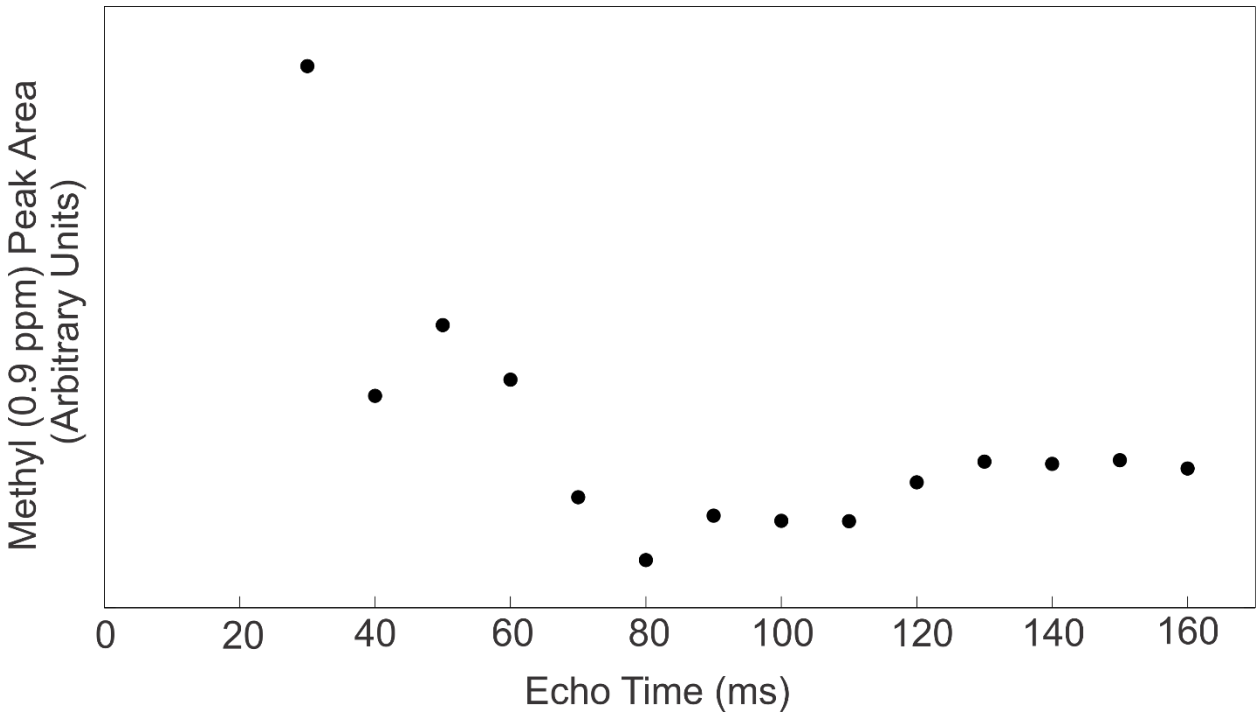

b. $0.9\ ppm$methyl signal from linoleic acid acquired with a standard PRESS sequence as a function of TE at $3\ T$. Signal from the $0.9\ ppm$ methyl protons in linoleic acid displays marked signal modulation due to J-coupling interactions.

2.4 – Lipid Quantification

2.4.1 – Quantification Method and Relaxation Effects

Various MRS methods of lipid quantification have been used and each method is selected based on a variety of concerns such as SNR, acquisition time and minimization of or compensation for relaxation effects. The use of a STEAM pulse sequence has the advantage over the PRESS sequence of a shorter minimum achievable echo time, the use of which minimizes signal loss from transverse relaxation and J-coupling effects. Furthermore, the choice

between acquisition using a single or multiple echo times exists for both pulse sequences. Often a single short TE is chosen to minimize transverse relaxation effects. Acquiring signal at multiple echo times, while extending the total scan time, allows for correction of transverse relaxation by fitting the data to a monoexponentially decaying function of the form $M_0 e^{-\left(\frac{TE}{T_2}\right)}$. Longitudinal relaxation effects can be accounted for by choosing a TR long enough to ensure sufficient longitudinal relaxation. Accounting or correcting for relaxation effects is crucial for accurate quantification.

2.4.2 – Fat-Water Ratio

The amplitude of the peaks in an MRS spectrum is influenced by a number of factors, some of which include: TE, TR, B_0, magnetic field shim, hardware and receiver gain. Additionally, different scanner software will display peak amplitudes using different scales. As a result, unless conditions are carefully controlled in every experiment, absolute quantification is impractical. Consequently, relative quantification is often employed by dividing measured peak heights or areas by the height or area of a reference peak. In fat quantification, a common reference peak used is water and so fat quantification is achieved by defining a fat-water ratio (FW)(5,6) or a fat fraction (FFW)(7-11,13):

$$FW = \frac{Area_{Fat}}{Area_{Water}} \tag{2.1}$$

$$FFW = \frac{Area_{Fat}}{Area_{Fat} + Area_{Water}} \tag{2.2}$$

2.4.3 – Effect of J-Coupling on Quantification

In addition to relaxation effects, the J-coupling interactions of lipid protons will modulate acquired signal as a function of TE, as seen in section 1.11 for PRESS and STEAM sequences. J-coupling evolution of *significant effect*, such as the evolution seen for the $0.9\ ppm$ lipid methyl protons, prevents an accurate monoexponential fit, resulting in inaccurate estimates of both M_0 and $T_2(1)$. Despite the perceived nearly monoexponential evolution of the $1.3\ ppm$ lipid methylene protons, the methods applied in this work aim to rewind the J-coupling evolution of the $1.3\ ppm$ methylene protons to determine the significance of J-coupling effects on the determination of M_0 and T_2. It should be noted that the complicated nature of spins with multiple coupling interactions, such as those of the 1.3 ppm lipid protons, may present signal modulation which is not readily predictable. The signal modulation of the 1.3 ppm lipid resonance is the sum of signal modulations of the many individual multiplet peaks which constitute the 1.3 ppm resonance.

2.4.4 – Previous Work on J-Coupling Effects on Observed Signal from the $1.3\ ppm$ Methylene Lipid Protons

The effects of J-coupling evolution on signal from the $1.3\ ppm$ methylene protons has been observed previously by a number of authors. MRI studies have qualitatively(18,19) or quantitatively(20-25) investigated the minimization of J-coupling effects on signal from fats, lipids or bone marrow when using a FSE(18,19,25) or CPMG(20-24) imaging sequence relative

to a conventional spin echo. The signal enhancement observed in these experiments is attributed to the dependence of J-coupling effects on the interpulse timing of 180° echo trains first noted by Allerhand (26). In spectroscopy, Hamilton et al. noted larger estimated values of T_2 for $1.3\,ppm$ methylene protons in animal fat acquired with STEAM compared to PRESS. T_2values of $84.9\,ms$ and $66.4\,ms$ were estimated using STEAM and PRESS, respectively, at $3\,T$. The difference was attributed to less J-coupling evolution of the $1.3\,ppm$ methylene protons during STEAM in comparison to PRESS. Despite the observation of J-coupling effects on the acquired signal from the $1.3\,ppm$ methylene protons, only one paper has been previously published attempting to correct for its effects(27). Gajdošík et al. attempted to correct for J-coupling effects on M_0 and T_2 estimation of all proton groups of *in-vivo* fatty acids by modifying the monoexponential equation used to fit data acquired with a PRESS sequence at $7\,T$. After modification, the equation(27)

$$M(TE) = M_0 e^{-(\frac{TE}{T_2})}[\cos(\pi TE J_{AX}) + b] \tag{2.3}$$

was used for fitting, where b is a constant. The cosine term of equation 2.3 corresponds to the cosine term in equation 1.29 which describes the J-coupling evolution of a weakly coupled AX spin system under PRESS. However, as seen in section 2.2.1, the$1.3\,ppm$ methylene protons and the other protons with which it interacts do not constitute anAX spin system. Due to the monoexponential behaviour (see figure 2.2) of the $1.3\,ppm$ methylene protons *in vivo*, the fitting method of equation (2.1), in comparison to the standard monoexponential fit, did not yield any differences in M_0 and T_2 estimations for the $1.3\,ppm$ methylene protons found in liver tissue.

2.5 – Rewinding J-Coupling Evolution

J-coupling evolution of weakly coupled spins can be rewound by the application of a PRESS sequence that employs refocussing pulses with a bandwidth equal to or smaller than the chemical shift difference between the spins of interest and the spins to which they are coupled. From this point forward the modified PRESS technique will be referred to as the "narrow bandwidth" method and "standard bandwidth" will be used in reference to a standard PRESS technique. The narrow bandwidth PRESS technique has been used previously to minimize the J-coupling evolution of coupled $0.9\ ppm$ lipid methyl protons(1).

2.5.1 – Chemical Shift Displacement, Voxel Size, RF Bandwidth and Chemical Shift

The narrow bandwidth PRESS technique exploits the chemical shift displacement effect (see section 1.8) to achieve selective refocussing of a single spin group(1,28,29). Recall that the chemical shift displacement (in any direction) between two spins with different chemical shifts is given by

$$Chem\ Shift\ = \frac{v}{BW} Voxel, \tag{2.4}$$

where v is the chemical shift difference between the coupled spins, in Hz, and $Voxel$ is the voxel size. It follows that if $BW \leq v$, then $Chem\ Shift \geq Voxel$. Thus, if we make the bandwidth of the refocussing pulses less than or equal to the chemical shift difference of the spins of interest and each of the proton groups to which they are coupled, the chemical shift displacement will be greater than or equal to the size of the voxel. Consequently, the

refocussing pulse will affect each proton group in non-overlapping regions of phantom or tissue. This is illustrated in figure 2.3 for two proton groups.

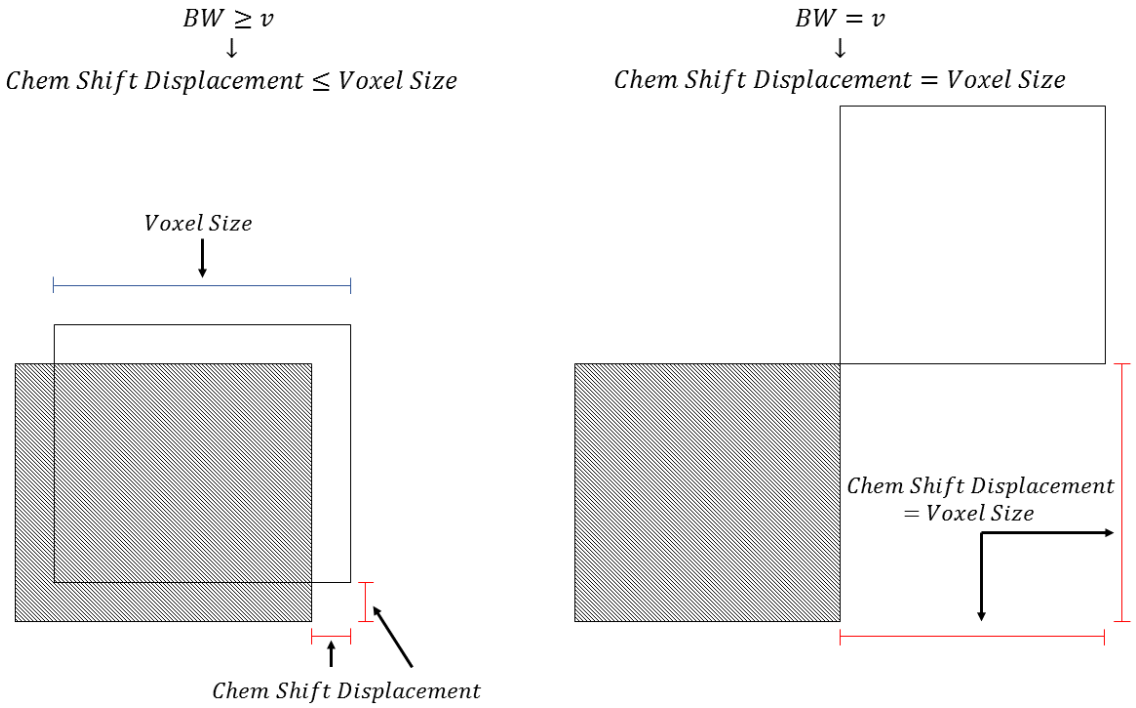

Figure 2.3 – Illustration of the relationship between chemical shift displacement, voxel size, RF bandwidth and chemical shift difference. The shaded box represents the spatial location of spins of one resonant frequency being affected by two RF pulses and the unshaded box represents the spatial location of spins of another resonant frequency being affected by the same pulses. The chemical shift difference between the two spin groups is v. When $BW = v$ there is no overlap between the regions since the chemical shift displacement is equal to the size of the voxel.

2.5.2 – Mechanism of the Narrow Bandwidth PRESS Technique

As discussed in section 1.10, J-coupling results in the existence of more than one resonant frequency among spins of a given group. For example, in an AX spin system the A spins will have two resonant frequencies spaced equally above and below the original Larmor frequency v: $v_{A\rightarrow X\alpha}$ which is greater than v and corresponds to A spins which are coupled to X spins in the α state, and $v_{A\rightarrow X\beta}$ which is less than v and corresponds to A spins which are coupled to X spins in the β state(30). After a ${90^\circ}_X$ pulse, in the absence of transverse relaxation effects, the two vectors $A_{X\alpha}$ and $A_{X\beta}$ will precess according to their Larmor frequencies, as seen in the second frame of figure 2.4a. The application of a ${180^\circ}_Y$ refocussing pulse of *standard bandwidth*, as seen in the third frame of figure 2.4a, will then flip $A_{X\alpha}$ and $A_{X\beta}$ about the y-axis. However, the intent of the refocussing pulse, which is to rewind the previous evolution of the spin isochromats, is not realized for J-coupling evolution. In addition to flipping the A spin vectors about the y-axis, a 180° pulse of *standard bandwidth* has sufficient bandwidth to affect both A and X spins and will therefore also invert the state of the X spins. As a result of the state inversion, the spins which were previously coupled to X spins in the α state will now be coupled to spins in the β state and vice versa. Consequently, the A spins which originally precessed at $v_{A\rightarrow X\alpha}$ before the refocussing pulse will now precess at $v_{A\rightarrow X\beta}$ and the A spins which originally precessed at $v_{A\rightarrow X\beta}$ will now precess at $v_{A\rightarrow X\alpha}$. After the refocussing pulse, the spin isochromats of A continue to dephase as depicted in the final frame of figure 2.4a. The use of a refocussing pulse with a bandwidth less than or equal to the chemical shift difference between A and X will not result in the same evolution. The use of the narrow bandwidth refocussing pulse will selectively refocus only A spins in the region initially

affected by the 90° pulse. The X spins which are affected by the narrow bandwidth refocussing pulse will be located in a region which does not overlap with the region of A spins due to the chemical shift displacement effect seen in figure 2.3. Thus, the X spins to which the A spins are coupled will not see the 180° pulse and their spin states will not be inverted. As a result, after the 180° pulse the spins will rephase as shown in figure 2.4b. It should be noted that this technique is only strictly valid for *weakly coupled* spin systems. The mechanism discussed here will be used to recover signal loss of the $1.3\ ppm$ methylene protons due to J-coupling in the experiments performed in the thesis. The signal recovered by the narrow bandwidth PRESS technique can be seen in the signal acquired from linoleic acid at multiple echo times using both standard and narrow bandwidth PRESS sequences in figure 2.5. It is clear that the narrow bandwidth PRESS sequence results in higher signal at each time point as a result of rewinding J-coupling evolution of the $1.3\ ppm$ methylene protons and the $0.9\ ppm$ methyl protons.

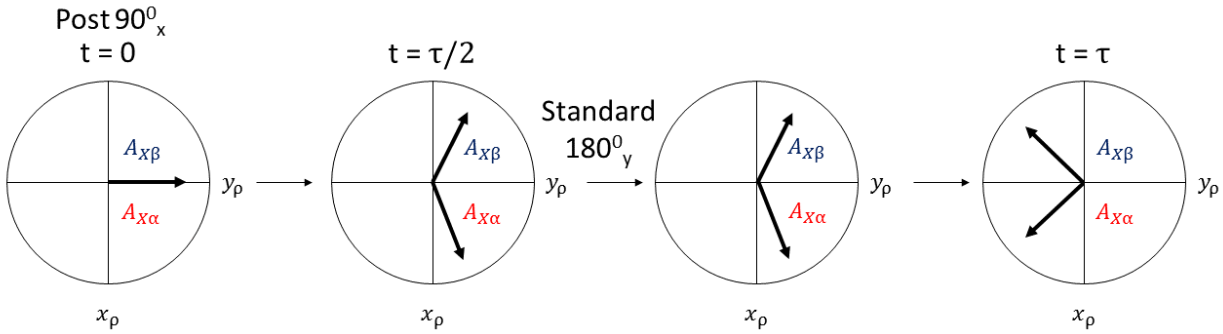

Figure 2.4

a. Evolution of an AX spin system under a 90◦ and standard 180◦ pulse sequence. J-coupling evolution is not rewound after application of a standard bandwidth 180◦ pulse.

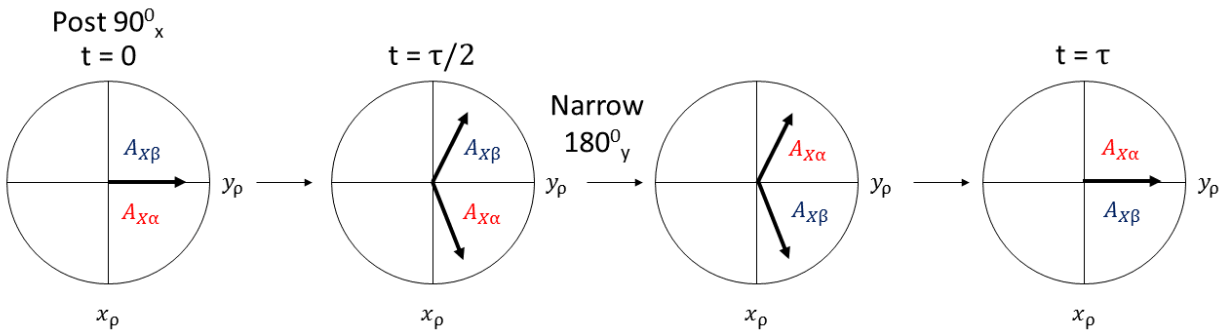

b. Evolution of an AX spin system under a$90°$ and a narrow $180°$◦ pulse sequence. J-coupling evolution is rewound by application of a narrow bandwidth $180°$◦ pulse.

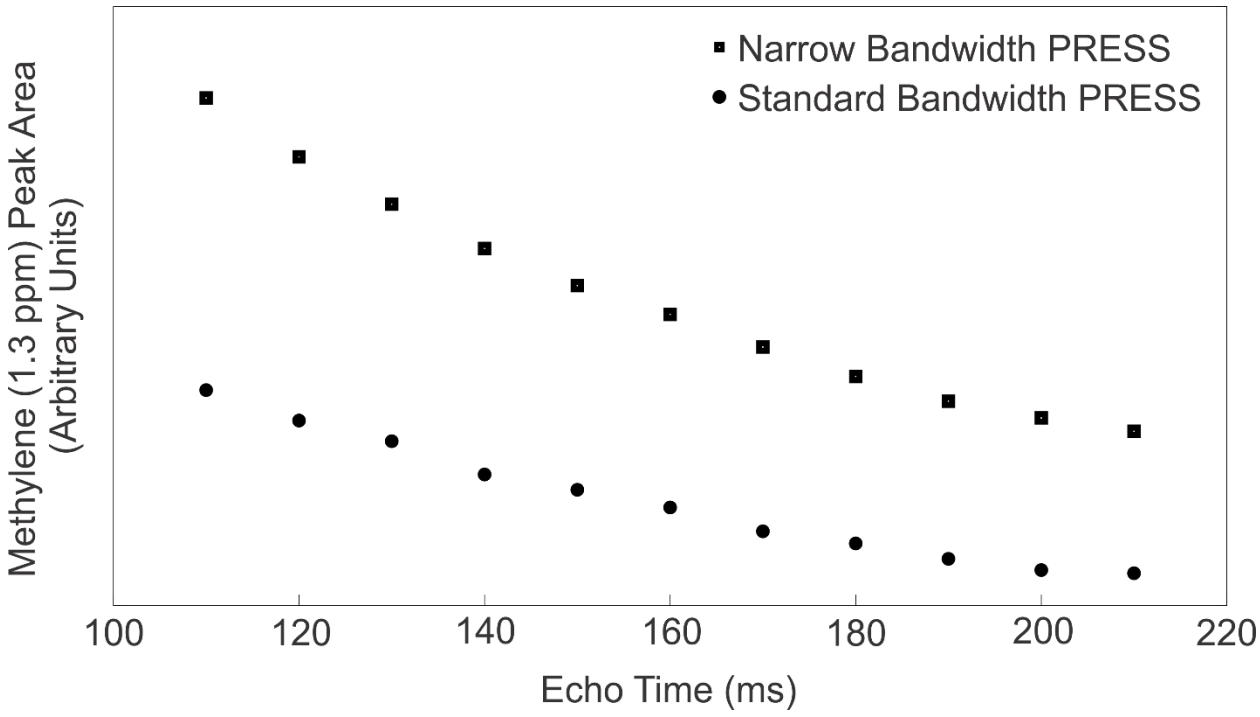

Figure 2.5

a. Comparison of signal acquired with the narrow and standard bandwidth PRESS sequences from the $1.3\ ppm$ methylene protons of linoleic acid. Clear enhancement in signal is visible when employing the narrow bandwidth PRESS sequence at each TE.

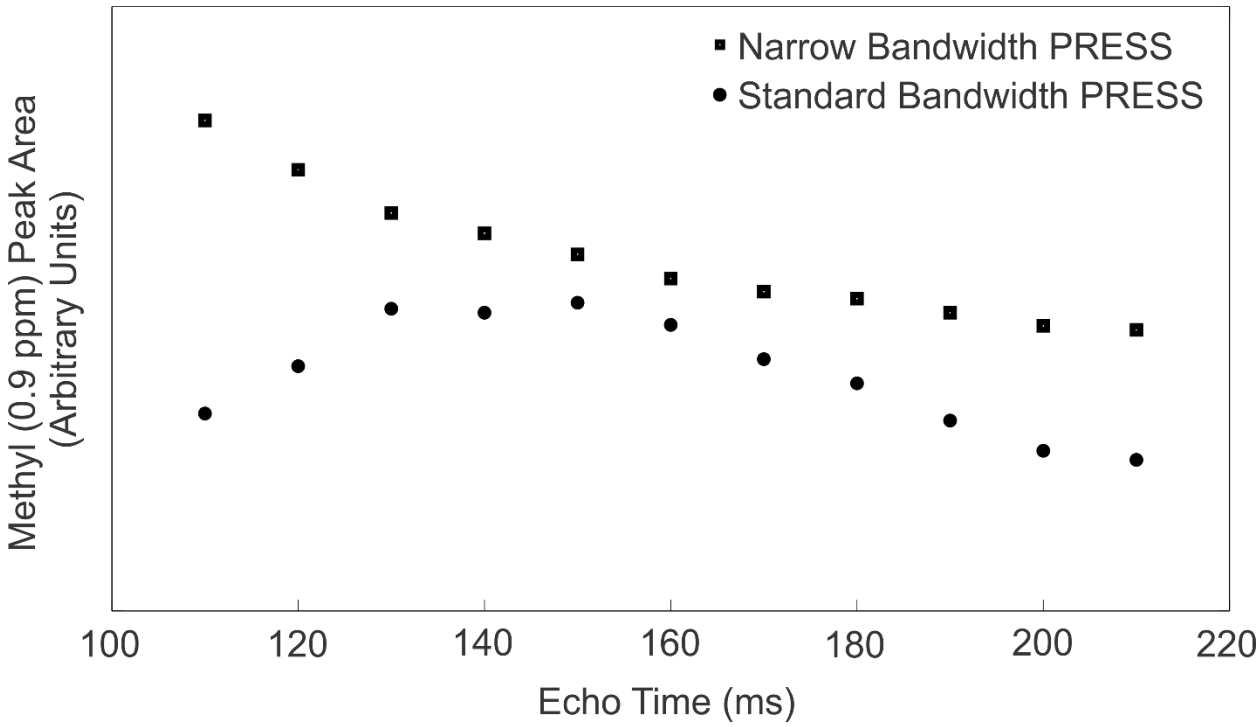

b. Comparison of signal acquired with the narrow and standard bandwidth PRESS sequences from $1.3\ ppm$ methyl protons in linoleic acid.

The effect of the narrow bandwidth PRESS sequence was tested on water phantoms, the protons of which have no J-coupling interactions, to determine if some other mechanism other than J-coupling is responsible for the change seen in figure 2.5. No significant difference between the data collected using the standard bandwidth and the narrow bandwidth PRESS sequence was found leading to the conclusion that the cause of the increased signal intensity seen in figure 2.5 is due to rewinding J-coupling evolution.

2.6 – Phantom Experiments

2.6.2 – Experimental Parameters

All imaging experiments were performed with a $3\,T$wholebody Philips MRI scanner. Phantom experiments were conducted employing a transmit/receive Philips head coil. Phantoms consisted of corn oil and a variety of commercially available fatty acids. Three main spectroscopy techniques were employed in the experiments performed in this thesis, namely, a STEAM sequence, a PRESS sequence, and a PRESS sequence which used narrow bandwidth refocussing pulses. Additionally, a scout image protocol, which employed a spin echo sequence, was employed initially in all experiments to acquire an image for the purposes of spatially localizing the spectroscopy voxel. Details of the pulse sequences are provided below.

2.6.2.1 – STEAM Pulse Sequence Parameters

Signal from phantoms was acquired from 32 averages from a $5\ \mathrm{x}\ 5\ \mathrm{x}\ 5\,mm^3$ voxel placed in the centre of the phantom. The repetition time was set to$3\,s$, the mixing time was set to $20\,ms$ and echo times were used ranging from $20\,ms$ to $200\,ms$ in steps of $10\,ms$. The STEAM sequence used RF pulses with a duration of $4.8\,ms$ and a bandwidth of $\sim 2900\,Hz$. The frequency of the RF pulses was set to the $1.3\,ppm$ methylene peak resonance frequency. Six outer volume suppression pulses with bandwidths of $\sim 3900\,Hz$ were employed in conjunction with gradients to suppress unwanted signal originating from$30\,mm$ slices outside the voxel of interest. Outer volume suppression pulses are used in the standard bandwidth PRESS method to be consistent with the methodology used in the narrow bandwidth method.

2.6.2.2 – Standard Bandwidth PRESS Pulse Sequence Parameters

Voxel size, position, acquired averages, repetition time, employed echo times and outer volume suppression techniques are identical to those used in STEAM. The standard PRESS sequence used sinc-gauss RF pulses. Excitation pulses had a duration of $3\ ms$ and a bandwidth of $\sim 3000\ Hz$. The refocussing pulses had a duration of $3.2\ ms$ and a bandwidth of $\sim 565\ Hz$. The frequency of the RF pulses was set to the $1.3\ ppm$ methylene peak resonance.

2.6.2.3 – Narrow Bandwidth PRESS Pulse Sequence Parameters

All parameters mentioned in section 2.5.2b remain the same with the exception of the duration and bandwidth of the sinc-gauss refocussing pulses which were set at $36\ ms$and $\sim 50\ Hz$, respectively. It should be noted that the bandwidth of $50\ Hz$ is less than the smallest chemical shift between the $1.3\ ppm$ methylene protons and the $0.9\ ppm$ methyl and $2.1\ ppm$ allylic protons. The bandwidth of $50\ Hz$ is not smaller than the chemical shift difference between the $1.3\ ppm$ methylene protons and the $1.6\ ppm$ methylene protons. However, J-coupling evolution due to the interaction between the $1.3\ ppm$ and the $1.6\ ppm$ protons cannot be rewound using the narrow bandwidth method due to the strong coupling behaviour of the interaction. Within the dimensions of the voxel generated by a narrow bandwidth PRESS method only the $1.3\ ppm$ methylene protons will generate signal. Signal from the $0.9\ ppm$ methyl protons will originate outside the voxel of interest as pictured in the right side of figure 2.3. The unwanted $0.9\ ppm$ methyl signal will be from an un-shimmed region, and may overlap

with and contaminate the $1.3\ ppm$ spectral peak. The outer volume suppression pulses are used to dephase the unwanted signal from the $0.9\ ppm$ methyl protons.

2.6.3 – Experimental Analysis

The spectra acquired in all experiments share the same details of spectral analysis. After acquisition, the FID is first filtered using a $2\ Hz$ Gaussian filter and then Fourier transformed to produce a spectrum. The resulting spectrum is then manually phased, the baseline is adjusted, and the peak resonances are manually assigned their chemical shift values. The area of the $1.3\ ppm$ methylene peak resonance is integrated in the window of $1.10 - 1.50\ ppm$ for consistency as indicated by the dashed lines in figure 2.6. This window excludes signal from the neighbouring $1.6\ ppm$ methylene protons and the $0.9\ ppm$ methyl protons. The resulting peak areas are then plotted as a function of echo time and fit to a monoexponentially decaying function using a non-linear least squares fitting algorithm in MATLAB in order to estimate M_0 and T_2. It should be noted that only echo times of $100, 120, 140, 160, 180$ and $200\ ms$ are used to fit the data from every acquired scan, regardless of pulse sequence, for consistency since the minimum attainable TE with the narrow bandwidth PRESS sequence is $100\ ms$. The coefficient of determination (R^2) is used to assess the accuracy of the monoexponential fits and is calculated using linear regression in Microsoft Excel according to Equation 2.7. The computational methods used by excel first linearize the data and fits the result to a straight line. Further experimental details and results follow in chapter 3.

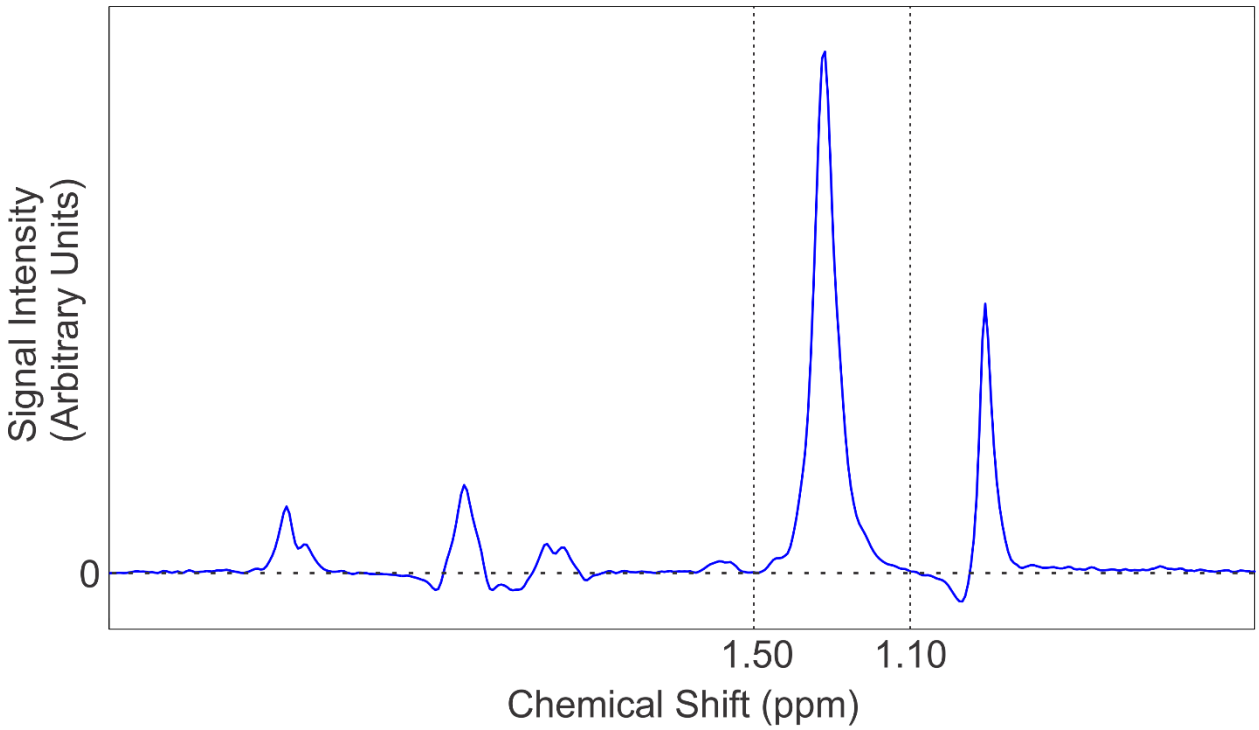

Figure 2.6– MRS spectrum of linoleic acid indicates the window of integration used for the $1.3\ ppm$ methylene peak during analysis. Acquired at $3\ T$ with a standard PRESS sequence at a TE of $100\ ms$.

2.7 – *In-Vivo* Experiments

2.7.1 – Experimental Parameters

Six volunteers (2 female, 4 male), ages 25 – 40, were scanned using the standard and narrow bandwidth PRESS sequences. *In-vivo* experiments were performed using the built in body coil of the $3\ T$ scanner for transmission and one element of a phased array surface coil for reception (Philips Flex L phased array coil). One element of the surface coil was placed approximately $10\ cm$ below the left knee cap of each volunteer and secured with Velcro straps. Axial and sagittal scout images were acquired using a T_1-weighted fast spin echo

sequence with the following parameters: $250\text{x}\ 250\ \text{x}\ 100\ mm^3$ field of view, $7.5\ ms\ TR$, $2.4\ ms\ TE$, 15° flip angle, and $10\ mm$ slice thickness. *In-vivo* signal was acquired from an $8\ \text{x}\ 8\ \text{x}\ 8mm^3$ voxel located in the centre of tibial bone marrow approximately $10\ cm$ below the knee cap of the volunteer as pictured in figure 2.7. The parameters of the PRESS sequences used were identical to those of the phantom experiments with the exception of the voxel size and the number of averages. Instead of 32 averages, only 16 averages were acquired to reduce scan time. To assess the reproducibility of the narrow bandwidth PRESS technique spectra from one volunteer were acquired at each echo time of $100, 120, 140, 160, 180$ and $200\ ms$ five times in one scan session.

Figure 2.7 – Sagittal image showing voxel placement in the volunteers. The voxel is placed approximately 10 cm below the left knee cap in the centre of the bone marrow. Parameters are: 250 x 250 x 100 mm^3 field of view, 7.5 ms TR, 2.4 ms TE, $15°$ flip angle, and 10 mm slice thickness.

2.7.2 – Experimental Analysis

Analysis of the *in-vivo* data follows the same methods as outlined for the phantom experiments. In addition, a paired t-test was used to statistically evaluate the changes in M_0 and T_2 between the standard and narrow bandwidth PRESS sequences over all volunteers. As well, coefficients of variation (CV) were calculated for the integrated 1.3 ppm methylene peak areas, M_0 and T_2 values of the volunteer who underwent multiple scans to assess reproducibility.

2.7.3 – Paired t-test

A paired t-test can be used to statistically compare the differences between two of the same (paired) measurements acquired by different methods. A p-value of < 0.05 is taken to represent a statistically significant difference between the two methods. To determine the p-value, first the value t is calculated using(31)

$$t = \left(\overline{X} - \overline{Y}\right)\sqrt{\frac{n(n-1)}{\sum_{i=1}^{n}(\widehat{X_i} - \widehat{Y_i})^2}}, \tag{2.5}$$

where $\widehat{X_i} = \left(X_i - \overline{X}\right)$ and $\widehat{Y_i} = \left(Y_i - \overline{Y}\right)$. The value of t is then compared to a Student's t-test distribution to determine the p-value. A Student's t-distribution is a continuous probability distribution used to estimate the mean of a normally distributed population using a small sample size and an unknown standard deviation. In contrast a normal distribution describes a complete population. The t-distribution is more prone to error due to its limited sample size and heavier tails. Student's t-distributions approach normal distributions as sample size increases.

2.7.4 – Coefficient of Variation

A coefficient of variation is defined mathematically as

$$CV = \frac{\sigma}{\mu}, \tag{2.6}$$

where, σ is the standard deviation of a set of numbers and μ is the mean of those numbers. A coefficient of variation is used to measure the dispersion of a variable.

2.7.5 – Coefficient of Determination

For a linear regression model with one independent variable the coefficient of determination is given by

$$R^2 = \left[\frac{\left(\frac{1}{N}\right)\sum_{i=1}^{N}[(x_i - x)(y_i - y)]}{(\sigma_x \sigma_y)}\right]^2, \tag{2.7}$$

where N is the number of observations, x_i is the dependent variable of observation i, $\bar{x}$ is the mean of the all observations x, y_i is the independent variable of observation i, $\bar{y}$ is the mean of the all observations y, σ_x is the standard deviation of observations x and σ_y is the standard deviation of observations .

2.8 – Fatty Acid Composition

Of relevance to the thesis is the fatty acid composition of tibial bone marrow and corn oil. The primary components (with concentrations of at least $1\ \%$) of tibial bone marrow are linoleic acid ($19\ \%$), oleic acid ($45\ \%$), palmitic acid ($22\ \%$), stearic acid ($5\ \%$) and myristic acid ($1\ \%$)(32). The remaining $8\ \%$ is composed of fatty acids found in concentrations of less than

1 %. Figure 2.8 illustrates the molecular structures of stearic and myristic acid, which are saturated fatty acids. The molecular structure of palmitic acid (another saturated fatty acid) is given in figure 2.1. The mean number of $1.3\ ppm$ methylene protons contained in saturated fatty acids in tibial bone marrow is therefore

$$(0.23/0.29)24 + (0.05/0.29)28 + (0.01/0.29)20 = \sim 25$$

Corn oil is composed of $50.4 - 57.5\ \%$ linoleic acid, $28.0 - 34.6\ \%$ oleic acid and $12.5 - 16.1\ \%$ saturated fatty acids(33). The main saturated fatty acid component is palmitic acid, followed by stearic and myristic acid(34).

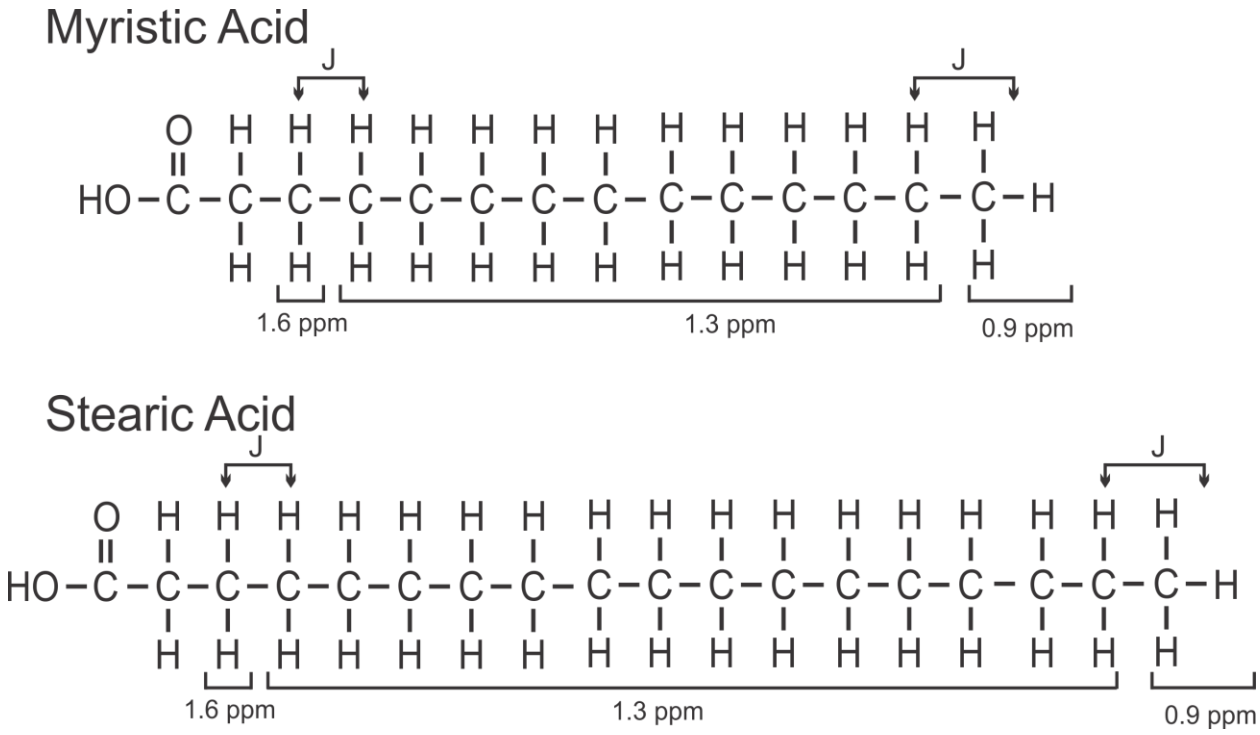

Figure 2.8 – Molecular structures of myristic and stearic acid.

2.9 – References

1. Yahya A, Fallone BG. T_2 determination of the J-coupled methyl protons of lipids: in vivo ilustration with tibial bone marrow at 3 T *J Magn Reson Imaging* 2010; **31**: 1514-1521.
2. Leray C. Lipids Nutrition and Health: CRC Press; 2014.
3. Ren J, Dimitrov I, Sherry A, Malloy C. Composition of Adipose Tissue and Marrow Fat in Humans by ^{1}H NMR at 7 Tesla. *Journal of Lipid Research* 2008; **49**.
4. Chernov MF, Hayashi M, Izawa M, Ono Y, Hori T. Proton magnetic resonance spectroscopy (MRS) of metastatic brain tumors: variations of metabolic profile. *Int J Clin Oncol* 2006; **11**: 375-384.
5. Kumar M, Jagannathan NR, Seenu V, Dwivedi SN, Julka PK, Rath GK. Monitoring the therapeutic response of locally advanced breast cancer patients: sequential in vivo proton MR spectroscopy study. *J Magn Reson Imaging* 2006; **24**: 325-332.
6. Oriol A, Valverde D, Capellades J, Cabañas ME, Ribera JM, Arús C. In vivo quantification of response to treatment in patients with multiple myeloma by ^{1}H magnetic resonance spectroscopy of bone marrow. *Magn Reson Mater Phy* 2007; **20**: 93-101.
7. Qi J, Fong Y, Saltz L, D'Angelica MI, Kemeny NE, Gonen M, Shia J, Shukla-Dave A, Jarnagin WM, Do RKG, Schwartz LH, Koutcher JA, Zakian KL. Serial measurement of hepatic lipids during chemotherapy in patients with colorectal cancer: a ^{1}H MRS study. *NMR Biomed* 2013; **26**: 204-212.
8. Chabanova E, Bille DS, Thisted E, Holm JC, Thomsen HS. ^{1}H MRS assessment of hepatic steatosis in overweight children and adolescents: comparison between 3T and open 1T MR-systems. *Abdom Imaging* 2013; **38**: 315-319.
9. Hayashi N, Miyati T, Minami T, Takeshita Y, Ryu Y, Matsuda T, Ohno N, Hamaguchi T, Kato K, Takamura T, Matsui O. Quantitative analysis of hepatic fat fraction by single-breath-holding MR spectrscopy with T_2 correction: phantom and clinical study with histologic assessment. *Radiol Phys and Technol* 2013; **6**: 219-225.
10. Griffith JF, Yeung DKW, Antonio GE, Lee FKH, Hong AWL, Wong SYS, Lau EMC, Leung PC. Vertebral bone mineral density, marrow perfusion, and fat content in healthy men and

men with osteoporosis: dynamic contrast-enhanced MR imaging and MR spectroscopy. *Radiology* 2005; **236**: 945-951.

11. Li X, Kuo D, Schafer AL, Porzig A, Link TM, Black D, Schwartz AV. Quantification of vertebral bone marrow fat content using 3 Tesla MR spectroscopy: reproducibility, vertebral variation, and applications in osteoporosis. *J Magn Reson Imaging* 2011; **33**: 974-979.
12. Borra R, Lautamäki R, Parkkola R, Komu M, Sijens PE, Hällsten K, Bergman J, Iozzo P, Nuutila P. Inverse association between liver fat content and hepatic glucose uptake in patients with type 2 diabetes mellitus. *Metabolism* 2008; **57**: 1445-1451.
13. Kotronen A, Juurinen L, Tiikkainen M, Vehkavaara S, Yki-Järvinen H. Increased liver fat, imparied insulin clearance, and hepatic adipose tissue insulin resistance in type 2 diabetes. *Gastroenterology* 2008; **135**: 122-130.
14. Perseghin G, Scifo P, De Cobelli F, Pagliato E, Battezzati A, Arcelloni C, Vanzulli A, Testolin G, Pozza G, Del Maschio A, Luzi L. Intramyocellular triglyceride content is a determinant of in vivo insulin resistance in humans. *Diabetes* 1999; **48**: 1600-1606.
15. Hamilton G, Middleton MS, Bydder M, Yokoo T, Schwimmer JB, Kono Y, Patton HM, Lavine JE, Sirlin CB. Effect of PRESS and STEAM sequences on magnetic resonance spectroscopic liver fat quantification. *J Magn Reson Imaging* 2009; **30**: 145-152.
16. Oostendorp M, Engelke UFH, Willemsen MAAP, Wevers RA. Diagnosing inborn errors of lipid metabolism with proton nuclear magnetic resonance spectroscopy. *Clin Chem* 2006; **52**: 1395-1405.
17. Stokes AM, Feng Y, Mitropoulos T, Warren WS. Enhanced refocusing of fat signals using optimized multipulse echo sequences. *Magn Reson Med* 2013; **69**: 1044-1055.
18. Henkelman RM, Hardy PA, Bishop JE, Poon CS, Plewes DB. Why fat is bright in RARE and fast spin-echo imaging. *J Magn Reson Imaging* 1992; **2**: 533-540.
19. Melki P, Mulkern R, Lawrence P, Jolesz F. Comparing the FAISE Method with Conventional Dual-Echo Sequences. *Journal of Magnetic Resonance Imaging* 1991; **1**: 319-326.

20. Constable R, Anderson A, Zhong J, Gore J. Factors Influencing Contrast In Fast Spin-Echo MR Imaging. *Magnetic Resonance Imaging* 1992; **10**: 497-511.
21. Hinks R, Martin D. Bright Fat, Fast Spin Echo, and CPMG. *Proceedings of the Society of Magnetic Resonance in Medicine 11th Annual Meeting* 1992: 4503.
22. Peled S, Williamson D, Mulkern R. Signal Intensity Studies of Strongly-Coupled Spin Systems during CPMG/RARE Imaging Sequences. *Proceedings of the Society of Magnetic Resonance Third Scientific Meeting* 1995: 655.
23. Rutt B, Wright G. Lipid Signal Enhancement in CPMG MRI: Effect of Field Strength. *Proceedings of the Society of Magnetic Resonance in Medicine 11th Annual Meeting* 1992: 4504.
24. Williamson D, Mulkern R, Jakab P, Jolesz F. Coherence Transfer by Isotropic Mixing in Carr-Purcell-Meiboom-Gill Imaging: Implications for the Bright Fat Phenomenon in Fast Spin-Echo Imaging. *Magnetic Resonance in Medicine* 1996; **35**: 506-513.
25. Wright G, Macovski A. Lipid Signal Enhancement in Spin-Echo Trains. *Proceedings of the Society of Magnetic Resonance in Medicine 11th Annual Meeting* 1992: 437.
26. Allerhand A. Analysis of Carr-Purcell Spin-Echo NMR Experiments on Multiple-Spin Systems. *The Journal of Chemical Physics* 1966; **44**: 1-9.
27. Gajdošík M, Chmelík M, Just-Kukurová I, Bogner W, Valkovič L, Trattnig S, Krššák M. In vivo relaxation behavior of liver compounds at 7 Tesla, measured by single-voxel proton MR spectroscopy. *J Magn Reson Imaging* 2014; **40**: 1365-1374.
28. Yahya A, Mädler B, Fallone BG. Exploiting the chemical shift displacement effect in the detection of glutamate and glutamine (Glx) with PRESS. *J Magn Reson Imaging* 2008; **191**: 120-127.
29. Yablonskiy D, Neil J, Raichle M, Ackerman J. Homonuclear J Coupling Effects in Volume Localized NMR Spectroscopy: Pitfalls and Solutions. *Magnetic Resonance in Medicine* 1998; **39**: 169-178.
30. de Graaf R. *In Vivo* NMR Spectroscopy: John Wiley & Sons Ltd.; 2007.
31. Goulden C. Methods of Statistical Analysis. New York: Wiley; 1956.

32. Griffith J, Yeung D, Ahuja A, Choy C, Mei W, Lam S, Lam T, Chen Z, Leung P. A Study of Bone Marrow and Subcutaneous Fatty Acid Composition in Subjects of Varying Bone Mineral Density. *Bone* 2009; **44**.

33. Yahya A, Tessier A, Fallone B. Effect of J-Coupling on Lipid Composition Determination With Localized Proton Magnetic Resonance Spectroscopy at 9.4 T. *Journal of Magnetic Resonance Imaging* 2011; **34**: 1388-1396.

34. Baur F, Brown J. The Fatty Acids of Corn Oil. *Journal of the American Chemical Society* 1945; **67**: 1899-1900.

Chapter 3 - Effect of J-Coupling on 1.3 ppm Lipid Methylene Signal Acquired with Localized Proton Magnetic Resonance Spectroscopy at 3 T*

3.1 – Introduction

Magnetic resonance spectroscopy measurements of lipids based on quantification of the 1.3 ppm signal from the -$(CH_2)_n$- methylene chain protons have been shown to be relevant in the study of a number of diseases and disorders (1-12). Often, the measures are those acquired with short echo time single voxel localization sequences (1,3,6-9,11) such as , Point RESolved Spectroscopy (PRESS)(13), or , Stimulated Echo Acquisition Mode (STEAM)(14). Some studies attempted to provide an absolute quantification by correcting for the transverse relaxation of the methylene protons by acquiring signal at more than one TE and fitting the response to a monoexponentially decaying function of the form $M_o\exp(-TE/T_2)$, where M_o is the extrapolated signal for $TE = 0$ ms(2,12). The T_2 of the 1.3 ppm protons has also demonstrated relevance in the study of colon cancer where T_2 times have been used to differentiate between colon tumours with high and low metastatic potential (15). Lipid methylene protons *in-vivo* and in phantoms representative of *in-vivo* lipid compositions have been shown to exhibit monoexponential decay with increasing TE(16), which provides the impression that effects of J-coupling on quantification of the 1.3 ppm lipid signal and its

*A version of this chapter has been accepted for publication.
Dylan Breitkreutz, B. Gino Fallone, Atiyah Yahya, "Effect of J coupling on 1.3-ppm lipid methylene signal acquired with localised proton MRS at 3 T", *NMR in Biomedicine.*

estimated T_2 are minimal (17,18). However, some of the 1.3 ppm lipid methylene protons do exhibit J-coupling interactions, namely, with the ≈ 0.90 ppm methyl, the ≈ 1.6 ppm methylene and the ≈ 2.1 ppm allylic proton groups (19). Evidence of J-coupling effects on fat signal has been observed in MRI where signal from fat is enhanced in FSE or CPMG images due to reduction of J-coupling modulation by the train of refocussing pulses (20-27). The response has been attributed to be dependent on interpulse timings in multipulse echo MRI sequences (19-21,28,29). In addition, in single voxel spectroscopy experiments PRESS and STEAM yield differences in measures of the 1.3 ppm methylene protons and their T_2 values (16). Recently, work has been done at 7 T to improve quantification of J-coupled lipid protons by fitting acquired data at multiple TE values to a function of the form $M_o\exp(-TE/T_2)[\cos(\pi JTE)+b]$, where b is a constant and J is a parameter introduced to fit oscillatory patterns of J-coupling evolution (30). The fitting, however, did not significantly alter the determined values of M_o and T_2 for the 1.3 ppm protons of corn oil; furthermore, in liver *in vivo* the fitting procedure did not yield a non-zero value for J due to the monoexponential decay of the methylene resonance signal with increasing TE(30). To our knowledge, no attempt other than that of Ref. (30) has been performed to estimate the errors that arise in determined M_o and T_2values of 1.3 ppm lipid protons due to J-coupling evolution.

In this work, we investigate the response of the 1.3 ppm protons to PRESS and STEAM in fatty acids of different chain lengths, namely, hexanoic, heptanoic, octanoic, linoleic and oleic acid. In addition, we apply a PRESS-based methodology, previously applied to rewind J-coupling evolution of other lipid proton groups (17,31), to rewind the J-coupling evolution of the 1.3 ppm lipid protons in the mentioned fatty acid phantoms, in corn oil, and in tibial bone marrow

in vivo. The technique enables more representative values of M_o and T_2 to be obtained and provides a quantitative estimate of how the values are affected by the presence of J-coupling interactions.

3.2 – Theory

At 3 T, the J-coupling interaction of 1.3 ppm lipid protons with neighbouring 0.9 ppm methyl protons can be considered to be on the threshold of weak coupling with a coupling constant (6.9 Hz) to chemical shift difference (51 Hz) ratio, J/δ, of ≈ 0.13(17). 1.3 ppm protons are also strongly-coupled to neighbouring 1.6 ppm protons with a J/δ of ≈ 0.18(19). In addition, in the presence of double bonds, 1.3 ppm protons are weakly-coupled to neighbouring 2.1 ppm allylic protons with a J/δ of ≈ 0.07(19), where δ is about 102 Hz. A PRESS sequence with refocusing pulses of bandwidth less than the chemical shift difference between weakly-coupled spins will rewind the J-coupling evolution of the target protons in the voxel of interest (32,33). Therefore, the methodology can be employed to rewind the weak coupling evolutions of the 1.3 ppm lipid protons (associated with interactions with the 0.9 and 2.1 ppm protons) by employing refocussing pulses of 50 Hz. The evolution due to strong-coupling interactions with the 1.6 ppm protons, however, will not be rewound. Figure 3.1 shows the molecular structures of hexanoic, heptanoic, octanoic, linoleic and oleic acid labelled with appropriate chemical shifts and coupling interactions. The percentage of 1.3 ppm protons involved in J-coupling interactions with neighbouring protons are 100 %, 67 %, 50 %, 57 % and 40 % for hexanoic, heptanoic, octanoic, linoleic and oleic acid, respectively.

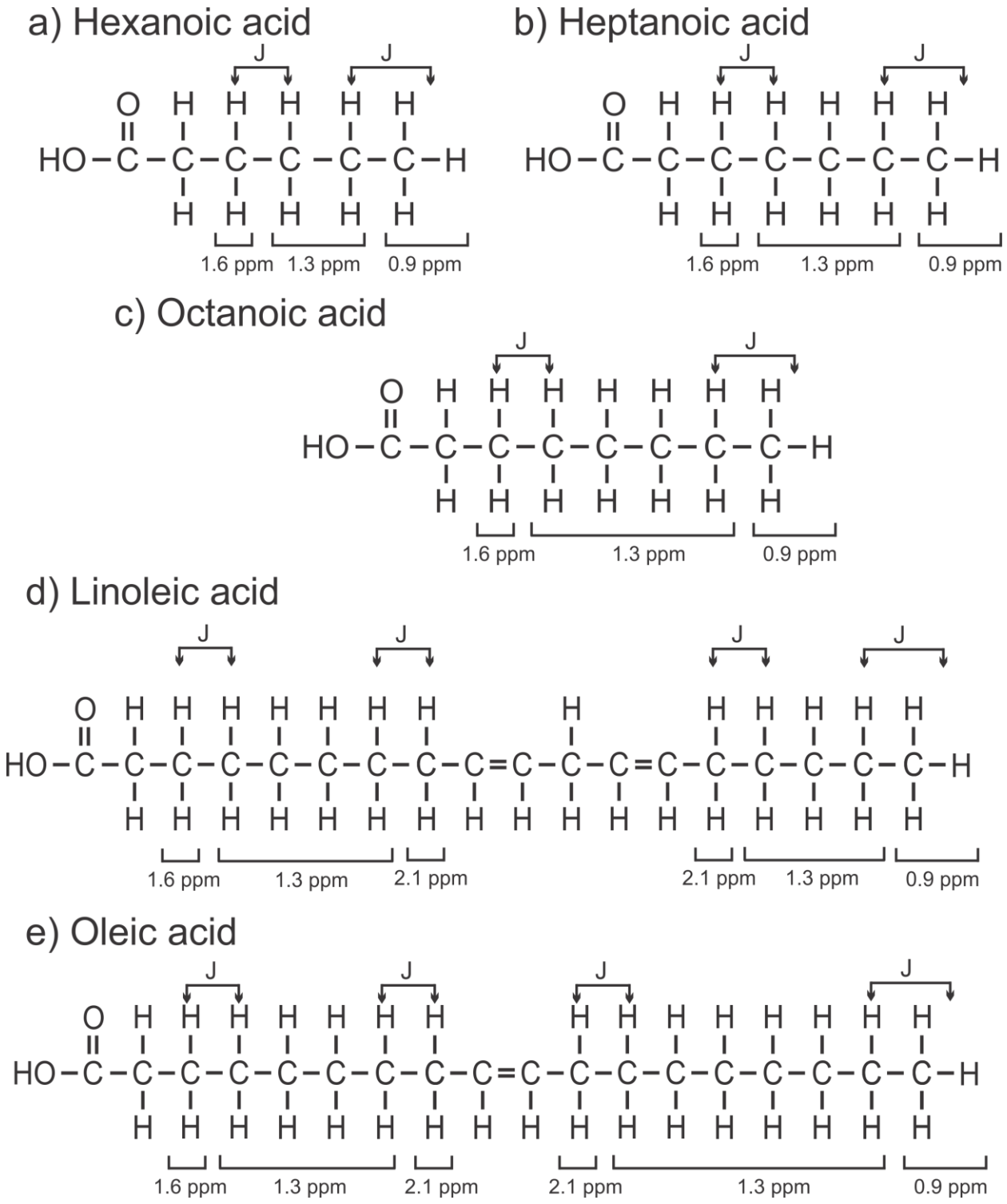

Figure 3.1 – Molecular structures of hexanoic, heptanoic, octanoic, linoleic and oleic acid. J-coupling interactions of 1.3 ppm protons with neighbouring proton groups are indicated by J.

3.3 - Materials and Methods

Experiments were performed using a whole body 3 T scanner (Intera, Philips Healthcare, Best, Netherlands). A transmit/receive head coil (Philips Healthcare) was used for all phantom experiments. Tibial bone marrow of six healthy volunteers (2 female, 4 male) was scanned (age range 25-40 years) after each volunteer signed informed consent. For *in-vivo* scans, the built in body coil of the scanner was employed for transmission while one element of a phased array surface coil (Flex-L, Philips Healthcare) was used for reception. The surface coil was centred approximately 10 cm below the left kneecap of volunteers and was secured using velcro straps. For both phantom and *in-vivo* experiments, two versions of a PRESS pulse sequence were used to acquire spectra. The first PRESS sequence employed sinc-gauss refocussing pulses with a duration of 3.2 ms and a bandwidth of ≈ 565 Hz (we refer to this as standard bandwidth PRESS). The second PRESS sequence used the same sequence but the refocussing pulse duration was increased to 36 ms to yield a bandwidth of ≈ 50 Hz (we refer to this as narrow bandwidth PRESS). A STEAM sequence which employed 4.8 ms long pulses with bandwidths of ≈ 2900 Hz was also used for phantom experiments. The frequency of the radiofrequency pulses was set to the 1.3 ppm methylene peak resonance. For phantoms, 32 averages were acquired for each spectrum from a 5 x 5 x 5 mm^3 voxel located in the centre of the phantom. For *in-vivo* experiments, 16 averages were acquired from an 8 x 8 x 8 mm^3 voxel which was positioned in the left tibia as indicated in Fig. 3.6(c). Six 30 mm outer volume suppression slices were positioned at the edges of the voxel to suppress signal from outside the region of interest. Shimming was performed automatically by the scanner and the full width half maximum (FWHM) of the 1.3 ppm methylene peak acquired with a TE of 30 ms was $\approx$

$9\ \mathrm{Hz}$ and $\approx 15\ \mathrm{Hz}$ for phantom and *in-vivo* spectra, respectively. To illustrate the effect of J-coupling interactions on signal evolution of the $1.3\ \mathrm{ppm}$ methylene protons, phantoms of hexanoic acid, heptanoic acid, octanoic acid, linoleic acid, oleic acid and corn oil were scanned using the standard bandwidth PRESS sequence and the STEAM sequence with a TR of $3\ \mathrm{s}$. For the standard bandwidth PRESS sequence, TE_1 was held constant at $15\ \mathrm{ms}$ and TE_2 was varied to achieve total TE values ranging from $30\ \mathrm{ms}$ to $200\ \mathrm{ms}$ in steps of $10\ \mathrm{ms}$. For the STEAM sequence, the dependence on TE was explored by fixing TM at $20\ \mathrm{ms}$ and varying TE from 20 to $200\ \mathrm{ms}$ in steps of $10\ \mathrm{ms}$. To demonstrate the consequences of J-coupling evolution on determined $\mathrm{M_o}$ and $\mathrm{T_2}$ values for the $1.3\ \mathrm{ppm}$ protons, all phantoms and volunteers were scanned with the standard bandwidth and the narrow bandwidth PRESS sequences. TE_1 of the standard and narrow bandwidth PRESS sequences were set to $15\ \mathrm{ms}$ and $48\ \mathrm{ms}$, respectively. TE_2 was increased for both PRESS sequences to achieve total TE values of 100, 120, 140, 160, 180 and $200\ \mathrm{ms}$. A TR of $3\ \mathrm{s}$ was used for all scans. Philips spectral processing software was employed to process and analyze all acquired spectra. All spectra were filtered, Fourier transformed, and phase corrected before the $1.3\ \mathrm{ppm}$ methylene peak area was calculated by integration between $1.10\mathrm{ppm}$ and $1.50\ \mathrm{ppm}$. For $\mathrm{M_o}$ and $\mathrm{T_2}$ estimation, peak areas were fit according to the function $\mathrm{M} = \mathrm{M_o}\exp(\text{-}\mathrm{TE}/\mathrm{T_2})$, since $\mathrm{TR} >> \mathrm{TE}$(34,35), with a least squares analysis in MATLAB (Mathworks, Natick, MA), where $\mathrm{M_o}$ is the extrapolated area when $\mathrm{TE} = 0\ \mathrm{ms}$.

To verify data reproducibilityin phantom, five sets of standard bandwidth and narrow bandwidth data were acquired from each of heptanoic, octanoic, linoleic and oleic acid. The coefficient of variation (standard deviation/mean), CV, of the $\mathrm{M_o}$ and $\mathrm{T_2}$ values obtained with

each data set was computed. A reproducibility test was also conducted *in vivo.* Five narrow bandwidth PRESS data sets were acquired from one of the volunteers in the same scan session. The CV of the methylene peak areas obtained with each TE was calculated. In addition, the coefficient of variation of the M_o and T_2 values obtained with each data set was computed. To confirm statistical significance of any differences in M_o and T_2 obtained with the two different PRESS sequences *in vivo* a two-tailed paired t-test was employed with MATLAB. Any stated coefficients of determination (R^2) values were obtained from linearization of data sets and fits to straight lines in MATLAB.

3.4 – Results

Figure 3.2 presents plots of the normalized 1.3 ppm methylene peak areas obtained as a function of standard PRESS and STEAM TE for hexanoic, heptanoic, octanoic, linoleic and oleic acid. J-modulation is clearly visible in the hexanoic and heptanoic acid responses. As the methylene chain length increases, and the percentage of protons involved in J-coupling interactions decreases, signal modulations become less evident and the signal decays more monoexponentially. In addition, as the methylene chain length increases, there is less of a difference between the responses to PRESS and to STEAM. The effects of J-coupling are also more apparent in the spectra acquired from the shorter chain fatty acids. Figure 3.3 displays some the 1.3 ppm resonances acquired from oleic acid and heptanoic acid for a few TE values; peak splitting from J-coupling interactions are visible in the heptanoic acid spectra but not in those of oleic acid.

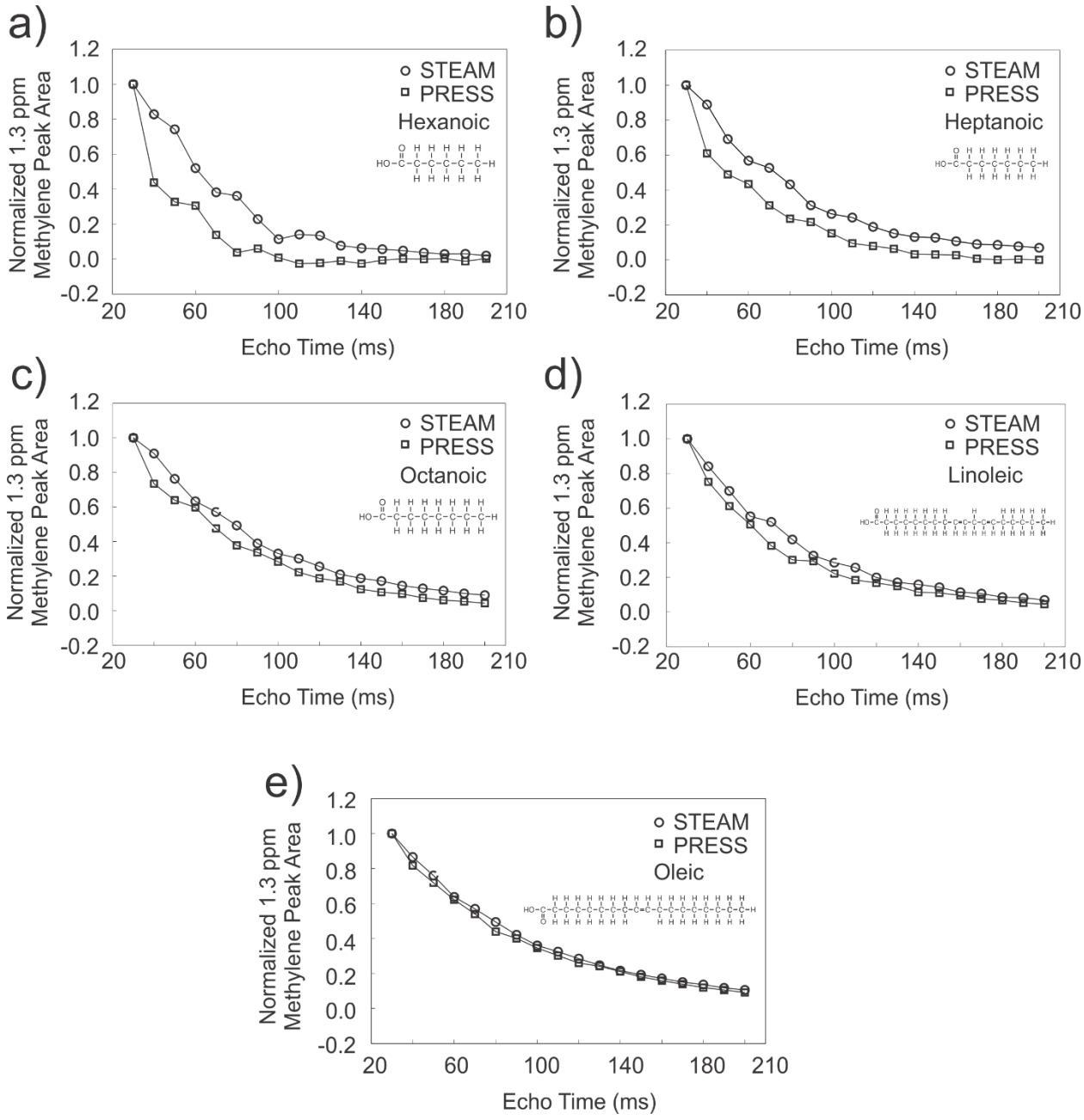

Figure 3.2 – Signal evolution of the 1.3 ppm methylene protons as a function of PRESS and STEAM TE for hexanoic, heptanoic, octanoic, linoleic and oleic acid. Peak areas for PRESS are normalized to the corresponding maximum area obtained with PRESS (acquired with the shortest TE) for each fatty acid. Similarly, peak areas obtained with STEAM are normalized to the maximum STEAM area. For STEAM, TM = 20 ms. The molecular structure of each fatty acid is displayed in each plot.

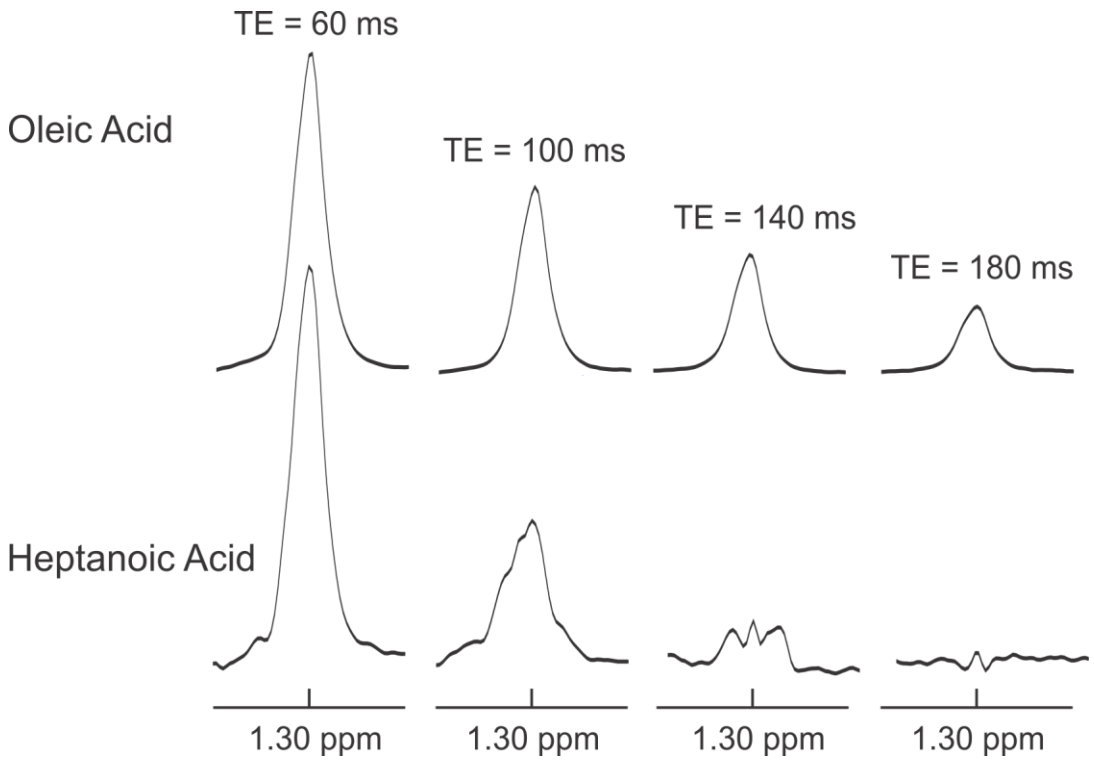

Figure 3.3 –Spectra of the 1.3 ppm methylene resonance for oleic and heptanoic acid for TE values of 60, 100, 140 and 180 ms.

Figure 3.4 shows the response of the 1.3 ppm protons as a function of TE for the five fatty acids measured with both the standard and the narrow bandwidth PRESS sequences. For each fatty acid, the peak area is enhanced at each TE when employing the narrow bandwidth PRESS sequence. The responses for heptanoic, octanoic, linoleic and oleic acid, were fit to monoexponentially decaying functions, and M_o and T_2 values were determined. M_o and T_2 values obtained with each of the five data sets demonstrated CVs between 0.3 – 2.8 % except for the heptanoic and linoleic standard bandwidth M_o, which had CVs between 6 – 7 %. The narrow bandwidth data for hexanoic acid was also fitted; however, the signal to noise ratio for

the standard bandwidth data was too low to enable fitting. The narrow bandwidth PRESS sequence results in significantly different values as summarized in Table 3.1. The responses of the methylene protons of corn oil and of tibial bone marrow were similar to that of oleic acid and the curve fits resulted in M_o and T_2 values also shown in table 3.1. Over the six volunteers, an average enhancement of $20.8\ \%$ and $8.8\ \%$ was obtained for M_o and T_2, respectively, when employing the narrow bandwidth PRESS sequence. Paired t-tests confirmed statistical significance of the differences in M_o and T_2values obtained with the two PRESS sequences; p-values $<< 0.001$ were obtained for both M_o and T_2. Reproducibility of the data was verified by acquiring five data sets with the narrow bandwidth PRESS sequence ($TE = 100$ ms, 120 ms, 140 ms, 160 ms, 200 ms) from one of the volunteers. Methylene peak areas obtained with each TE, except $TE = 200$ ms, exhibited a $CV < 2\%$; the data with $TE = 200$ ms had a CV of $< 3\ \%$. M_o and T_2 values obtained with each of the five data sets demonstrated a CV of approximately $4.2\ \%$ and $2.7\ \%$, respectively. Figure 3.5 displays the mean and standard deviation of 1.3 ppm methylene peak areas obtained from the reproducibility experiments for each fatty acid phantom. Figure 3.6a displays the 1.3 ppm peak area as a function of TE for one volunteer. Figure 3.6b presents acquired spectra from the same volunteer obtained with TE values of 120 ms and 200 ms with both the standard and the narrow bandwidth PRESS sequences. Table 3.1 also includes T_2 values determined from the response of heptanoic, octanoic, linoleic and oleic acid to STEAM (TE = 100 ms, 120 ms, 140 ms, 160 ms, 180 ms and 200 ms, TM = 20 ms) for comparison to the T_2 values determined with the standard bandwidth PRESS sequence.

Phantom or subject	PRESS Standard Bandwidth T_2 (ms)	PRESS Narrow Bandwidth T_2 (ms)	% change in T_2	STEAM T_2 (ms)	PRESS Standard Bandwidth M_0	PRESS Narrow Bandwidth M_0	% change in M_o
Heptanoic	28.1 ± 0.5	83.6 ± 0.9	197.5 %	69.2	28.8 ± 1.8	6.6 ± 0.1	-77.1 %
Octanoic	53.1 ± 0.1	87.3 ± 0.9	64.4 %	75.2	12.9 ± 0.1	10.1 ± 0.1	-21.7 %
Linoleic	57.6 ± 1.5	83.1 ± 1.4	44.3%	67.8	6.8 ± 0.5	8.7 ± 0.2	27.9 %
Oleic	75.3 ± 0.3	90.3 ± 1.0	19.9 %	81.3	12.2 ± 0.1	15.0 ± 0.3	23.0 %
Corn	70.5	79.8	13.2 %	-	8.5	11.0	29.4 %
Volunteer #1	83.1	91.3	9.9 %	-	34.3	41.0	19.5 %
Volunteer #2	88.4	94.7	7.1 %	-	44.8	55.2	23.2 %
Volunteer #3	84.7	91.7	8.3 %	-	50.2	62.3	24.1 %
Volunteer #4	86.7	93.7	8.1%	-	44.2	53.9	21.9%
Volunteer #5	86.9	96.1	10.6%	-	48.7	57.4	17.9%
Volunteer #6	87.9	95.4	8.5%	-	59.1	69.8	18.1%

Table 3.1– Summary of M_o and T_2 values obtained for the 1.3 ppm lipid protons with the different pulse sequences. For the PRESS heptanoic, octanoic, linoleic and oleic acid data, the mean M_o and T_2 values obtained over the five acquired data sets are shown along with their standard deviations.

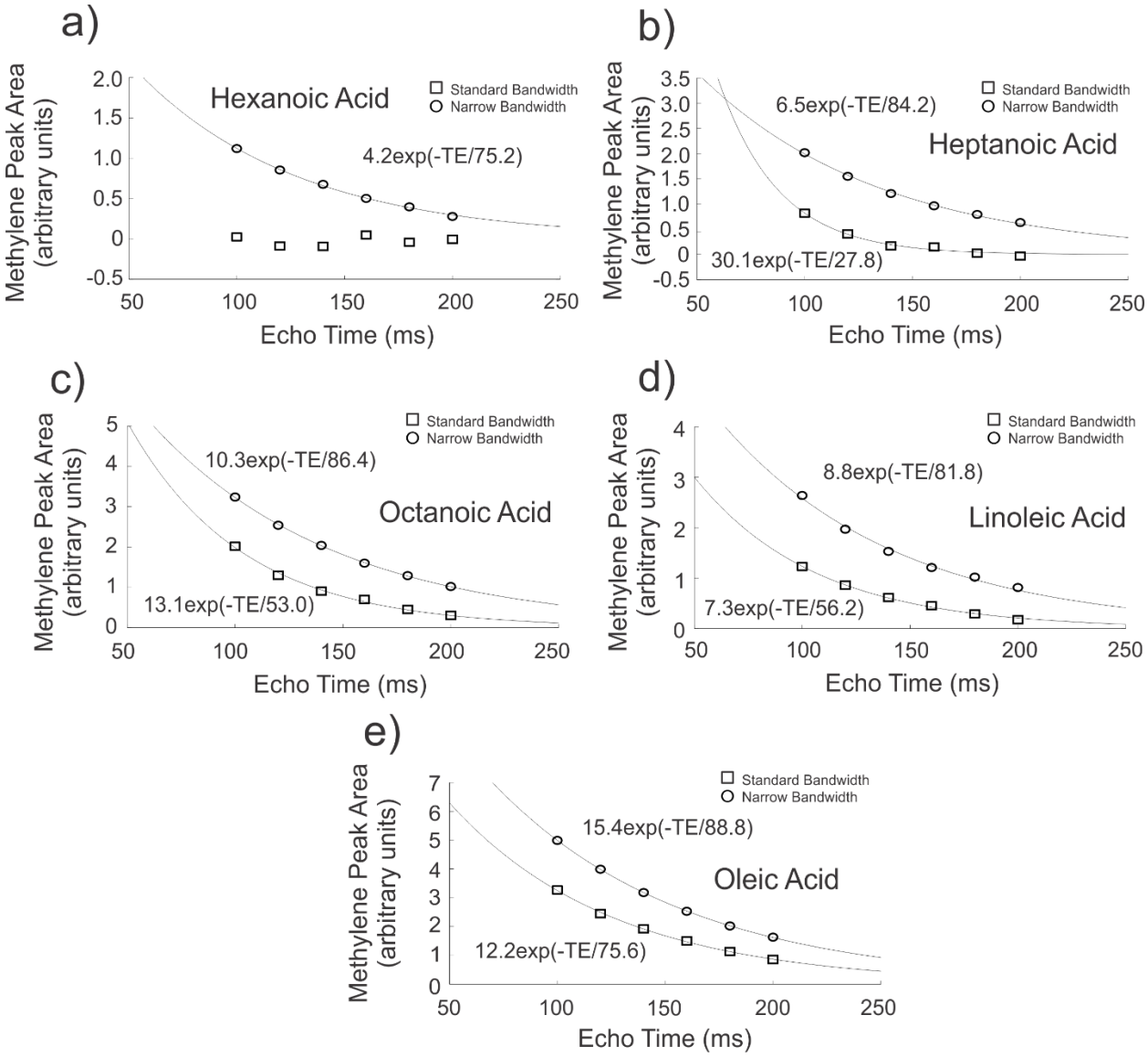

Figure 3.4 – 1.3 ppm methylene peak areas as a function of TE in response to the standard and narrow bandwidth PRESS sequences for (a) hexanoic, (b) heptanoic, (c) octanoic, (d) linoleic and (e) oleic acid. The monoexponential fits are displayed; all have R^2 values of greater than 0.992 except the fit for the standard bandwidth heptanoic data, which has an R^2 of 0.903. For figures (b) - (e) only one dataset out of five is shown.

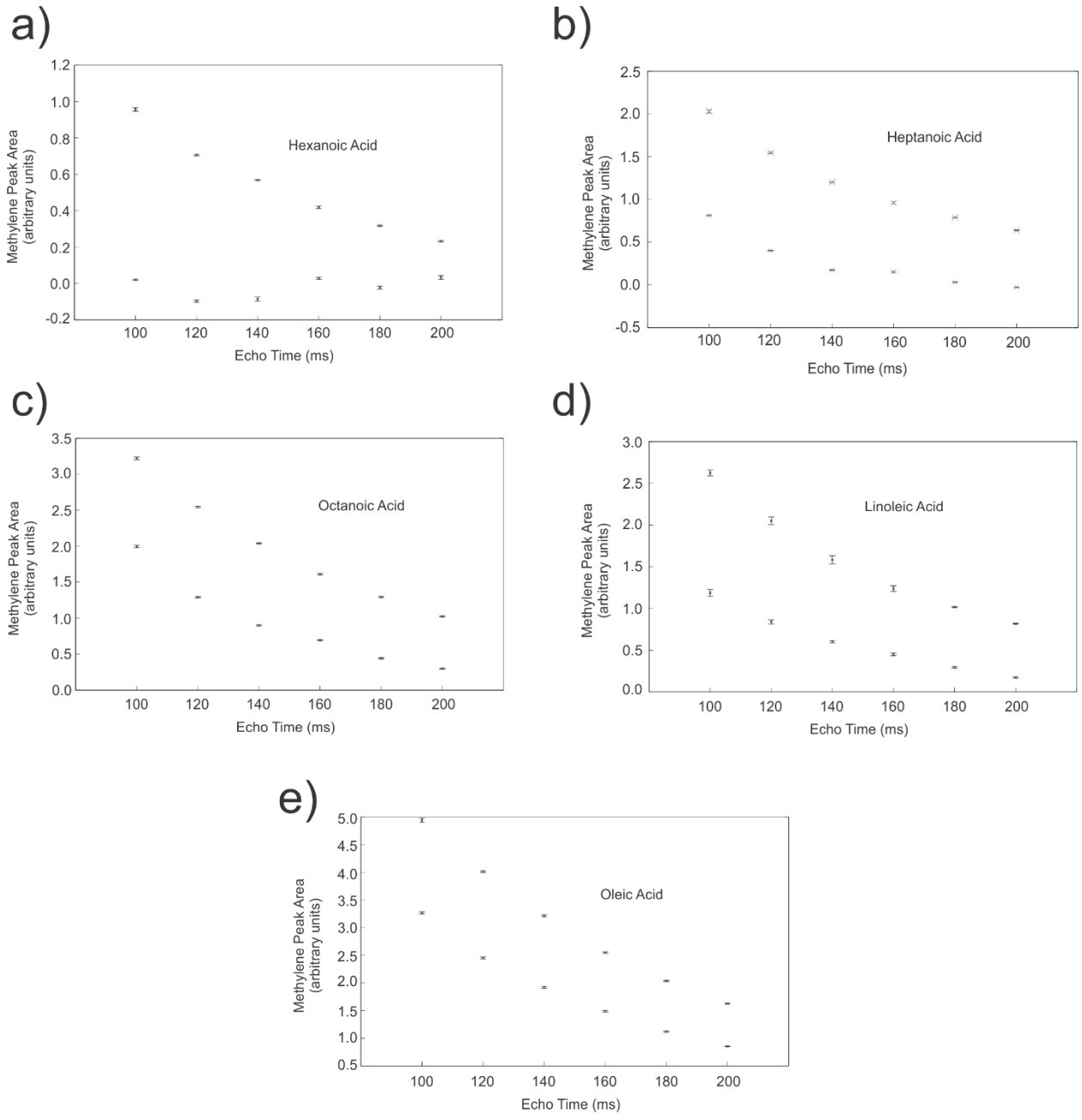

Figure 3.5 – Mean values and standard deviation of the 1.3 ppm methylene peak areas as a function of TE in response to the reproducibility tests of the standard and narrow bandwidth PRESS sequences for (a) hexanoic, (b) heptanoic, (c) octanoic, (d) linoleic and (e) oleic acid. Each TE is the mean of five signal acquisitions. The error bars represent ± standard deviation of the five measurements.

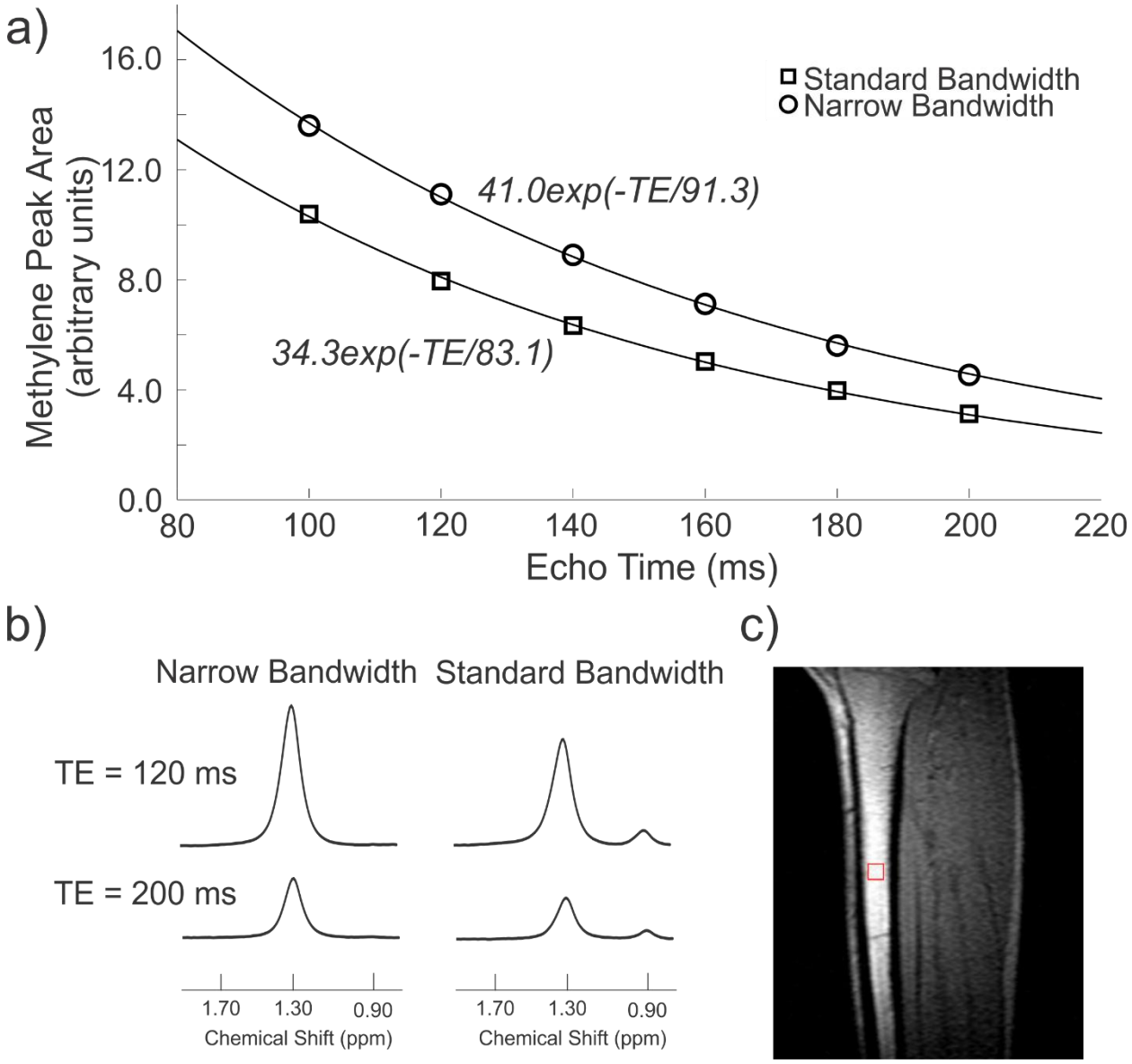

Figure 3.6 – Panel (a) displays the 1.3 ppm methylene peak areas acquired from tibial bone marrow of one volunteer as a function of TE in response to the standard and narrow bandwidth PRESS sequences. The monoexponential fits are displayed; R^2 values of greater than 0.999 were obtained for both fits. Panel (b) shows spectra obtained with TE values of 120 and 200 ms acquired using both versions of PRESS. The voxel location is illustrated in (c) on a sagittal scout image of the left leg of one volunteer.

3.5 – Discussion

The objective of this work is to investigate, at 3 T, the impact of J-coupling interactions on the quantification and T_2 determination of 1.3 ppm lipid methylene protons. Effects due to the J-coupling interactions have been previously observed (16,19-21); however, the monoexponential nature of the signal decay with increasing TE tends to alleviate concerns of quantification errors (17,18). In this work, we investigated the response of the 1.3 ppm protons to PRESS and STEAM in fatty acids of different chain lengths to gain insight into the decay response. Furthermore, we employed a PRESS sequence with refocussing pulses of 50 Hz bandwidth to rewind weak coupling interactions exhibited by 1.3 ppm lipid methylene protons, namely, with neighbouring 0.9 ppm methyl and 2.1 ppm allylic protons. The technique enabled us to estimate errors that occur in the determination of M_o and T_2 values due to J-coupling evolution.

Significant signal modulation is observed in the response of the four hexanoic acid methylene protons as a function of PRESS and STEAM echo time in figure 3.2a. The modulations are due to J-coupling interactions with neighbouring 0.9 ppm and 1.6 ppm protons. As the methylene chain length increases and more "inner" uncoupled CH_2 groups are introduced, the modulations due to signal evolution of the coupled protons become diluted by the dominating monoexponential T_2 decay of the uncoupled protons. Small oscillations are visible for heptanoic, octanoic and linoleic acid but in the case of oleic acid, where only eight of the twenty methylene protons are coupled to neighbouring protons, the majority of the 1.3 ppm methylene signal originates from uncoupled protons and therefore the response appears monoexponential and free from oscillations.

For a more quantitative assessment of the extent to which J-coupling interactions affect the quantification and T_2 determination of 1.3 ppm lipid methylene protons, the narrow bandwidth PRESS method was applied. As can be seen in Fig. 3.4, the narrow bandwidth PRESS sequence results in excellent monoexponential fits (R^2 values greater than 0.992 were calculated for the narrow bandwidth data and all narrow bandwidth R^2 values were greater than their respective value for standard bandwidth) for the five fatty acids and in significantly enhanced signal at each TE compared to the standard bandwidth PRESS sequence. The enhancement is a result of rewinding J-coupling evolution due to interactions with the 0.9 ppm methyl protons and also, in the case of linoleic acid and oleic acid, the 2.1 ppm allylic protons. The method does not rewind the strong coupling evolutions due to coupling with the 1.6 ppm protons. The limitation of incomplete rewinding of all J-coupling evolution due to strong coupling interactions with the 1.6 ppm protons is present for all the fatty acids; however, the effect on the narrow bandwidth signal response is most significant for hexanoic acid where 50 % of the methylene protons are strongly coupled to the 1.6 ppm protons. The fraction of strongly coupled 1.3 ppm protons is lower for the other four fatty acids, namely, 33.3 %, 25 %, 14 % and 10 % for heptanoic, octanoic, linoleic acid and oleic acid, respectively. With the four fatty acids, the narrow bandwidth PRESS technique yielded a higher T_2 compared to standard PRESS because results from the latter include losses due to J-coupling (an apparent T_2). The increase in T_2 is most significant for the case of heptanoic acid ($\approx 198\%$) followed by octanoic acid ($\approx 64\%$) and linoleic acid (≈ 44 %) and then oleic acid ($\approx 20\%$). As the methylene chain length increases and the fraction of coupled protons in the chain decreases, the apparent T_2 value, which includes losses due to J-coupling, approaches the more representative T_2 values

obtained with the narrow bandwidth sequence. In all four cases, the M_o values are significantly affected by the presence of J-coupling interactions. For heptanoic acid, where $67\ \%$ of the methylene chain protons are J-coupled, the M_o value is overestimated by almost a factor of 4.5. While the consequence of J-coupling on M_o determination for oleic acid, an important constituent of lipids *in vivo*, is not as large, M_o is underestimated by $\approx 18\ \%$ due to the presence of J-coupling interactions among some of the methylene chain protons. The effect of J-coupling on M_o and T_2 values was also investigated for corn oil, which is composed of approximately $13.5\ \%$ saturated fatty acids, $32.5\ \%$ oleic acid, and $52\ \%$ linoleic acid (36). J-coupling effects caused M_o and T_2values to be underestimated by $23\ \%$ and $12\ \%$, respectively.

T_2 values were also estimated for heptanoic, octanoic, linoleic acid and oleic acid with STEAM employing the signal areas obtained with TE values between 100 and $200\ ms$ to be consistent with the TE range employed for PRESS. As can be seen from table 3.1, consistent with previous findings (16), the T_2 values obtained with STEAM are higher than those obtained with standard PRESS. The T_2 values obtained with STEAM agree more closely with the T_2values obtained with the narrow bandwidth PRESS sequence indicating that J-coupling interactions have less of an effect on the response of the methylene protons to STEAM compared to PRESS. This may be due to intrapulse J-coupling evolutions which take place during the PRESS 180° pulses (37), effects which have been shown to be less significant with STEAM (38). It is of significance to note that with both standard PRESS and STEAM the measured T_2 for linoleic acid is less than that of oleic acid (the narrow bandwidth PRESS method shows that they both have comparable T_2 values) indicating that measures of T_2 with standard techniques will be influenced by lipid composition.

To evaluate the effects of J-coupling on M_o and T_2 determination of 1.3 ppm lipid methylene protons *in vivo*, we studied the response of tibial bone marrow in six healthy volunteers. Tibial bone marrow is composed primarily of about 19 % linoleic acid, 45 % oleic acid and 28 % saturated fatty acids (39) Employing the narrow bandwidth PRESS sequence yielded an average increase of ≈ 21 % and 9 % for M_o and T_2, respectively, over the six volunteers. The standard bandwidth PRESS technique resulted in a mean T_2 of 86.3 ms (standard deviation of 2.0 ms) while the narrow bandwidth PRESS technique yielded a mean T_2 of 93.8 ms (standard deviation of 2.0 ms). The differences between M_o and T_2 values determined by the two PRESS sequences *in vivo* are a few percent less compared to those observed in corn oil. This is likely explained by the larger proportion of oleic acid and long chain saturated fatty acids found *in vivo*, which have a mean number of 25 methylene protons, only four of which are coupled to neighbouring protons. It should also be noted that because the narrow bandwidth method does not rewind J-coupling evolution due to strong coupling interactions with the 1.6 ppm protons, the M_o and T_2values determined by the technique likely underestimate true M_o and T_2values. However, because only about 9 % of the methylene chain protons are involved in coupling with the 1.6 ppm protons, it is not expected to significantly affect the results.

A consequence of underestimating the lipid methylene M_o is an underestimation of fat fraction, which is often calculated as the methylene peak area divided by the sum of the methylene peak area and that of water (40). For example, in healthy spinal bone marrow the fat fraction lies in the range of $0.25 - 0.55$(40); a fat to water area ratio of 0.45 measured with standard PRESS results in a fat fraction of 0.31. Compensating the fat area for J-coupling

effects by multiplication by a factor of 1.2 results in a fat fraction of 0.35, a value approximately 13 %higher. In liver, where fat fractions as low as 0.5 %(41) can be measured the error would be about 20 %. In conclusion, we have demonstrated that J-coupling interactions of 1.3 ppm lipid methylene protons *in vivo* can lead to underestimations of their levels and T_2 values by about 20 % and 10 %, respectively. Although J-coupling effects have been noted in magnetic resonance imaging and spectroscopy studies, it has been difficult to estimate the quantification errors they introduce because of the monoexponential nature of the signal decay as a function of echo time. Fitting the signal to a function of the form $M_o\exp(-TE/T_2)[\cos(\pi JTE)+b]$ as was done by Ref. (30) is not appropriate since the model neglects a monoexponentially decay term for uncoupled spins and it assumes a simple two spin system. The presented work minimizes J-coupling effects by using the narrow bandwidth PRESS technique. A limitation of the technique is that it enables improved quantification of the methylene protons at the expense of losing information about other lipid peaks. However, the intent of the presented work was to use the methodology to enable an assessment of the consequences of J-coupling interactions of the 1.3 ppm methylene protons to be made.

3.7 – References

1. Qi J, Fong Y, Saltz L, et al. Serial measurement of hepatic lipids during chemotherapy in patients with colorectal cancer: a ^{1}H MRS study. NMR Biomed 2013;26:204-212.
2. Chabanova E, Bille DS, Thisted E, Holm JC, Thomsen HS. ^{1}H MRS assessment of hepatic steatosis in overweight children and adolescents: comparison between 3T and open 1T MR-systems. Abdom Imaging 2013;38:315-319.
3. Griffith JF, Yeung DKW, Antonio GE, et al. Vertebral bone mineral density, marrow perfusion, and fat content in healthy men and men with osteoporosis: dynamic contrast-enhanced MR imaging and MR spectroscopy. Radiology 2005;236:945-951.
4. Chernov MF, Hayashi M, Izawa M, Ono Y, Hori T. Proton magnetic resonance spectroscopy (MRS) of metastatic brain tumors: variations of metabolic profile. Int J Clin Oncol 2006;11:375-384.
5. Kumar M, Jagannathan NR, Seenu V, Dwivedi SN, Julka PK, Rath GK. Monitoring the therapeutic response of locally advanced breast cancer patients: sequential in vivo proton MR spectroscopy study. J Magn Reson Imaging 2006;24:325-332.
6. Venkatesh BA, Lima JAC, Bluemke DA, Lai S, Steenbergen C, Liu CY. MR proton spectroscopy for myocardial lipid deposition quantification: a quantitative comparison between 1.5T and 3T. J Magn Reson Imaging 2012;36:1222-1230.
7. Oriol A, Valverde D, Capellades J, Cabañas ME, Ribera JM, Arús C. In vivo quantification of response to treatment in patients with multiple myeloma by ^{1}H magnetic resonance spectroscopy of bone marrow. Magn Reson Mater Phy 2007;20:93-101.
8. Borra R, Lautamäki R, Parkkola R, et al. Inverse association between liver fat content and hepatic glucose uptake in patients with type 2 diabetes mellitus. Metabolism 2008;57:1445-1451.
9. Kotronen A, Juurinen L, Tiikkainen M, Vehkavaara S, Yki-Järvinen H. Increased liver fat, imparied insulin clearance, and hepatic adipose tissue insulin resistance in type 2 diabetes. Gastroenterology 2008;135:122-130.

10. Perseghin G, Scifo P, De Cobelli F, et al. Intramyocellular triglyceride content is a determinant of in vivo insulin resistance in humans. Diabetes 1999;48:1600-1606.
11. Li X, Kuo D, Schafer AL, et al. Quantification of vertebral bone marrow fat content using 3 Tesla MR spectroscopy: reproducibility, vertebral variation, and applications in osteoporosis. J Magn Reson Imaging 2011;33:974-979.
12. Hayashi N, Miyati T, Minami T, et al. Quantitative analysis of hepatic fat fraction by single-breath-holding MR spectrscopy with T_2 correction: phantom and clinical study with histologic assessment. Radiol Phys and Technol 2013;6(1):219-225.
13. Bottomley PA. Selective volume method for performing localized NMR spectroscopy. . U.S. ; 1984.
14. Frahm J, Merboldt KD, Hanioke W. Localized proton spectroscopy using stimulated echoes. J Magn Reson 1987;72:502-508.
15. Smith IC, Princz EJ, Saunders JK. Magnetic resonance spectroscopy in cancer research. Can Assoc Radiol J 1990;41(1):32-38.
16. Hamilton G, Middleton MS, Bydder M, et al. Effect of PRESS and STEAM sequences on magnetic resonance spectroscopic liver fat quantification. J Magn Reson Imaging 2009;30:145-152.
17. Yahya A, Fallone BG. T_2 determination of the J-coupled methyl protons of lipids: in vivo illustration with tibial bone marrow at 3 T J Magn Reson Imaging 2010;31:1514-1521.
18. Gambarota G, Tanner M, van der Graaf M, Mulkern RV, Newbould RD. ^{1}H-MRS of hepatic fat using short TR at 3T: SNR optimization and fast T2 relaxometry. Magn Reson Mater Phy 2011;24(6):339-345.
19. Stokes AM, Feng Y, Mitropoulos T, Warren WS. Enhanced refocusing of fat signals using optimized multipulse echo sequences. Magn Reson Med 2013;69:1044-1055.
20. Henkelman RM, Hardy PA, Bishop JE, Poon CS, Plewes DB. Why fat is bright in RARE and fast spin-echo imaging. J Magn Reson Imaging 1992;2:533-540.
21. Melki P, Mulkern R, Lawrence P, Jolesz F. Comparing the FAISE Method with Conventional Dual-Echo Sequences. Journal of Magnetic Resonance Imaging 1991;1:319-326.

22. Constable R, Anderson A, Zhong J, Gore J. Factors Influencing Contrast In Fast Spin-Echo MR Imaging. Magnetic Resonance Imaging 1992;10:497-511.
23. Hinks R, Martin D. Bright Fat, Fast Spin Echo, and CPMG. Proceedings of the Society of Magnetic Resonance in Medicine 11th Annual Meeting 1992:4503.
24. Peled S, Williamson D, Mulkern R. Signal Intensity Studies of Strongly-Coupled Spin Systems during CPMG/RARE Imaging Sequences. Proceedings of the Society of Magnetic Resonance Third Scientific Meeting 1995:655.
25. Rutt B, Wright G. Lipid Signal Enhancement in CPMG MRI: Effect of Field Strength. Proceedings of the Society of Magnetic Resonance in Medicine 11th Annual Meeting 1992:4504.
26. Williamson D, Mulkern R, Jakab P, Jolesz F. Coherence Transfer by Isotropic Mixing in Carr-Purcell-Meiboom-Gill Imaging: Implications for the Bright Fat Phenomenon in Fast Spin-Echo Imaging. Magnetic Resonance in Medicine 1996;35:506-513.
27. Wright G, Macovski A. Lipid Signal Enhancement in Spin-Echo Trains. Proceedings of the Society of Magnetic Resonance in Medicine 11th Annual Meeting 1992:437.
28. Allerhand A. Analysis of Carr-Purcell Spin-Echo NMR Experiments on Multiple-Spin Systems. The Journal of Chemical Physics 1966;44(1):1-9.
29. Stables L, Kennan R, Anderson A, Gore J. Density Matrix Simulations of the Effects of J Coupling in Spin Echo and Fast Spin Echo Imaging. Journal of Magnetic Resonance 1999;140:305-314.
30. Gajdošík M, Chmelík M, Just-Kukurová I, et al. In vivo relaxation behavior of liver compounds at 7 Tesla, measured by single-voxel proton MR spectroscopy. J Magn Reson Imaging 2014;40:1365-1374.
31. Yahya A, Tessier AG, Fallone BG. Effect of J-coupling on lipid composition determination with localized proton magnetic resonance spectroscopy at 9.4 T. J Magn Reson Imag 2011;34:1388-1396.
32. Yahya A, Mädler B, Fallone BG. Exploiting the chemical shift displacement effect in the detection of glutamate and glutamine (Glx) with PRESS. J Magn Reson Imaging 2008;191:120-127.

33. Yablonskiy DA, Neil JJ, Raichle ME, Ackerman JJH. Homonuclear J coupling effects in volume localized NMR spectroscopy: Pitfalls and solutions. Magn Reson Med 1998;39:169-178.

34. Träber F, Block W, Lamerichs R, Gieseke J, Schild HH. ^{1}H metabolite relaxation times at 3.0 tesla: measurements of T1 and T2 values in normal brain and determination of regional differences in transverse relaxation. J Magn Reson Imag 2004;19:537-545.

35. Helms G. Analysis of 1.5 tesla proton MR spectra of human brain using LCModel and an imported basis set. Magn Reson Imag 1999;17:1211-1218.

36. Guillén MD, Ruiz A. Rapid simultaneous determination by proton NMR of unsaturation and composition of acyl groups in vegetable oils. Eur J Lipid Sci Technol 2003;105:688-696.

37. Thompson RB, Allen PS. Sources of variability in the response of coupled spins to the PRESS sequence and their potential impact on metabolite quantification. Magn Reson Med 1999;41:1162-1169.

38. Thompson RB, Allen PS. Response of metabolites with coupled spins to the STEAM sequence. Magn Reson Med 2001;45:955-965.

39. Griffith JF, Yeung DKW, Ahuja A, et al. A study of bone marrow and subcutaneous fatty acid composition in subjects of varying bone mineral density. Bone 2009;44:1092-1096.

40. Kugel H, Jung C, Shulte O, Henidel W. Age- and sex-specific differences in the ^{1}H spectrum of vertebral bone marrow. J Magn Reson Imag 2001;13:263-268.

41. Machann J, Thamer C, Schnoedt B, et al. Hepatic lipid accumulation in healthy subjects: a comparative study using spectral fat-selective MRI and volume-localized ^{1}H-MR spectroscopy. Magn Reson Med 2006;55:913-917.

Chapter 4 – Conclusion

4.1 – Concluding Remarks

The primary objective of the work performed in this thesis has been to demonstrate the significance of J-coupling effects on the quantification and T_2 estimation of $1.3\ ppm$ lipid methylene protons. Using a modified PRESS MRS sequence, which employed narrow bandwidth refocussing pulses, the J-coupling evolution due to weak coupling interactions of $1.3\ ppm$ lipid methylene protons in phantoms and from *in-vivo* tibial bone marrow was largely rewound. In the absence of J-coupling evolution from weak coupling interactions, the values of M_0 and T_2 determined by the narrow bandwidth PRESS sequence for *in-vivo* tibial bone marrow of six volunteers were $\sim 21\ \%$ and $\sim 9\ \%$ higher, respectively, in comparison to a standard PRESS sequence. The results indicate that the effects of J-coupling on quantification aspects of the $1.3\ ppm$ lipid methylene signal are not negligible.

Despite previously noted effects of J-coupling on $1.3\ ppm$ lipid methylene signal(1-10), only one other study to date has attempted to account for J-coupling effects on the lipid methylene signal(11). Unfortunately, the study was unable to compensate for the *in vivo* J-coupling effects of $1.3\ ppm$ methylene protons due to the limitations of the simplified model being used to account for signal evolution and the minimal appearance of signal modulation seen *in vivo*. Furthermore, the non-obvious J-coupling modulation observed *in vivo* is the primary reason why the J-coupling effects have been overlooked to date in MRS studies. In

addition to estimating the extent to which the values of M_0 and T_2 of the $1.3\,ppm$ lipid methylene protons are underestimated *in vivo*, the work performed in this thesis indicates that the dominating monoexponential nature of the$1.3\,ppm$ lipid methylene proton signal decay *in vivo* is attributed to the high proportion of uncoupled CH_2 protons present in the long chain fatty acids which dominate the constituents of adipose tissue and bone marrow.

It was found that the determined values of T_2 were larger when acquired with a STEAM pulse sequence in comparison to a PRESS sequence – the same observation made by Hamilton et al(1). The magnitude of the difference in acquired T_2 values was found to correlate with fatty acid chain length with shorter chain fatty acids, displaying the largest discrepancy – the STEAM T_2 of $1.3\,ppm$ methylene protons value of heptanoic acid was $146\,\%$ higher than PRESS whereas this value was only $8\,\%$ higher for oleic acid. The correlation to chain length indicates that the difference in J-coupling evolution under the two sequences is the cause of the discrepancies. Furthermore, it is worthwhile to note that the determined T_2 value of the $1.3\,ppm$ methylene protons of oleic acid differed from that of linoleic acid by about $31\,\%$ and $20\,\%$, when employing PRESS and STEAM, respectively, implying that lipid composition has an effect on the determined T_2 value.

The values of M_0 and T_2 of $1.3\,ppm$ lipid methylene protons have been used in previous studies to investigate various diseases including cancer, diabetes, osteoporosis and non-alcoholic fatty liver disease. While the accuracy of M_0 and T_2 required in each of the studies depends on the methodology being used, for any study investigating changes in M_0 and T_2 values between healthy and diseased tissue discrepancies of $21\,\%$ and $9\,\%$ will be significant if absolute quantification is the goal. Based on previous studies, it is apparent that no consensus

has been achieved with regard to the best way of evaluating changes in the values of M_0 between healthy and diseased tissue. For example, the paper by Oriol et al. defines a lipid to water ratio greater than one in spinal bone marrow to indicate the positive response of patients with multiple myeloma to chemotherapy. This definition of response is based solely on the fact that all patients deemed responsive to treatment exhibited a lipid-water ratio greater than one. However, the definition of response used by Oriol et al. cannot be generalized and cannot be considered to be absolute due to variable choice of spectroscopic methodology, relaxation and J-coupling effects, and inter-patient variation of water and lipid quantities.

The presented work is the first to estimate by how much J-coupling evolution affects quantification and T_2 estimation of the $1.3\ ppm$ lipid methylene protons determined by a PRESS pulse sequence. The work raises awareness that although a large percentage of the protons contributing signal to the $1.3\ ppm$ resonance are uncoupled, the J-coupling interactions of the remaining protons do affect quantification.

The work conducted for this thesis is part of a larger research program investigating aspects of lipid quantification with *in-vivo* proton magnetic resonance spectroscopy. Future work will build upon the work in this thesis by further assessing the effect of lipid composition on measured T_2 values and investigating the consequences of J-coupling evolution at $9.4\ T$ (a field strength commonly employed in animal model studies of disease), where all the J-coupling interactions of the $1.3\ ppm$ methylene protons fall under the weakly-coupled regime.

4.2 – References

1. Hamilton G, Middleton MS, Bydder M, Yokoo T, Schwimmer JB, Kono Y, Patton HM, Lavine JE, Sirlin CB. Effect of PRESS and STEAM sequences on magnetic resonance spectroscopic liver fat quantification. *J Magn Reson Imaging* 2009; **30**: 145-152.
2. Henkelman RM, Hardy PA, Bishop JE, Poon CS, Plewes DB. Why fat is bright in RARE and fast spin-echo imaging. *J Magn Reson Imaging* 1992; **2**: 533-540.
3. Constable R, Anderson A, Zhong J, Gore J. Factors Influencing Contrast In Fast Spin-Echo MR Imaging. *Magnetic Resonance Imaging* 1992; **10**: 497-511.
4. Hinks R, Martin D. Bright Fat, Fast Spin Echo, and CPMG. *Proceedings of the Society of Magnetic Resonance in Medicine 11th Annual Meeting* 1992: 4503.
5. Listerud J, Mulkern R. The J Coupling Hypothesis for Bright Fat observed on FSE. *Proceedings of the Society of Magnetic Resonance in Medicine 11th Annual Meeting* 1992: 4505.
6. Melki P, Mulkern R, Lawrence P, Jolesz F. Comparing the FAISE Method with Conventional Dual-Echo Sequences. *Journal of Magnetic Resonance Imaging* 1991; **1**: 319-326.
7. Peled S, Williamson D, Mulkern R. Signal Intensity Studies of Strongly-Coupled Spin Systems during CPMG/RARE Imaging Sequences. *Proceedings of the Society of Magnetic Resonance Third Scientific Meeting* 1995: 655.
8. Rutt B, Wright G. Lipid Signal Enhancement in CPMG MRI: Effect of Field Strength. *Proceedings of the Society of Magnetic Resonance in Medicine 11th Annual Meeting* 1992: 4504.
9. Williamson D, Mulkern R, Jakab P, Jolesz F. Coherence Transfer by Isotropic Mixing in Carr-Purcell-Meiboom-Gill Imaging: Implications for the Bright Fat Phenomenon in Fast Spin-Echo Imaging. *Magnetic Resonance in Medicine* 1996; **35**: 506-513.
10. Wright G, Macovski A. Lipid Signal Enhancement in Spin-Echo Trains. *Proceedings of the Society of Magnetic Resonance in Medicine 11th Annual Meeting* 1992: 437.

11. Gajdošík M, Chmelík M, Just-Kukurová I, Bogner W, Valkovič L, Trattnig S, Krššák M. In vivo relaxation behavior of liver compounds at 7 Tesla, measured by single-voxel proton MR spectroscopy. *J Magn Reson Imaging* 2014; **40**: 1365-1374.

Bibliography

1. Rabi I, Millman S, Kusch P. The Molecular Beam Resonance Method for Measuring Nuclear Magnetic Moments. *Physical Review* 1939; **55**.
2. Proctor W, Yu F. The Dependence of a Nuclear Magnetic Resonance Frequency Upon Chemical Compound. *Physical Review* 1950; **77**.
3. de Graaf R. *In Vivo* NMR Spectroscopy: John Wiley & Sons Ltd.; 2007.
4. Chernov MF, Hayashi M, Izawa M, Ono Y, Hori T. Proton magnetic resonance spectroscopy (MRS) of metastatic brain tumors: variations of metabolic profile. *Int J Clin Oncol* 2006; **11**: 375-384.
5. Kumar M, Jagannathan NR, Seenu V, Dwivedi SN, Julka PK, Rath GK. Monitoring the therapeutic response of locally advanced breast cancer patients: sequential in vivo proton MR spectroscopy study. *J Magn Reson Imaging* 2006; **24**: 325-332.
6. Oriol A, Valverde D, Capellades J, Cabañas ME, Ribera JM, Arús C. In vivo quantification of response to treatment in patients with multiple myeloma by ^{1}H magnetic resonance spectroscopy of bone marrow. *Magn Reson Mater Phy* 2007; **20**: 93-101.
7. Qi J, Fong Y, Saltz L, D'Angelica MI, Kemeny NE, Gonen M, Shia J, Shukla-Dave A, Jarnagin WM, Do RKG, Schwartz LH, Koutcher JA, Zakian KL. Serial measurement of hepatic lipids during chemotherapy in patients with colorectal cancer: a ^{1}H MRS study. *NMR Biomed* 2013; **26**: 204-212.
8. Borra R, Lautamäki R, Parkkola R, Komu M, Sijens PE, Hällsten K, Bergman J, Iozzo P, Nuutila P. Inverse association between liver fat content and hepatic glucose uptake in patients with type 2 diabetes mellitus. *Metabolism* 2008; **57**: 1445-1451.
9. Kotronen A, Juurinen L, Tiikkainen M, Vehkavaara S, Yki-Järvinen H. Increased liver fat, imparied insulin clearance, and hepatic adipose tissue insulin resistance in type 2 diabetes. *Gastroenterology* 2008; **135**: 122-130.
10. Perseghin G, Scifo P, De Cobelli F, Pagliato E, Battezzati A, Arcelloni C, Vanzulli A, Testolin G, Pozza G, Del Maschio A, Luzi L. Intramyocellular triglyceride content is a determinant of in vivo insulin resistance in humans. *Diabetes* 1999; **48**: 1600-1606.

11. Chabanova E, Bille DS, Thisted E, Holm JC, Thomsen HS. ^{1}H MRS assessment of hepatic steatosis in overweight children and adolescents: comparison between 3T and open 1T MR-systems. *Abdom Imaging* 2013; **38**: 315-319.
12. Hayashi N, Miyati T, Minami T, Takeshita Y, Ryu Y, Matsuda T, Ohno N, Hamaguchi T, Kato K, Takamura T, Matsui O. Quantitative analysis of hepatic fat fraction by single-breath-holding MR spectrscopy with T_2 correction: phantom and clinical study with histologic assessment. *Radiol Phys and Technol* 2013; **6**: 219-225.
13. Griffith JF, Yeung DKW, Antonio GE, Lee FKH, Hong AWL, Wong SYS, Lau EMC, Leung PC. Vertebral bone mineral density, marrow perfusion, and fat content in healthy men and men with osteoporosis: dynamic contrast-enhanced MR imaging and MR spectroscopy. *Radiology* 2005; **236**: 945-951.
14. Li X, Kuo D, Schafer AL, Porzig A, Link TM, Black D, Schwartz AV. Quantification of vertebral bone marrow fat content using 3 Tesla MR spectroscopy: reproducibility, vertebral variation, and applications in osteoporosis. *J Magn Reson Imaging* 2011; **33**: 974-979.
15. Smith IC, Princz EJ, Saunders JK. Magnetic resonance spectroscopy in cancer research. *Can Assoc Radiol J* 1990; **41**: 32-38.
16. Bottomley P. Selective volume method for performing localized NMR spectrscopy. *US patent 4,480,228* 1984.
17. Frahm J, Merboldt K, Hanioke W. Localized proton spectroscopy using stimulated echoes. *J Magn Reson* 1987; **72**: 502-508.
18. Venkatesh BA, Lima JAC, Bluemke DA, Lai S, Steenbergen C, Liu CY. MR proton spectroscopy for myocardial lipid deposition quantification: a quantitative comparison between 1.5T and 3T. *J Magn Reson Imaging* 2012; **36**: 1222-1230.
19. Hamilton G, Middleton MS, Bydder M, Yokoo T, Schwimmer JB, Kono Y, Patton HM, Lavine JE, Sirlin CB. Effect of PRESS and STEAM sequences on magnetic resonance spectroscopic liver fat quantification. *J Magn Reson Imaging* 2009; **30**: 145-152.

20. Oostendorp M, Engelke UFH, Willemsen MAAP, Wevers RA. Diagnosing inborn errors of lipid metabolism with proton nuclear magnetic resonance spectroscopy. *Clin Chem* 2006; **52**: 1395-1405.
21. Stokes AM, Feng Y, Mitropoulos T, Warren WS. Enhanced refocusing of fat signals using optimized multipulse echo sequences. *Magn Reson Med* 2013; **69**: 1044-1055.
22. Henkelman RM, Hardy PA, Bishop JE, Poon CS, Plewes DB. Why fat is bright in RARE and fast spin-echo imaging. *J Magn Reson Imaging* 1992; **2**: 533-540.
23. Melki P, Mulkern R, Lawrence P, Jolesz F. Comparing the FAISE Method with Conventional Dual-Echo Sequences. *Journal of Magnetic Resonance Imaging* 1991; **1**: 319-326.
24. Constable R, Anderson A, Zhong J, Gore J. Factors Influencing Contrast In Fast Spin-Echo MR Imaging. *Magnetic Resonance Imaging* 1992; **10**: 497-511.
25. Peled S, Williamson D, Mulkern R. Signal Intensity Studies of Strongly-Coupled Spin Systems during CPMG/RARE Imaging Sequences. *Proceedings of the Society of Magnetic Resonance Third Scientific Meeting* 1995: 655.
26. Williamson D, Mulkern R, Jakab P, Jolesz F. Coherence Transfer by Isotropic Mixing in Carr-Purcell-Meiboom-Gill Imaging: Implications for the Bright Fat Phenomenon in Fast Spin-Echo Imaging. *Magnetic Resonance in Medicine* 1996; **35**: 506-513.
27. Hinks R, Martin D. Bright Fat, Fast Spin Echo, and CPMG. *Proceedings of the Society of Magnetic Resonance in Medicine 11th Annual Meeting* 1992: 4503.
28. Rutt B, Wright G. Lipid Signal Enhancement in CPMG MRI: Effect of Field Strength. *Proceedings of the Society of Magnetic Resonance in Medicine 11th Annual Meeting* 1992: 4504.
29. Wright G, Macovski A. Lipid Signal Enhancement in Spin-Echo Trains. *Proceedings of the Society of Magnetic Resonance in Medicine 11th Annual Meeting* 1992: 437.
30. Gajdošík M, Chmelík M, Just-Kukurová I, Bogner W, Valkovič L, Trattnig S, Krššák M. In vivo relaxation behavior of liver compounds at 7 Tesla, measured by single-voxel proton MR spectroscopy. *J Magn Reson Imaging* 2014; **40**: 1365-1374.

31. Yahya A, Fallone BG. T_2 determination of the J-coupled methyl protons of lipids: in vivo ilustration with tibial bone marrow at 3 T *J Magn Reson Imaging* 2010; **31**: 1514-1521.
32. Tipler P, Llewellyn R. Modern Physics. New York: W. H. Freeman and Company; 2002.
33. Giancoli D. Physics for Scientists and Engineers. New Jersey: Prentice Hall; 2000.
34. Schroeder D. An Introduction to Thermal Physics: Addison Wesley Longman; 1999.
35. James T. Nuclear Magnetic Resonance In Biochemistry: Academic Press; 1975.
36. Callaghan P. Principles of Nuclear Magnetic Resonance Microscopy. Oxford: Oxford University Press; 1993.
37. Chavhan G, Babyn P, Thomas B, Shroff M, Haacke E. Principles, Techniques and Applications of T2* - based MR Imaging and Its Special Applications. *Radiographics* 2009; **29**: 1433 - 1449.
38. Hahn E. Spin Echoes. *Physical Review* 1950; **80**: 580-594.
39. Burstein D. Stimulated Echoes: Description, Applications, Practical Hints. *Concepts in Magnetic Resonance* 1996; **8**: 269-278.
40. Traber F, Block R, Lamerichs J. ^{1}H Metabolite Relaxation Times at 3.0 Tesla: Measurements of T_1 and T_2 Values in Normal Brain and Determinaton of Regional Differences in Transverse Relaxation. *Journal of Magnetic Resonance Imaging* 2004; **19**: 537-545.
41. Helms G. Analysis of 1.5 Tesla Proton MR Spectra of Human Brain Using LCmodel and an Imported Basis Set. *Magnetic Resonance Imaging* 1999; **17**: 1211-1218.
42. de Graaf R, Rothman D. *In Vivo* Detection and Quantification of Scalar Coupled ^{1}H NMR Resonances. *Concepts in Magnetic Resonance* 2001; **13**: 32-76.
43. Allerhand A. Analysis of Carr-Purcell Spin-Echo NMR Experiments on Multiple-Spin Systems. *The Journal of Chemical Physics* 1966; **44**: 1-9.
44. Leray C. Lipids Nutrition and Health: CRC Press; 2014.
Ren J, Dimitrov I, Sherry A, Malloy C. Composition of Adipose Tissue and Marrow Fat in Humans by ^{1}H NMR at 7 Tesla. *Journal of Lipid Research* 2008; **49**.

45. Yahya A, Mädler B, Fallone BG. Exploiting the chemical shift displacement effect in the detection of glutamate and glutamine (Glx) with PRESS. *J Magn Reson Imaging* 2008; **191**: 120-127.

46. Yablonskiy D, Neil J, Raichle M, Ackerman J. Homonuclear J Coupling Effects in Volume Localized NMR Spectroscopy: Pitfalls and Solutions. *Magnetic Resonance in Medicine* 1998; **39**: 169-178.

47. de Graaf R. *In Vivo* NMR Spectroscopy: John Wiley & Sons Ltd.; 2007.
Goulden C. Methods of Statistical Analysis. New York: Wiley; 1956.

48. Yahya A, Tessier A, Fallone B. Effect of J-Coupling on Lipid Composition Determination With Localized Proton Magnetic Resonance Spectroscopy at 9.4 T. *Journal of Magnetic Resonance Imaging* 2011; **34**: 1388-1396.

49. Baur F, Brown J. The Fatty Acids of Corn Oil. *Journal of the American Chemical Society* 1945; **67**: 1899-1900.

50. Gambarota G, Tanner M, van der Graaf M, Mulkern RV, Newbould RD. ^{1}H-MRS of hepatic fat using short TR at 3T: SNR optimization and fast T2 relaxometry. Magn Reson Mater Phy 2011;24(6):339-345.

51. Stables L, Kennan R, Anderson A, Gore J. Density Matrix Simulations of the Effects of J Coupling in Spin Echo and Fast Spin Echo Imaging. Journal of Magnetic Resonance 1999;140:305-314.

52. Guillén MD, Ruiz A. Rapid simultaneous determination by proton NMR of unsaturation and composition of acyl groups in vegetable oils. Eur J Lipid Sci Technol 2003;105:688-696.

53. Thompson RB, Allen PS. Sources of variability in the response of coupled spins to the PRESS sequence and their potential impact on metabolite quantification. Magn Reson Med 1999;41:1162-1169.

54. Thompson RB, Allen PS. Response of metabolites with coupled spins to the STEAM sequence. Magn Reson Med 2001;45:955-965.

55. Kugel H, Jung C, Shulte O, Henidel W. Age- and sex-specific differences in the ^{1}H spectrum of vertebral bone marrow. J Magn Reson Imag 2001;13:263-268.

56. Machann J, Thamer C, Schnoedt B, et al. Hepatic lipid accumulation in healthy subjects: a comparative study using spectral fat-selective MRI and volume-localized ^{1}H-MR spectroscopy. Magn Reson Med 2006;55:913-917.

57. Listerud J, Mulkern R. The J Coupling Hypothesis for Bright Fat observed on FSE. *Proceedings of the Society of Magnetic Resonance in Medicine 11th Annual Meeting* 1992: 4505.